DUST DYNAMICS IN A COLLAPSING PRESTELLAR CORE

Master Thesis

May 20, 2021

DANIEL PLOUG HALL

SUPERVISOR:
TROELS HAUGBØLLE

UNIVERSITY OF COPENHAGEN
FACULTY OF SCIENCE
NIELS BOHR INSTITUTE

Abstract

The interstellar medium is the birth place of stars and planets, and is thus of great interest. Here the cold phase of the ISM called molecular clouds collapse into prestellar cores, which in the end form the stars and planets. In the ISM small aggregates of heavier atoms exists collected in either carbon, iron, silicate dominated dust grains. Dust is present in every phase of the ISM and is of great importance in observations thought emission and absorption of light, in astrochemistry where it acts as a catalyst for the creation of water and other molecules, and in the formation and creation of planets in a protoplanetary disk. This happens through dust-to-dust collisions where the dust can coagulate and grow in size until grains reach mm-sizes. These pebbles are then collected in collective streaming instabilities in to planetesimals that may grow further either though collisions or effective aerodynamically assisted pebble accretion.

The dynamics and evolution of dust in protoplanetary disks has received massive attention in the past decade, due to direct observations and the importance for understanding formation o planets, comparatively the dynamics and evolution of dust in the earlier phases has received much less attention. The goal of the thesis is to begin to understand how dust settles in a prestellar core, to create more realistic initial conditions for dust in the protoplanetary disk from numerical simulations of dust-gas interaction. A Larganian background model is used for the prestellar core, in different configurations. I have investigated 12 cores with varying mass ranging from 1 to $8M_\odot$, temperature ranging from 5 to 10K and radius ranging from $3000 - 7500$AU. To handle the dust numerically in the cores, a set of numerical methods were created to distribute the dust throughout the core and to couple the gas distribution described in the Lagrangian mesh and the dust particles, whose movement is solved with a leapfrog integration scheme.

The settling of dust was found to be present for particles as small as $25\mu m$, although it was the smallest size tested. The velocities of the particles were also show to have an effect on the particles, as the lower azimuthal velocities would result in more infall. Further more the dust-to-gas ratio stops to increase further once the first Larson core form as the particles will couple to the gas once inside. Coagulation becomes a prominent effects once inside the first Larson core due to the increase in dust density, at least for particles around or smaller than $100\mu m$. It was found that if the dust particles are critically coupled to the core, then the dust-to-gas ratio inside the proto-star can be quite high, and thus in turn have a high metalicity. Further more the dust-to-gas ratio for the protoplanetary disk reach higher than the canonical dust-to-gas ratio of 0.01. This shows that the dynamics of the core plays a role for both the disk and the star, and further research into more complex simulations should be future priority.

Contents

List of Figures

List of Tables

Introduction

Astronomers have for many millennia and across cultures looked out into the vast emptiness of space, at first observing stars and planets. As technology improved the ability to observe further away and in greater detail was becoming possible. Here scientists discovered that stars were not alone but rather a medium was between them.

The Interstellar Medium or ISM for short, is the collective description for the material between the stars which includes but is not limited to Hydrogen, Helium, dust particles and various molecules like CO, but also magnetic fields, from moving charged particles, and radiation fields from stars. In other words, a mostly gaseous mass which is subject to radiative and magnetic forces. The ISM was formed when the soup of ions formed in the Big Bang cooled sufficiently, thus allowing atoms and molecules to form. However, the ISM is not filled with remnants from ancient times, as stars form and die using old and birth to new material ([Schulz, 2012]). The ISM varies a lot in terms of its physical properties as the temperature and number density various with orders of magnitude. There are 3 general phases of the ISM with further sub-categorization. The cold ISM consistent of molecules and atomic gases with temperatures below 100K. The warm medium consistent of mostly atomic and ionized hydrogen with temperature up to 10^4K. The hot medium which is characterized by being an ionized shocked gas created from supernovas and stellar wind[Schulz, 2012], and can reach temperatures up to 10^7K, coming from shocks from supernovas and stellar winds.

A sub-category of special interest in the cold ISM, is that of the cold molecular cloud. The molecular cloud is the coldest and most dense region of the ISM with number densities over 1000cm^{-3}, which is quite dense, and temperatures around 10-50K. Thus the molecular cloud is a prime suspect for star formation. These low temperatures are obtained because the cloud is in thermal balance between the heating from stars and cosmic rays, and being subsequently cooled by interstellar dust which absorbs and scatters light. The sizes of molecular clouds vary a lot ranging from 1 to 100pc where the larger ones are called giant molecular clouds. The masses here naturally also varies by a great amount, ranging from 10 to 10^6 $\text{M}_\odot$ ([Schulz, 2012]). The shape of the molecular clouds is quite irregular, which also extends to the mass distribution. These irregularities can cause fragmentation within the cloud, due to the jeans instability given by the following:

$$\lambda_j = \sqrt{\frac{\pi c_s^2}{G\rho}} \tag{1.1}$$

$$M_j = \frac{\pi^{5/2}}{6} \frac{c_s^3}{\sqrt{G\rho}} \tag{1.2}$$

Here λ_j is called the jeans critical length, and M_j is the critical jeans mass. Since both critical parameters depend on the density, they will decrease as a local volume in the could becomes denser, and as such it can collapse and fragment the cloud. However, observations carried out the in recent years, thanks to the Herschel telescope, has shown that molecular clouds have

a filament-like structure ([Arzoumanian et al., 2011, Palmeirim et al., 2013, Peretto et al., 2012]). These complex structures indicate quite a dynamical system where material flows and collect in bulk. Numerical work eq. [Nakamura and Li, 2008, Padoan et al., 2001] shows that the filaments is a natural consequence of turbulence which can be induced by stellar feedback on larger scales. As the filaments become more dense, the collapse due to the aforementioned jeans instability and fragment the cloud. This fragmentation and their elongated shape give rise to a new bound object, that of the prestellar core or dense cores in some literature. These prestellar cores are observed to be created in bulk from in the filaments as shown in [Palmeirim et al., 2013]. This has also been confirmed by numerical models eg. [Burkert and Hartmann, 2004]. An interesting aspect to this is that the cores are not separated from the filaments. For it seems that there is an inflow from the filaments, which can feed material into the cores themself. This was observed in [Kirk et al., 2013], which observed the Serpens South embedded cluster. Here the researchers found that the filaments accrete around $130 M_\odot/yr$ from the surrounding cloud medium, and they in turn accrete around $28 M_\odot/yr$ into the cluster of prestellar cores.

The prestellar cores are the birth place of low mass stars, formed when the core collapses under its own gravity. The cores are elongated along their host filament with temperatures near $10K$ throughout, albeit not constant ([Arzoumanian et al., 2011, Stahler and Palla, 2004c]). The density profile of the cores can be challenging to measure since the normal tracer for molecular clouds are optically thick for a dense core. Therefore other tracers are useful such as NH_3, CS or rare isotopes of CO ([Hartmann, 2008a]). Other techniques uses the absorption and emission of dust though near-inferred extinction, mm to sub-mm dust emission or absorption against a bright background emission ([Bergin and Tafalla, 2007]). in a sub-mm survey of cores it was found in [Ward-Thompson et al., 1994] that the density profile of cores are flatten near the center, while the outer rim is described by a power-law, which fits well with the theoretical Bonner-Ebert sphere discussed in chapter 2.

Stars are created from the gravitational collapse of an unstable prestellar core. If rotation is present during this collapse, then a protoplanetary disk, or accretion disk is formed around the protostar along the midplane of the rotational axis. The accretion disk transports material such as dust and gas unto the surface of the protostar, due to transport of angular momentum. This transport is caused by a difference in the keplarian angular velocity given by $\Omega = (GM/r^3)^{1/2}$, where G is the gravitational constant, M is the integrated mass at a radius r. The viscosity of the disk will thus create a friction force between particles with different velocities. This friction will slow down material further by forcing it to drift outwards, while material further out will increase their velocity and thus drift inwards. The dynamics of accretion disks have been studied though numerical work eg. in [Birnstiel, T. et al., 2010]. It is in these protoplanetary disk that planets are created.

The formation of planets are not fully understood, although it is generally understood that dust particles play a vital role in their creations. Dust particles are aggregates made out of various materials such as graphite, iron, silicone carbide etc.([Schulz, 2012]). Dust is often assumed consist of spherical particles, however this is far from the truth as dust particles are mostly irregular shapes. These shapes come from the merger of dust called coagulation, destruction from mass transfer, erossion/cratering and fragmentation ([Windmark, F. et al., 2012]) which can form a variety of shapes. This is discussed in section 1.1. With coagulation, dust can in theory grow to an infinite size and thus potentially grow, if rapid enough, to a planet. However, fragmentation and particle bouncing can affect the growth rate quite significantly. This is shown in figure 1.1 which is figure 8 from [Windmark, F. et al., 2012]. Here one can see that dust with sizes close to 1 cm will likely bounce off each other, which is called the bouncing barrier or meter-size barrier, which is hard to pass. Furthermore, particles in the meter size range will either erode or fragment, preventing growth from such interactions. As presented in [Windmark, F. et al., 2012], the only way for meter-sized particles to
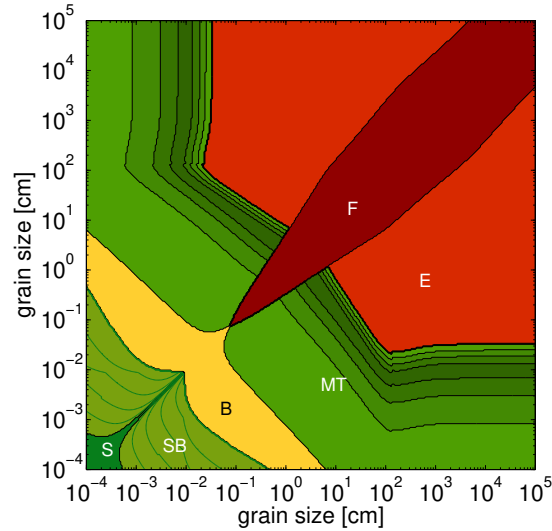
Figure 1.1: Figure 8 borrowed from [Windmark, F. et al., 2012]. Here F is fragmentation, E is erosion, MT is mass transfer, B is bouncing, and S is sticking. Here its quite clear that there is a bounding barrier near 1 cm dust, which can prevent growth. Furthermore near grain sizes of 1 meter there is a large region of erosion and fragmentation. This is the meter barrier, and prevents larger dust particles to grow though interation of equally sizes particles.

growth larger is from mass transfer, which is where cratering occurs and some mass of the smaller particle sticks to the dust grain and thus gives a net increase in size. If dust grains have accumulated enough to be around the km-size, called a planetesimal then they can grow from pebble accretion. pebble accretion is the idea that as a planetesimal moves though a medium it can due to gravity collect smaller particles which then accurate unto the surface, which can result in growth, and as such a potential planet ([Brouwers et al., 2018, Ormel et al., 2021])

When observing a galaxy or a patch in the ISM though the visible band, one will likely observe dark patches in contrast to the potentially bright background. These patches are dust absorbing and scattering the background light. This process is called extinction and can be quite useful in observations since it can be linked to the column density of hydrogen though an extinction law.

$$A_V = 0.56 N_H + 0.23 \tag{1.3}$$

Where N_H is the column density in units of 10^{21}cm^{-2} ([Schulz, 2012]). In other words, dust can through its scattering of photons be used by observers to map the hydrogen column densities, and thus measure the amount of gas in eg. a cloud. Dust emits black body radiation through absorbtion of photons, and remits them as infrared light. The extinction from dust limits what we observe in our telescopes. Since dust tend to scatter blue light, which naturally means that what we observe is more red.

Astrochemistry is quite interesting with respect to the ISM, since here astronomers use tracers, various atoms and molecules, to measure parts of the ISM. In this case dust particles can play an important role as they can function as a catalyst for various reactions. They do so by absorbing atoms, ie. it clings to the surface of the dust grain, which can then collide/interact with other molecules on the surface of the dust grain. This can happen though two mechanism, the first being the Eley-Rideal mechanism, in which the atom clings to the grain and the atom is then directly hit by another particle. This is shown below where an arbitrary atom X is clinging to the dust, g, and X is then hit by another arbitrary atom Y.

$$X + Y : g \rightarrow X - Y : g \rightarrow XY + g$$
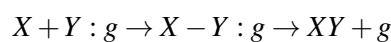
This method is quite unlikely to occur as since the probability of directly hitting the stuck atoms is not that big ([van Dishoeck, 1988]). Another way is that of the Langmuir-Hinshelwood mechanism in which both atoms X and Y cling to the surface of the grain, and they can then interact thought random walks on top of the surface given by:

$$X + Y : g \rightarrow Y : g : X \rightarrow X - Y : g \rightarrow XY + g$$
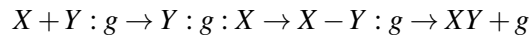
Through these effects, dust can help create a larger abundance of molecules and can also help with the creation of water [Tielens and Hagen, 1982]. Furthermore there is the possibility that other molecules freeze out on the grain if the temperature is low enough. Here an example could be CO freezing out and thus making it harder to use it for observations

As presented in this chapter, dust is important in all aspects of the ISM and star formation. It is important for our understating of the universe, as it can be used to both aid and hinder our observations. Although its is also quite important to understand the dynamics of the dust within the different hierarchies of the ISM, as understanding the dust dynamics in the prestellar core gives the initial conditions for the accretion disk, and by extension the creation of planets.

1.1 Numerical Context
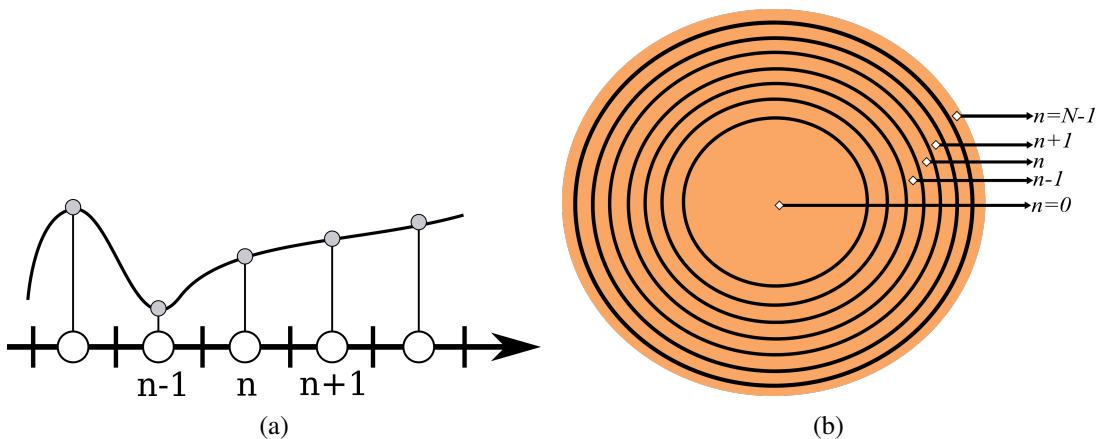
Figure 1.2: **a)** Illustration showing the sampling idea. Here the curve is a continuous quantity, eg. density, which is then sampled into the white circles on the arrow, with corresponding sampled quantities represented by the small grey dots. **b)** Illustration of the spherically symmetric mesh, where each cell is corresponds to a spherical shell.

In many fields such as biology, physics, chemistry etc., differential equation are used to a great effect, as it may describe a variety of problems and properties. The partial differential equation is especially useful as it can describe problems in multiple dimensions, eg. the flow of water in two spatial coordinates and in time. However, the solutions to many differential equations are hard to solve analytically, if solvable at all. Instead numerical methods have been developed over many years to approximate the solutions to the problem. Solving a differential equation numerically has become incredibly practical with the rise of the computer, since it is now possible to solve many coupled systems of equations in a reasonable amount of time and effort. There are a multitude of ways to develop a scheme that allows for a numerical approximation to the system, including the Finite difference method, Finite volume method and the Finite volume method. There do also exist methods that are outside or heavily modified versions of these like the Runge-Kutta method or the leapfrog method, the latter of which is presented in subsection 3.4.1.

The usage of these methods is normally referred to as discretising the problem, since in all of these problems one generates a discrete set of data, referred to as a mesh or grid. This can be thought of as a sampling of a continuous quantity in space, as illustrated in figure 1.2a. Here the spacial or temporial discrete points are refered to as cells or bins, which can have a width associated with them. This width describe the volume (if 3D) they govern. The transit from one cell to another is called the interface which is shown in figure 1.2a, as the vertical black lines between the white dots. The shape of the cells can by anything needed for the problem, such as squares or triangles. In the case of a spherically symmetric problem, the cells can represent spherical shell as illustrated in figure 1.2b

In order to distinguish these cells, the notation adapted in this thesis is ψ_n^i. Here the index i refers to the current time step, hence $i+1$ is the next time step and $i-1$ is the previous time step. This also goes for the spatial index n where its the spatial cells. The interfaces between the cells are given a $n \pm 1/2$ index, where $n+1/2$ is the interface between cells n and $n+1$

1.2 Structure of thesis

The structure is as follows:

- Chapter 2 presents how to solve the Bonnor-Ebert sphere for use in numerical work.

- Chapter 3 shows how to model the interaction of dust with gas through drag in eg. a Bonnor-ebert sphere, where the dust is considered as macro particles.

- Chapter 4 discusses the usage of a background sphere model, together with algorithms for mapping dust to numerical cells of the given background model.

- The findings of the report are presented, discussed and concluded in Chapter 5, 6 and 7.

Prestellar core

As mentioned in Chapter 1, the prestellar cores are have relativley homogenous centers and are close to isothermal. This fits with the a theoretical prestellar core called the Bonnor-Ebert sphere. In order to model a prestallar core, and its potential collapse, the Bonnor-Ebert sphere is often adapted as it observations approximately ([Alves et al., 2001]), and it allows the modeller to easily create cores of varying size, mass and temperature. The Bonnor-Ebert sphere is assumed to be spherical, however, there is some tension as of observed cores tend to be elongated along their filaments ([Arzoumanian et al., 2011]).

2.1   Solving a Bonnor-Ebert sphere

The Bonnar-ebert sphere is a isothermal sphere in hydrostatic equilibrium. To construct a set of equation that describe this system we can start with the conservative Eulian fluid equations

$$\frac{\partial \rho}{\partial t} + \nabla \cdot (\rho \mathbf{v}) = 0 \tag{2.1}$$

$$\frac{\partial \rho \mathbf{v}}{\partial t} + \nabla \cdot (\rho \mathbf{v} \otimes \mathbf{v}) = -\nabla P + \rho \mathbf{a} \tag{2.2}$$

$$\frac{\partial E}{\partial t} + \nabla \cdot ([E + P]\mathbf{v}) = \rho \mathbf{v} \cdot \mathbf{a} \tag{2.3}$$

Here ρ is the fluid density with a velocity $\mathbf{v}$. The fluid can be affected by a preassure P and have a total energy of E. The first equation is the mass conservation equation, the second is the momentum conservation equation and the last is conservation of the total energy density equal to the internal and kinetic energy density $E = \rho e_{int} + 1/2\rho |\mathbf{v}|^2$. For the sphere to be in hydrostaic equilibirum we assume a steady state and no flows ($\mathbf{v} = 0$). Under these assumptions only the momentum equation, ie equation (2.2), is non-zero.

$$\nabla P = \rho \mathbf{a} \tag{2.4}$$

We assume that the acceleration is due to gravity given by the gravitational potential ϕ.

$$\mathbf{a} = -\nabla \phi \tag{2.5}$$

$$\nabla^2 \phi = 4\pi G \rho \tag{2.6}$$

We can now combine equation (2.4), (2.5) and (2.6) to obtain a equilibrium equation for a sphere.

$$\nabla \cdot \left(\frac{\nabla P}{\rho}\right) - 4\pi G \rho = 0 \tag{2.7}$$

Assuming that the sphere is spherically symmetric and thus only depend on the radius, one can obtain the following.

$$\frac{1}{r^2} \frac{d}{dr} \left(\frac{r^2}{\rho} \frac{dP}{dr}\right) + 4\pi G \rho = 0 \tag{2.8}$$

As we assumed that the sphere is isothermal we use the relation $P = c_s^2 \rho$, where $c_s^2 = k_b T/(\mu m_h)$, to obtain an equation that is only depended on density and thus can be solved.

$$\frac{1}{r^2} \frac{d}{dr} \left(\frac{r^2}{\rho} \frac{d\rho}{dr} \right) + \frac{4\pi G}{c_s^2} \rho = 0 \tag{2.9}$$

This equation describe a barocentric fluid, and to solve it we need a set of boundary conditions.

$$\rho(0) = \rho_c \tag{2.10}$$

$$\left. \frac{d\rho}{dr} \right|_{r=0} = 0 \tag{2.11}$$

Here we define a Dirichlet boundary where the central density is equal to a value of ρ_c so we ensure that ρ doesn't go towards infinity as r goes to 0. A Neumann boundary condition is also defined where the gradient at the center is 0. These boundary conditions were proposed in [Bonnor, 1956].

As the system is a simple ODE, it will be a benefit to write it in dimensionless form. To do this we need to define characteristic parameters. The benefit of this is that we can solve the equation once, and then scale the solution with the parameters to obtain every possible Bonner-Ebert sphere. In the system we have the constants of π, G, c_s^2 and ρ_c. The latter which we defined our self. From these constants we can define a characteristic length.

$$r_c = \frac{c_s}{\sqrt{4\pi G \rho_c}} \tag{2.12}$$

The inclusion of 4π in this definition is to clean up the equation by removing dimensional constants. We know define a dimensionless density and radius given in equations (2.13) and (2.14)

$$x = \frac{r}{r_c} \tag{2.13}$$

$$y = \frac{\rho}{\rho_c} \tag{2.14}$$

These can them be substituted into into equation (2.9) to obtain equation (2.15).

$$\frac{1}{x^2} \frac{d}{dx} \left(\frac{x^2}{y} \frac{dy}{dx} \right) + y = 0 \tag{2.15}$$

Here we define $u = \ln(y)$ to make the equation resemble a Lane-Emden equation.

$$\frac{1}{x^2} \frac{d}{dx} \left(x^2 \frac{du}{dx} \right) + e^u = 0 \tag{2.16}$$

We now further define z to obtain a set of first-order coupled differential equations.

$$z = x^2 \frac{du}{dx} \Leftrightarrow \frac{du}{dx} = \frac{z}{x^2} \tag{2.17}$$

$$\frac{1}{x^2} \frac{dz}{dx} + e^u = 0 \Leftrightarrow \frac{dz}{dx} = -x^2 e^u \tag{2.18}$$

The boundary conditions defined earlier can now be redefined for the new system of equations.

$$\ln(y(0)) = \ln \left(\frac{\rho_c}{\rho_c} \right) = u(0) = 0 \tag{2.19}$$

$$\left. \frac{dy}{dx} \right|_{x=0} = e^{u(0)} \left. \frac{du}{dx} \right|_{r=0} = \left. \frac{du}{dx} \right|_{r=0} = 0 \tag{2.20}$$

Figure 2.1 shows the solution to the set of coupled ODEs which was solved with a Runge-Kutta method. Here we see that the sphere has a constant density in the center, and goes roughly as r^{-2} further out.
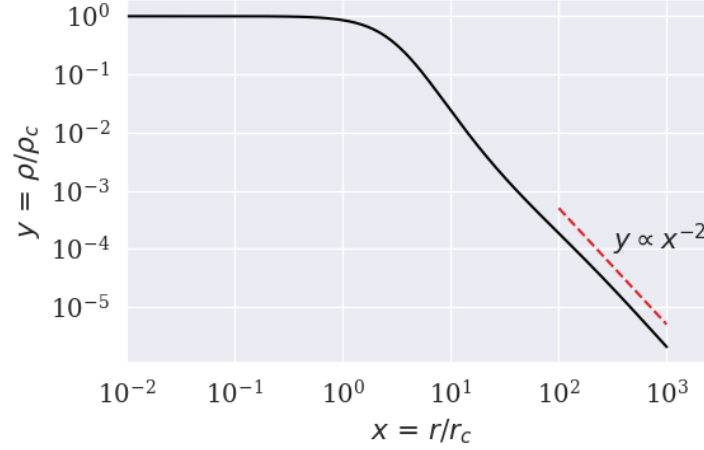
Figure 2.1: Solution to the Lane-Emden equation. Here we see that the center of the Bonnor emden sphere is constant while the outer parts goes as r^{-2} as shown with the red dotted line.

2.1.1 Stability of a Bonner-Ebert sphere

In [Bonnor, 1956] a stability criteria was given for the sphere. Here the outer pressure gradient should be less than 0, such that pressure perturbations in the sphere would dampen, and not cause a run away effect.

$$\frac{\partial P_0}{\partial r_0} < 0 \tag{2.21}$$

To find a relation between what mass, temperature and radius is needed to create a stable BE sphere, we firstly need to find an expression for the outer pressure we can solve. We start with $P_0 = P(x_o) = c_s^2 \rho(x_0) = c_s^2 \rho_0$. Here we need an expression for the outer density which can be obtained from the mass and substituting in the adimensional parameters.

$$M_0 = 4\pi r_c^3 \rho_c \int_0^{x_0} x^2 y \, dx = 4\pi \left(\frac{c_s}{\sqrt{4\pi G \rho_c}} \right)^3 \rho_c \eta(x_0) = \frac{c_s^3}{\sqrt{G^3 \rho_o}} \sqrt{\frac{y_0}{4\pi}} \eta(x_0) \tag{2.22}$$

We can now isolate ρ_0 and use it to express the outer pressure P_0 as function of mass.

$$P_0 = \frac{c_s^8}{G^3 M_0^2} \left(\sqrt{\frac{y_0}{4\pi}} \eta(x_0) \right)^2 = \frac{c_s^8}{G^3 M_0^2} m(x_0)^2 \tag{2.23}$$

The above equation shows that P_o only depends on x_o though the adimensional mass m, as the outer mass is a known constant. With this we can find the critical pressure for when a Bonnor-ebert sphere goes from stable to unstable, ie when $\partial_{r_0} P_0 = 0$. From figure 2.2 we find, with the help of a root finder, that the critical mass, radius, density and pressure which are represented in table 2.1. With these values we can now create a useful relation between mass, temperature and radius of the sphere. First we define the stable radius of the sphere.

x_0	y_0	$m(x_0)$	$P(x_0) = m(x_0)^2$
6.45	1/14.04	1.18	1.40

Table 2.1: Table over the critical values for a stable Bonner-Ebert sphere.

$$R_{BE} = r_c x_0 = \frac{c_s}{\sqrt{4\pi G \rho_c}} x_0 \tag{2.24}$$
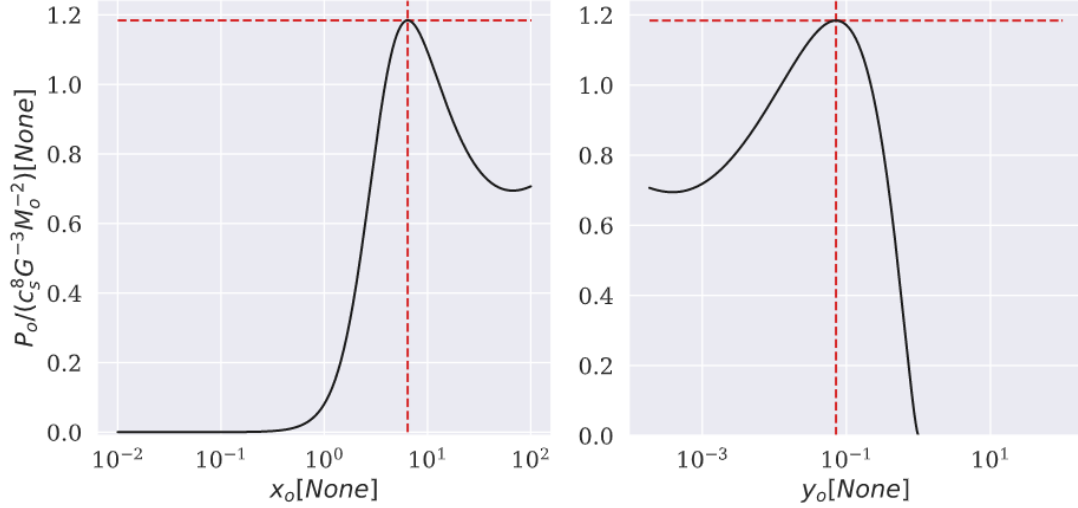
Figure 2.2: Figure of the outer pressure as a function of the dimensionless radius x_o on the left plot and the dimensionless density y_0 on the right plot. The dotted red lines indicate the placement of the critical values

By combining this with equation (2.22), we obtain an expression that couples our stable outer values, temperature, mass and radius.

$$M_{BE} = \frac{c_s^2}{G} \frac{\eta(x_0)}{x_0} R_{BE} = \frac{c_s^2}{G} \sqrt{\frac{4\pi}{y_0}} \frac{m(x_0)}{x_0} R_{BE} = 2.434 \frac{c_s^2}{G} R_{BE} \tag{2.25}$$

We can rewrite this equation in a mass-radius ratio, in units of $M_\odot$, AU and K.

$$\left[\frac{M_{BE}}{M_\odot}\right] \left[\frac{R_{BE}}{AU}\right]^{-1} \approx \frac{1}{10581} \left[\frac{T}{10K}\right] \tag{2.26}$$

This means that a if the sphere with a temperature of $10K$ and a mass of $1M_\odot$ then to be stable it needs to have a radius of 10581 AU. To furthere visualize the runaway effect from the pressure one can construct a pressure-volume diagram. A volume can be define quite easily from the radius of the critically stable Bonner-Ebert sphere and using $P_0 = c_s^2 \rho_0$ and equation (2.23).

$$V = \frac{4}{3}\pi R_{BE}^3 = \frac{\sqrt{4\pi}}{3} \frac{GM_0}{c_s^2} \frac{x_0 \sqrt{y_0}}{m(x_0)} = \xi \frac{GM_0}{c_s^2} \frac{x_0 \sqrt{y_0}}{m(x_0)} \tag{2.27}$$

Thus the P-V diagram becomes figure 2.3. The P-V diagram in figure 2.3, shows the instability given in equation (2.21). For here the gradient of the pressure is negative when going from infinity to x_0, located near the bent. As the volume becomes small enough the pressure can then no longer increase to counter act the collapse, as seen with the decrease in pressure to the left of x_0. This causes the collapse of the sphere as gravity will begin to dominate over the internal pressure in the cloud.

2.2 A collapsing Bonnar-Ebert sphere

In this section some short introductions to a presteallar core collapse are represented. However the mathematical nature of the core collapse will not be more in depth than a base level introduction, to give perspective for what effect might have been left out by the sphere data used in chapter 5 and discussed in chapter 4. This is mostly as the collapse of a sphere can be quite complex and could well be a master thesis in itself. The focus of this thesis is the
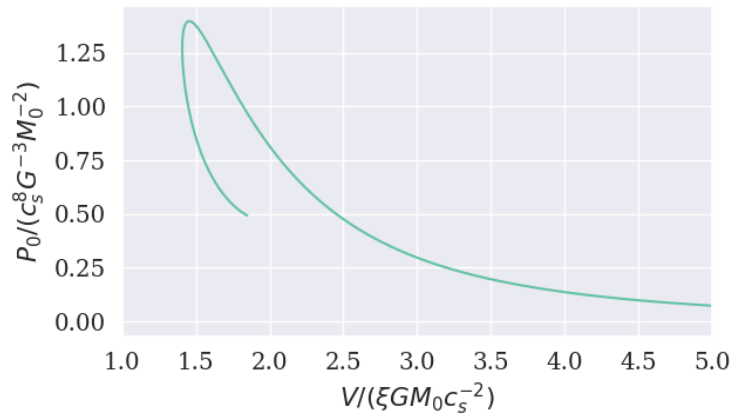
Figure 2.3: P-V plot where one can easily see the instability criteria, as the pressure stops to rise after a certain amount of compression.

dust dynamics in a collpasing core, but it is still useful to have a basic understanding and perspective on different forces and processes that affects the gas. If however the reader is more curious i highly recommend The Formation of Stars by Steven W. Stahler and Francesco Palla, and Accretion Processes in Star Formation by Lee Hartmann as they give a great inside to the theory and observation for the presented theory.

2.2.1 The effect of Gravity
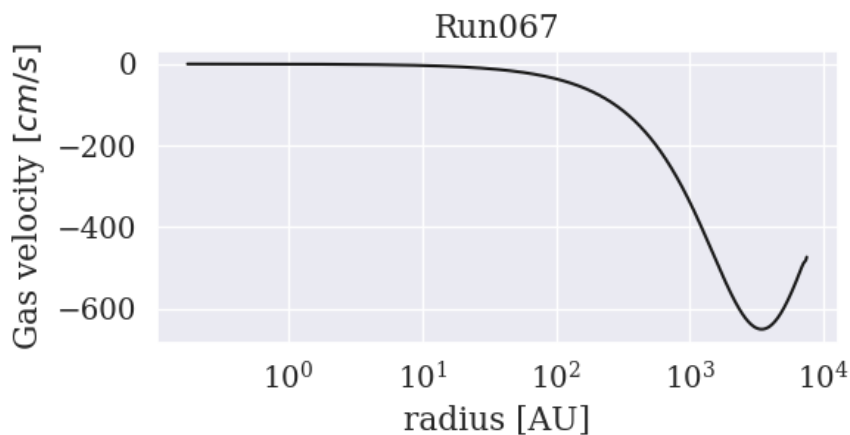
Figure 2.4: The radial gas velocity in the early stages of a collapse.

If one naively considers a collapse of a Bonner-Ebert sphere, one can easily think that that it will collapse like a singular core ($\rho \to \infty$ as $r \to 0$) with an inside out collapse. This is due to the free fall time is inversely proportional to the square root of the density and thus is shorter near the center. However this is not the case as the Bonner Ebert sphere collapses from the outside and in. As seen in figure 2.4, where the velocity of the gas increases further out and then falls in. Here there is an higher initial infall of mass due to the constant density near the center, these parts have the same free fall time, and will therefor hit the center at the same time. That a Bonner-Ebert sphere collapses might at first seem unintuitive. However if one compares the critical jeans mass given in equation (1.2), with the bonnor-ebert mass from equation (2.22), it easily to see that there is a factor of ~ 2.5 difference, if one assumes the average uniform density in the jeans mass is the outer density of a Bonnor-Ebert sphere. This

factor difference between the two likely comes from the difference in assumption in density, and therefor one can argue that the instability/collapse of the core is due to the jeans instability which affects larger scales.

2.2.2 Rotations effect and creation protoplanetary disks

Rotations is a physcial effect that causes the prestellar core to form a prestellar disk. This effect can be studied in a simple simple case. If we assume a spherical symmetric cloud, and it rotates as a solid body. Here we will have a specific angular momentum $j = r \times v$ and a uniform angular velocity $\omega = v_\phi/r$ and a fixed central mass M, then if material falls into a keplerian orbit we will get a radius of ([Hartmann, 2008b]).

$$R = \frac{j^2}{GM} = \frac{r^4 \omega^2 \sin^2(\theta)}{GM} \tag{2.28}$$

Here θ is the angle from the rotation axis midpoint to the particle. Here we see that if θ equals zero then we material will just fall into the core, as their angular momentum is non-existent, if the angle is $\pi/2$ then the material will fall to an orbit at a given radius.

$$r_c = \frac{r^4 \omega^2}{GM} \tag{2.29}$$
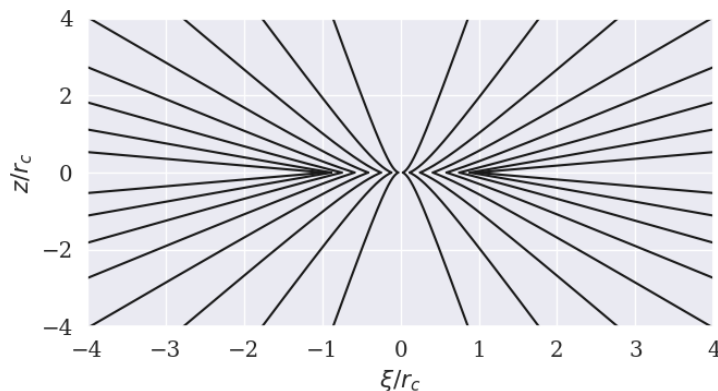
Figure 2.5: Here is shown the streamlines that comes as a consequence of the rotating core. Here particles move along the trajectories and collide in the mid plane, giving birth a proto-plantary disk

This radius is called the centrifugal radius, which dictates the maximum radius that the material will fall into to. If one take this one step further such that a particle moves along a plane with an angle, ϕ, to the rotation midplane one can find streamlines and mass contours for the collapse. The geometry of this is shown in figure 2.6. This is done in great detail in both [Hartmann, 2008b] and [Stahler and Palla, 2004a], and only the results will be presented here. They both find a relationship between the spherical radius r and the centrifugal radius.

$$\frac{r}{r_c} = \frac{\sin^2(\phi)\cos(\phi)}{\cos(\phi) - \cos(\theta)} \tag{2.30}$$

The spherical radius can be described in terms of a cylindrical radius ξ and the height z.

$$r = \sqrt{\xi^2 + z^2} \tag{2.31}$$

$$z = r\cos(\theta) \tag{2.32}$$

Using these equation together with equation (2.30), one can obtain the streamline for the infall. These streamlines are plotted in figure 2.5. Here each line represent a different value of ϕ. Here it is quite clear that material that starts with a small height fall in to the centrifugal radius and material that starts with a larger height fall into the center. From the streamlines one can see that material falling from $+z$ collide with material coming from $-z$ in the mid-plane. This will give rise to the creation of the protoplanetary disk.
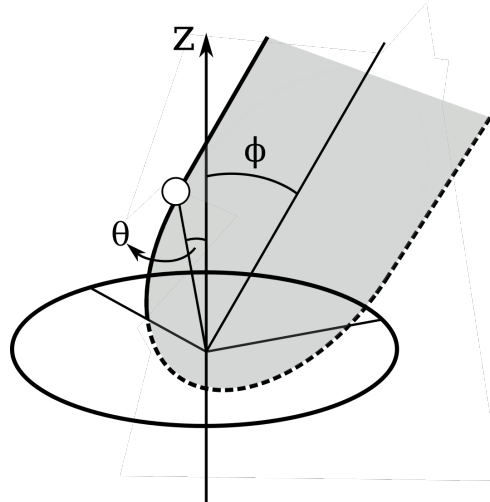
Figure 2.6: Figure is drawn after figure 10.16 in [Stahler and Palla, 2004b], such that the syntax in used in this section matched with the illustration. here the orbital plane of the particle is illustrated by the shaded area, with the angle ϕ with respect to the z-axis, while the particle has an angle θ with repspect to the z-axis
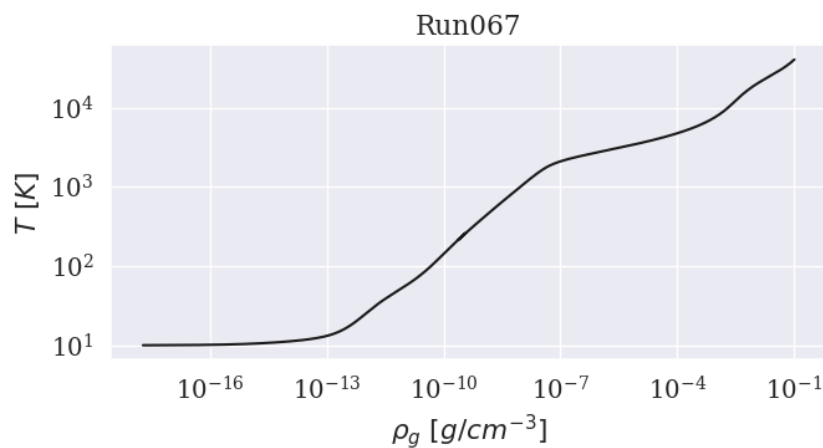
Figure 2.7: This figure shows the temperature as a function of gas density for a presteallar core, specifically run067 shown in table 5.1. Here the collapses happens when the temperature is near constant and adiabatic process which dictates the first and second Larson core are the slopes where temperature increases.

2.2.3 Radiative effect

Radiative transport is a field of physics that explain how energy, eg from the sun or a hot stove is transfered though a medium such as earths atmosphere or a dense core. For a collapsing core it is also quite relevant and important, as under a collapse the opacity of the core can change drastically. When a bonnor-ebert sphere starts its collapse it will be a optically thick

(low opacity) and isothermal. As the collapse undergoes most of the energy released from the potential energy is radiated into the cosmos. At some point the density reaches around 10^{-14}g cm^{-3} ([Vaytet and Haugbølle, 2017]), and the opacity increases trapping more energy. After a bit the sphere becomes optically thick to its own radiation, trapping the energy within it. This creates an increase in temperature, and thus creates a radioactive pressure which stops the collapse. Here the sphere enters a new hydrostatic equilibrium called the first Larson core.

Mass accretes unto the core from an envelope that used to be the outer parts of the sphere. This accretion will naturally increase the effect of gravity, and the core begins a adiabatic process, which increase the temperature, to keep its equilibrium. Once the temperature reaches 2000K, the H_2 molecules disassociate. This process is endothermic in nature, meaning it uses energy to occur. This loss of energy will decrease the temperature increase over time meaning that the equilibrium can no longer be satisfied, and a second collapse occurs which is also close to isothermal [Vaytet and Haugbølle, 2017]. This collapse continues until the H_2 molecules have been almost completely dissociated, and thus enter a second hydrostatic equilibirum and the tempureture begins to increase adiabticlly again. This is called the second Larson core, also called a protostar. The core stays until fusion begins and the star is born.

3

Dust dynamics and numerical methods

3.1 Choice of dust simulation approach

Generally, there are two approaches to simulating the interaction between dust and gas. The multi-fluid approach and the Lagrangian approach (not to be confused with a Lagrangian mesh).

1. The multi-fluid approach is where the dust particles are considered to act as a fluid. This holds true if the dust particles are small enough to couple with the gas. With this method one has to write out the fluid equations for the dust, and take into account its interaction with the gas though drag. These will have a form close to equation (2.1), (2.1) and (2.3), and has been done for a protostellar disk in [Birnstiel et al., 2010]. The benefit of this approach is that there exist a plethora of methods and libraries for solving hydrodynamics. This approach also scales quite nicely if one wants to include more dust, as one just have to increase the floating point numbers per cell.

   The biggest downside to this methods is, as mentioned, the particles need to be coupled to the gas. This naturally puts a constraint on the grain size on a pr case basis.

2. In the Lagrangian approach one considers the dust particles as their own separate entity, this can become quite computationally expensive as the problem size grows. One can levitate this downside by considering Marco particles, which essentially are a "bag" of dust that is considered one singular evolving unit. The benefit here is that one can consider particles of larger stokes number (Section 3.3), and doesn't need to ensure that the particles decouple. However the downside, other than the computational expense, is that its more programming intensive as there needs to be subroutines to map the particles to the environment cells, distributing mass to each macro particle correctly etc.

There is nothing that makes one approach inherently better than the other. In this thesis the Lagrangian approach was chosen. This was mostly done since what evolved into the entire thesis was originally supposed to be a little testing program, before moving into large scale simulations with the FORTRAN library `DISPATCH`.

3.2 Drag regimes regimes for dust

When dust particles move through a gaseous fluid, such as a molecular cloud, protoplanetary disk or a prestellar core, they will experience a drag force opposite of its trajectory ([Armitage, 2007, Weidenschilling, 1977]).

$$\mathbf{F_D} = -\frac{1}{2} C_d \pi s^2 \rho_g |\mathbf{v}_{dg}| \mathbf{v}_{dg} \qquad (3.1)$$

Here πs^2 is the cross section area of a spherical dust grain, ρ_g is the density of the gas, the relative velocity between dust and gas is $\mathbf{v}_{dg} = \mathbf{v}_d - \mathbf{v}_g$ and C_D which is the drag coefficient.The

drag coefficient changes depending on drag regime the dust particle is in. There are 2 regimes to consider, called the Epstein and Stokes Regime.

The coefficient of the Epstein regime is defined as

$$C_D = \frac{8}{3} \frac{\bar{v}}{|\mathbf{v}_{dg}|} \quad \text{for } s < \frac{9}{4}\lambda_{mfp} \tag{3.2}$$

Here λ_{mfp} is the mean-free path of the gas and $\bar{v} = \sqrt{8/\pi}c_s$ is called the thermal velocity ([Armitage, 2007]) . The mean free path is calculated from the number density of the gas and the geometric cross section of a hydrogen molecule ([Birnstiel et al., 2010]).

$$\lambda_{mfp} = \frac{1}{\sigma_{H_2} n_g} \tag{3.3}$$

Here the $\sigma_{H_2} = 2 \cdot 10^{15} \text{cm}^2$ ([Birnstiel, T. et al., 2010]). By using $\mu = 2.42$ one can find that for this regime to hold for $1mm$ dust the gas density needs to be less than 1.8e-7. If this isn't the case, then one needs to use the Stokes regime instead. The Stokes regime is segmented into 3 other regimes, depending on the Reynolds number.

$$Re = \frac{2\rho_g|\mathbf{v}_{dg}| s}{\nu} = \frac{2|\mathbf{v}_{dg}| s}{\nu_{mol}} \tag{3.4}$$

Here s is the grain size and ν is the dynamic viscosity of the gas ([Weidenschilling, 1977]) and $\nu_{mol} = 0.5\bar{v}\lambda_{mfp}$ is the gas molecular viscosity ([Birnstiel, T. et al., 2010]). The Reynolds number describes if the flow is turbulent or Laminar. The drag coefficient are as follows ([Weidenschilling, 1977]).

$$C_D = \begin{cases} 24Re^{-1} & \text{for } Re < 1 \\ 24Re^{-0.6} & \text{for } 1 < Re < 800 \\ \dfrac{4}{9} & \text{for } Re > 800 \end{cases} \tag{3.5}$$

The transition form the Epstein regime to the Stokes regime is simply when the Epstein criteria breaks.

3.2.1 Stopping times

The different regimes of drag from equation (3.5) means that a particle in two different regimes feels 2 different forces and thus will be affected differently over different times. This can be described by a characteristic time called the stopping time, which can be constructed by taking the ratio between the momentum of the dust relative to the gas and the drag force of a particle ([Armitage, 2007, Weidenschilling, 1977]).

$$t_{stop} = \frac{|\mathbf{p}_{dg}|}{F_D} = \frac{8}{3} \frac{m_d|\mathbf{v}_{dg}|s}{C_D V_d \rho_g |\mathbf{v}_{dg}|^2} = \frac{8}{3} \frac{\rho_s s}{\rho_g C_D |\mathbf{v}_{dg}|} \tag{3.6}$$

$V_d = 4/3\pi s^3$ was used to get the stopping time in more usable terms. Here material density of the dust $\rho_s = 1.6g \ cm^{-3}$. By using the different drag coefficients form the two regimes, explicit stopping times can be constructed.

$$t_{stop} = \begin{cases} \dfrac{\rho_s s}{\rho_g \bar{v}} & \text{for } s < \dfrac{9}{4}\lambda_{mfp} \\ \dfrac{2}{9}\dfrac{\rho_s s^2}{\nu_{mol}\rho_g} & \text{for } Re \leq 1 \\ \dfrac{2^{0.6}}{9}\dfrac{s^{1.6} \rho_s}{\nu_{mol}^{0.6}\rho_g|\mathbf{v}_{dg}|^{0.4}} & \text{for } Re \in\,]1,800[\\ 6\dfrac{\rho_s s}{|\mathbf{v}_{dg}|\rho_g} & \text{for } Re \geq 800 \end{cases} \tag{3.7}$$

3.3 Estimating a stokes number in a prestellar core

It is obvious from equation (3.7), that the stopping times for a dust particle depends on the grain size. This naturally means that a dust size of $1mm$ couples to the gas on another timescale than $1\mu m$, and thus the timescale one considers dictates which particles will drift. The Stokes number can be used here to indicate the coupling of a dust particle. Normally the stokes number is taken as the stopping time over the dynamical timescale of the system.

$$St = \frac{t_{stop}}{t_{dyn}} \tag{3.8}$$

The dynamical time scale is normally taken as the turn-over-eddy time also called the vortex time, which is the case for a protostellar disk [Birnstiel et al., 2010]. However in a collapsing prestellar core it would be more fitting to us the free-fall time of the system, as it indicate the time for the gravitational sink to collect all the surround material.

$$t_{dyn} = t_{ff} = \sqrt{\frac{3\pi}{32G\rho_g}} \tag{3.9}$$

Using the defined stopping times from equation (3.7) one can obtain the stokes number for the Epstien and Stokes regimes.

$$St = t_{stop}\sqrt{\frac{32G\rho_g}{3\pi}} = \begin{cases} \sqrt{\frac{32G}{3\pi\rho_g}}\frac{\rho_s s}{\bar{v}} & \text{for } s < \frac{9}{4}\lambda_{mfp} \\[2ex] \frac{2}{9}\sqrt{\frac{32G}{3\pi\rho_g}}\frac{\rho_s\, s^2}{v_{mol}} & \text{for } Re \leq 1 \\[2ex] \frac{2^{0.6}}{9}\sqrt{\frac{32G}{3\pi}}\frac{s^{1.6}\,\rho_s}{v_{mol}^{0.6}\rho_g^{1/2}|\mathbf{v}_{dg}|^{0.4}} & \text{for } Re \in\,]1{,}800[\\[2ex] \sqrt{\frac{384G}{\pi\rho_g}}\frac{\rho_s s}{|\mathbf{v}_{dg}|} & \text{for } Re \geq 800 \end{cases} \tag{3.10}$$

For some context a small stokes number of eg. 1e-4 will over the timescale of a t_{ff} act as coupled to the gas, as the stopping time is much shorter. Inversely a larger stokes number of eg. 5 will not couple couple that much, and will not stray from its path that much if any. The dynamics becomes quite interesting when $St \approx 1$. For here the particle will be affected enough for its path to change, but not enough to couple to act as the gas. Dust particles will then, in the case of a prestellar core, settle towards the center of the sphere.

The stokes number is affected by the the physical parameters of the environment. In the case of the Epstein regime it will depends on the gas density, and the temperature though the thermal velocity $\bar{v}$. This means that doing a collapse where both the temperature and gas density will rise, the stokes number will fall and thus larger particles will begin to couple to the gas.

$$S_t \propto \frac{1}{\sqrt{T(r)\rho_g(r)}} \tag{3.11}$$

3.4 Solving the movement of dust under the affect of drag

To evolve the particles in time under the effects of drag, we consider newtons second law of motion. Here we consider the perspective of a singular gas particle. We assume that only gravity and drag act on the particle.

$$\mathbf{a} = \frac{\mathbf{F}_{tot}}{m_d} = \mathbf{g} + \frac{\mathbf{F}_d}{m_d}\frac{\mathbf{v}_{dg}}{|\mathbf{v}_{dg}|} = \mathbf{g} - \frac{\mathbf{v}_{dg}}{t_{stop}} \tag{3.12}$$

Equation (3.12) can be written as a set of ODEs for the velocity and the spatial coordinates.

$$\frac{d\mathbf{x}_d}{dt} = \mathbf{v}_d \tag{3.13}$$

$$\frac{d\mathbf{v}_d}{dt} = \mathbf{g} - \frac{\mathbf{v}_{dg}}{t_{stop}} \tag{3.14}$$

The stopping time depends on time in a collapse, through quite a few parameters like gas density. This means that equation (3.13) and equation (3.14) can't be solved analytically. Here the time derivatives are approximated with a first-order-accurate backwards finite difference method.

$$\mathbf{x}^{n+1} = \mathbf{x}^n + \Delta t \mathbf{v}_d^{n+1} \tag{3.15}$$

$$\frac{\mathbf{v}_d^{n+1} - \mathbf{v}_d^n}{\Delta t} = \mathbf{g}^{n+1} - A_d^{n+1} \left[\mathbf{v}_d^{n+1} - \mathbf{v_g}^{n+1} \right] \tag{3.16}$$

To make the velocity scheme nicer to look, in terms of numerical notation, we define here $A \equiv t_{stop}^{-1}$, . Here one can see that the position of the particle can be calculated by first calculating the next step for the velocity. This means that we just need to find an expression for the next velocity step. To do this we define $\Delta \mathbf{v}_d = \mathbf{v}_d^{n+1} - \mathbf{v}_d^n$.

$$\frac{\Delta \mathbf{v}_d}{\Delta t} = \mathbf{g}^{n+1} - A_d^{n+1} \left[\Delta \mathbf{v}_d + \mathbf{v}_d^n - \mathbf{v}_g^n \right] \Leftrightarrow \tag{3.17}$$

$$\Delta \mathbf{v}_d = \frac{\Delta t}{1 + \Delta t A^{n+1}} \left(\mathbf{g}^{n+1} - A^{n+1} \left[\mathbf{v}_d^n - \mathbf{v}_g^{n+1} \right] \right) \tag{3.18}$$

We now insert this into our the definition for $\Delta \mathbf{v}_d$, thus obtaining the update scheme for the velocity.

$$\mathbf{v}_d^{n+1} = \mathbf{v}_d^n + \frac{\Delta t}{1 + \Delta t A^{n+1}} \left(\mathbf{g}^{n+1} - A^{n+1} \left[\mathbf{v}_d^n - \mathbf{v}_g^{n+1} \right] \right) \tag{3.19}$$

Equation (3.19) is dependent on future values of the environment. If the environment is independent on the dust particles, then the environment can be evolved a step forward in time and then one can update the particles. In chapter 4, we will consider if the enviorment comes from a data set and thus comes in different time steps to the particles.

The choice of a backwards finite method for the time derivative, is largely from a stability point of view. The backwards method is numerically stable for all time steps, meaning one doens't have to fear the simulation becoming numerically unstable [Heath, 2005]. The first-order accuracy of the version used is not a big problem the choice of integrator discussed in the next subsection, increases the accuracy of the integration to second order.

3.4.1 Leapfrog method

As the particles are affected by gravity they will have orbital motions. Due to this the symplectic leaping frog (SLF) integration is chosen to evolve the particles. The benefit of the SLF method is that i conserve the energy in an orbit to a good approximation ([Quinn et al., 1997, Springel, 2005]). SLF works by using 2 operators. The kick (K) operator which updates the velocity and the drift (D) opertor which updates the position. These operators are placed in a *KDK* formation, where the kick is half a time step each.

$$\text{K}(\Delta t): v^{n+1} = v^n + \Delta t \, a(x^n) \tag{3.20}$$

$$\text{D}(\Delta t): x^{n+1} = x^n + \Delta t \, v_n^{n+1} \tag{3.21}$$

$$\text{KDK}: \text{K}(\Delta t/2)\text{D}(\Delta t)\text{K}(\Delta t/2) \tag{3.22}$$
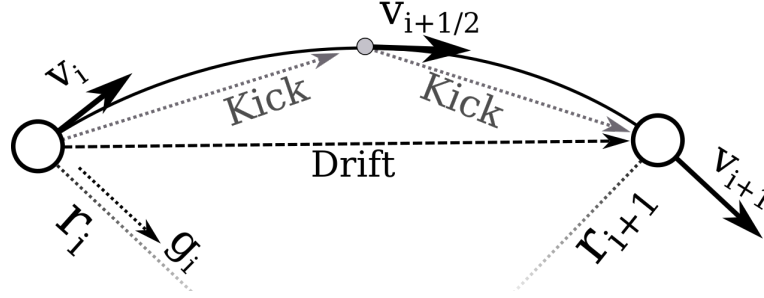
Figure 3.1: Illustration of a leaping frog, KDK variant, integrating on an orbit. Here v_i is the current velocity to at time step i, $v_{i+1/2}$ is the velocity at half a time step forward calculated from a kick, v_i is the velocity after a full time step, and is calculated from a second kick.

This is illustrated in figure 3.1. Here the arrows dictate the update of the velocity and spacial coordinates. For the dust particles affected by drag as per equation (3.19) the full SLF scheme becomes (future values are evaluated at $t + \Delta t/2$):

$$\text{Kick: } \mathbf{v}_d^{n+\frac{1}{2}} = \mathbf{v}_d^n + \frac{\Delta t}{2 + \Delta t A^{n+\frac{1}{2}}} \left(\mathbf{g}^{n+\frac{1}{2}} - A^{n+\frac{1}{2}} \left[\mathbf{v}_d^n - \mathbf{v}_g^{n+\frac{1}{2}} \right] \right) \tag{3.23}$$

$$\text{Drift: } \mathbf{x}^{n+1} = \mathbf{x}^n + \Delta t \mathbf{v}_d^{n+\frac{1}{2}} \tag{3.24}$$

$$\text{Kick: } \mathbf{v}_d^{n+1} = \mathbf{v}_d^{n+\frac{1}{2}} + \frac{\Delta t}{2 + \Delta t A^{n+1}} \left(\mathbf{g}^{n+1} - A^{n+1} \left[\mathbf{v}_d^n - \mathbf{v}_g^{n+1} \right] \right) \tag{3.25}$$

Comparing the energy conservation of the leapfrog integrator
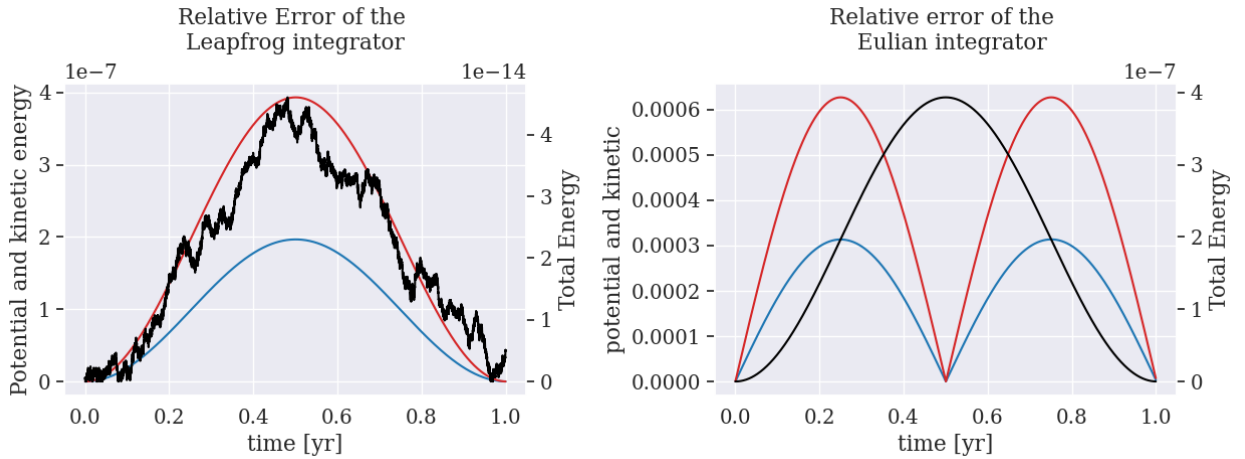
Figure 3.2: The potential energy is blue, the kinetic energy is red and the total energy is black. The left plot shows the relative error for the kinetic, gravitational and total energy of the leaping frog integrator, while the left is for a standard Eulian integrator. The drop of the Eulian integrator midway though is because the energy comes closer the the starting value, however here it comes near 10^{-6} which is still larger than the leapfrog integrator

As mentioned in section 3.4.1 the SLF method is good at conserving energy, especially for orbitals ([Quinn et al., 1997, Springel, 2005]). To compare this conservation of energy, we compare the KDK method with a eulian update scheme seen in equation (3.19) and equation (3.15). In both cases we initialize a system of a arbitrary object, referred to as planets, in a circular orbit around a sun like star with a radius of 1 AU, naturally we do not consider drag for this so $A = 0$. Both methods are elapsed for 1 year with a time stepping of $3156s \approx 1hr$.

Figure 3.2 shows the relative error of the potential, kinetic and total energy for both integrators. Here we see that the leaping frog integrator conserve energy better as the kinetic and potential energy are of order 10^{-7} at worst, while for the Euler integrator it is of order 10^{-4}. This is even more transparent with the total energy as the leapfrog is of order 10^{-14} which is one order of magnitude away from machine precision, while for the Euler its at 10^{-7} orders of magnitude. We also see that even with keplarian velocity, both integrators gives an orbit that is ever so slightly eplitical, as the energies have a bell trends. With this one can see that the SLF methods is a good choice for integrating the particles.

3.5 Coagulation and Fragmentation

The presented dust dynamics builds on the dusts interaction with gas, though an aerodynamic drag force. However dust can also interact with dust, and depending on the collusion it can fragment into smaller pieces or the grains can merge, fully or partially, into larger grains. These dynamics are quite important as larger particles can shatter into smaller pieces that will coupled more to the gas, and thus halting the transport of mass. Inversely smaller dust grains can growth to sizes where the coupling decrease and the mass can thus be transported more effective. For these reasons one must consider coagulation and fragmentation to grasp the full picture of the dynamics of dust. Sadly due to time constrains the implementation of coagulation and fragmentation wasn't implemented, so in this section the theory and discretization will more so be discussed.

3.5.1 Coagulation

Coagulation describes when two dust particles collide with each other and combine into a larger dust particle. To model this one uses the Smoluchowski equation, which describe how particles coagulate upon impact ([Birnstiel, T. et al., 2010, Elimelech et al., 1995]). In continuous form the equation is

$$\frac{\partial n(m_i,t)}{\partial t} = \frac{1}{2}\int_0^i K(m_i-m_j,m_j)n(m_j,t)n(m_i-m_j,t)\,dm_j - n(m_i,t)\int_0^\infty k(m_i,j)n(m_j,t)\,dm_j$$
(3.26)

Here the indexes i and j describe two different particles, where i is the one we want to find the evolution of though interation with various j particles. n is describes the number density of the particle, which is naturally defined as ρ/m. There first term on the RHS of the equation describes the creations of particle i from the coagulation of particle j and $k = i - j$. The factor of a half is to avoid double counting. The second term describe the removal of particle i because it is used to create another particle though coagulation. If we have well defined grain sizes then we can discretize equation (3.26) as a sum.

$$\frac{\partial n_i(t)}{\partial t} = \frac{1}{2}\sum_{j=0}^i K_{k,j}\,n_j(t)\,n_k(t) - n_i(t)\sum_{j=0}^N K_{i,j}\,n_j(t)$$
(3.27)

The coagulation kernel is depended on the relative velocity between particles $\Delta u(i,j)$, their effective cross section $\sigma(i,j) = \pi(s_i + s_j)^2$, and the probability of sticking togheter p_c ([Birnstiel, T. et al., 2010]).

$$K(i,j) = \Delta u(i,j)\sigma(i,j)p_c$$
(3.28)

The sticking probability will be touched more upon in section 3.5.2, together with the fragmentation probability

Podalak Algorithm

When two particles coagulate and we have predefined grain bins, there is the possibly that the newly created grain will not match them. So to conserve mass the new particle is split into the two closest bins. This is called the podalak algorithm ([Brauer et al., 2007]). Here one defines a collective term for interation.

$$G_{ij} = K_{ij}n_jn_j \tag{3.29}$$

Where K is the coagulation kernel, and n is the number density. This dictates the creation of a new mass $m = m_i + m_j$ which we assume doesn't perfectly match a bin. The new mass however is between the two bins of m_a and m_b where $m_a < m_b$. Now we split G_{ij} linearly into the two existing grain bins.

$$G_a = \varepsilon G_{i,j} \tag{3.30}$$

$$G_b = (1 - \varepsilon)G_{i,j} \tag{3.31}$$

Which conserves the number density of our particles as $G_a + G_b = G_{i,j}$. To enforce the conservation of mass we define

$$G_am_a + G_bm_b = G_{i,j}(m_i + m_j) \tag{3.32}$$

By inserting equation (3.30) and (3.31) into the above, we can obtain an expression for ε as a function of the mass or grain size.

$$\varepsilon = \frac{m_b - (m_i + m_j)}{m_b - m_a} = \frac{a_b^3 - (a_i^3 + a_j^3)}{a_b^3 - a_a^3} \tag{3.33}$$

If $m_i + m_j = m_b$ then $\varepsilon = 0$ and all the mass should be put into the m_b as per equation (3.31). A feature of this method is that ε only depends on the predefined bins, which means that in implementation one can define a look up table for grain interation. With this new scheme one can modify the Smoluchowski equation.

$$\frac{\partial n_i(t)}{\partial t} = \frac{1}{2}\sum_{j=0}^{i}G_{kj}\gamma_{ijk} - \sum_{j=0}^{N}G_{ij} \tag{3.34}$$

Where gamma is defined as

$$\gamma_{ijk} = \begin{cases} \varepsilon & \text{if } i = a \text{ for interation between k and j} \\ 1 - \varepsilon & \text{if } i = b \text{ for interation between k and j} \\ 0 & \text{else} \end{cases} \tag{3.35}$$

3.5.2 Fragmentation

Fragmentation is when two particles collide and shatter into smaller pieces, this can be a partial destruction or a complete destruction. This process is modelled in the same way as coagulation except the kernel is different.

$$L(i,j) = \Delta u(i,j)\sigma(i,j)p_f \tag{3.36}$$

Which then gives the following form of equation (3.27)

$$\frac{\partial n_i(t)}{\partial t} = \frac{1}{2}\sum_{j=0}^{i}L_{k,j}\,n_j(t)\,n_k(t)F(i,j,k) - n_i(t)\sum_{j=0}^{N}L_{i,j}\,n_j(t) \text{ where } k = i - j \tag{3.37}$$

When two particles collide and causes fragmentation, the result is not necessarily create a single particle that fits into the defined grain bins, akin to the coagulation. However fragmentation doesn't necessarily create a single particles, it will likely create many various sizes at

once. This distribution is handled by the $F(i,j,k)$ factor. The form of this distribution will not be talk about in this thesis, as time didn't permit much reading into the subject. However [Geretshauser, R. J. et al., 2011, Windmark, F. et al., 2012], could provide some great insight as they provide models for simulating fragmentation, erosion and mass transfer process, here [Windmark, F. et al., 2012] focuses on a grid based approach for usage in disk models while [Geretshauser, R. J. et al., 2011]focuses on a detailed grain to grain interaction. This also extends to the probabilities of fragmentation and coagulation, here they are defined by the velocities of the interacting grains and can account for the the various regimes in figure 1.1.

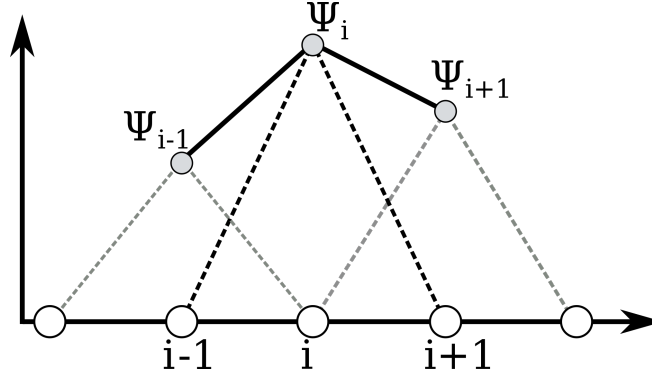### 3.5.3 Estimating Coagulation from existing data of a discrete environment

Figure 3.3: Illustration of the Galerkin approximation with liner shape functions. Here we have 3 discrete points located at i, i-1 and i+1. The dotted lines are each points individual shape function.

As time didn't permit the implementation and usage of disk growth effects wasn't tested, however a simpler approach to estimate when growth kicks in can be found. Here we follow the appendix in [Birnstiel, T. et al., 2010] with equation (3.38).

$$\frac{ds}{dt} = \frac{\rho_d}{\rho_s}\Delta u \tag{3.38}$$

Where s is the dust grain size, ρ_d is the dust mass density, ρ_s is the solid internal density in a dust grain, Δu is the velocity difference given by

$$\Delta u_{BM} = \sqrt{\frac{16 k_b T}{\pi m}} \tag{3.39}$$

$$\Delta u_{RD} = |u_r(m_1) - u_r(m_2)| \tag{3.40}$$

$$\Delta u_{TM} = \begin{cases} c_s\sqrt{2\alpha St} & \text{for } St \ll 1 \\ c_s\sqrt{\dfrac{2\alpha}{St}} & \text{for } St \gg 1 \end{cases} \tag{3.41}$$

Which are taken from redBauere 2010. Here the equation (3.39) is the relative velocity for Brownian motion for two similar sized particles. Equation (3.40) is the relative velocity for radial motion and equation (3.41) is the relative velocity based on the α viscosity model. The α model is used to parameterize the viscosity, and here $\alpha = 1e-4$ which is taken as a lower boundary as it should be higher.

Forward from here we are gonna consider the growth in eulian bins, ie. constant cell centers and width, and all quantaties of ρ_d and Δu are calculated from these either directly from the volume or by a mean estimation. This naturally introduces some errors into the method, in terms of scale, however it should affect when process kicks in. If we assume that the dust

density and relative velcity are constant over time then the solution to equation (3.38) becomes trivially simple. However this might not be the case, and we might not know the exact relation between a quantity and time. We therefore use a Galerkin approximation which is a way of interpolating though so called shape functions.

$$\psi(t) = \sum_{i=0}^{N} N_i(t)\hat{\psi}_i \tag{3.42}$$

Here $\hat{\psi}$ is the discrete point of some quantity and N_i is called the shape function. This shape function dictates the order of interpolation. For this work a linear shape function is chosen. This shape function is illustrated in figure 3.3 and is given by equation (3.43).

$$N_i(x) = \begin{cases} \dfrac{x - x_{i-1}}{x_i - x_{i-1}} & x_{i-1} \leq x \leq x_i \\[2mm] \dfrac{x_{i+1} - x}{x_{i+1} - x_i} & x_i < x \leq x_{i+1} \\[2mm] 0 & \text{else} \end{cases} \tag{3.43}$$

With this method one can simply write a physical quantity as a sum over discrete points connected by a shape function. The physical quantity of Δu can take different forms, and thus depend of time depended variables in different way, to find a common equation from which most combinations of Δu can be calculated, we assume a the velocity can be decomposition into 3 parts. Firstly the constants collected into C, the second part is the grain size dependencies,if any, collected into $\xi(s)$ and lastly the time dependent properties, which can be seen as a function, $Y(\psi(t))$, of some physical quantity ψ. Here we assume that Y is only dependent on a single physical property.

$$\Delta u = C\,\xi(s)Y(\psi(t)) \tag{3.44}$$

Inserting this into equation (3.38), and separating the parts depending on size and time. Furthermore integration limits of a starting time t_0 and arbitrary time of t is inserted.

$$\int_{s_0}^{s} \frac{1}{\xi(s')}ds' = \frac{C}{\rho_s}\int_{t_0}^{t} \rho_d(t')Y(\psi(t'))dt' \tag{3.45}$$

For the rest of this derivations the short hand notation of $t' = t$ is used. Here ρ_d and ψ can be approximated with equation (3.42) such that the integral can be evaluated. However as the chosen shape function is not well behaved over the time domain of $[t_0, t']$ as the equation (3.43) is not a continuous function on this domain. However one can utilize that integrals can be separated into an sum of integrals over a smaller sub domain. Here one just chooses to separate the integration domain into parts between each discrete point, eg. from $i - 1$ to i. For the shape function is well behaved within these sub domains.

$$\int_{t_0}^{t} \rho_d(t)Y(\psi(t))dt = \sum_{k=1}^{} \int_{t_{k-1}}^{t_k} \rho_d(t)Y(\psi(t))dt \tag{3.46}$$

We are now going to consider a small sub domain that lies in $[t_\alpha, t_\beta]$ where the edges of the sub domain have a corresponding ρ_d and ψ. The shape functions for α and β simplify in this domain.

$$N_\alpha = \frac{t_\beta - t}{t_\beta - t_\alpha} \wedge N_\beta = \frac{t - t_\alpha}{t_\beta - t_\alpha} \tag{3.47}$$

Equation (3.42) and (3.47) is then inserted into equation (3.46).

$$\int_{t_\beta}^{t_\alpha} \left[N_\alpha\hat{\rho}_{d,\alpha} + N_\beta\hat{\rho}_{d,\beta}\right] Y(N_\alpha\hat{\psi}_\alpha + N_\beta\hat{\psi}_\beta)dt \tag{3.48}$$

The expression of ψ and ρ_d can be cleaned up into a linear function by inserting the shape functions of equation (3.47).

$$\frac{t_\beta - t}{t_\beta - t_\alpha}\hat{\psi}_\alpha + \frac{t - t_\alpha}{t_\beta - t_\alpha}\hat{\psi}_\beta = \frac{\hat{\psi}_\beta - \hat{\psi}_\alpha}{t_\beta - t_\alpha}t + \frac{\hat{\psi}_\alpha t_\beta - t_\alpha \hat{\psi}_\beta}{t_\beta - t_\alpha} = A_\psi t + B_\psi \tag{3.49}$$

Here ψ is used for the purpose of generalization. The sub domain integral can now be written more neatly. A_ψ ,B_ψ,A_ρ and B_ρ are constants, and thus can be pulled out of the integral.

$$\int_{t_\beta}^{t_\alpha} \left[A_\rho t + B_\rho\right] Y(A_\psi t - B_\psi)\, dt = A_\rho \int_{t_\alpha}^{t_\beta} t\, Y(A_\psi t - B_\psi)\, dt + B_\rho \int_{t_\beta}^{t_\alpha} Y(A_\psi t - B_\psi)\, dt \tag{3.50}$$

Now equation (3.45) can be written in its final general form.

$$\int_{s_0}^{s} \frac{1}{\xi(s')}ds' = \frac{C}{\rho_s}\sum_{i=1}^{N}\left(A_\rho \int_{t_{i-1}}^{t_i} t\, Y(A_\psi t + B_\psi)\, dt + B_\rho \int_{t_{i-1}}^{t_i} Y(A_\psi t + B_\psi)\, dt\right) \tag{3.51}$$

Now schemes for coagulation can be found by decomposing equation (3.39), (3.40) and (3.41). This is done in appendix A, together with a convergence test for when the physical quantities becomes constant. For Brownian motion we get.

$$s_{BM}(t) = \left(\frac{5}{2\pi}\sqrt{\frac{12k_b}{\rho_s^3}}\sum_{i=1}^{N}Q_i + s_0^{5/2}\right)^{2/5} \tag{3.52}$$

$$Q_i = \frac{2}{5}\frac{A_\rho}{A_T^2}\left[(A_T t + B_T)^{5/2}\right]_{t_{i-1}}^{t_i} + \left(\frac{2}{3}\frac{B_\rho}{A_T} - \frac{2}{3}\frac{A_\rho B_T}{A_T^2}\right)\left[(A_T t + B_T)^{3/2}\right]_{t_{i-1}}^{t_i} \tag{3.53}$$

For relative velocities in the radial motion we get.

$$s_r(t) = \sum_{i=1}^{N}\left\{\frac{A_\rho A_r}{3\rho_s}\left[t^3\right]_{t_{i-1}}^{t_i} + \frac{B_r A_\rho + B_\rho A_r}{2\rho_s}\left[t^2\right]_{t_{i-1}}^{t_i} + \frac{B_r B_\rho}{\rho_s}\left[t\right]_{t_{i-1}}^{t_i}\right\} + s_0 \tag{3.54}$$

For α model turbulence we get.

$$s_{turb} = \begin{cases} \left[\left[\sqrt{\frac{\alpha}{2\rho_s}}\left(\frac{32Gk_b}{24\mu m_p}\right)^{1/4}\sum_{i=1}^{N}Q_i + s_0^{1/2}\right]^2 & \text{for } St \leq 1 \\[4mm] \left[\frac{3}{2}\sqrt{\frac{2\alpha}{\rho_s^3}}\left(\frac{24k_b^3}{32G\mu^3 m_p^3}\right)^{1/4}\sum_{i=1}^{N}Q_i + s_0^{3/2}\right]^{2/3} & \text{for } St > 1 \end{cases} \tag{3.55}$$

$$Q_i = \frac{2}{5}\frac{A_\rho}{A_{Se}^2}\left[(A_{Se}t + B_{Se})^{5/2}\right]_{t_{i-1}}^{t_i} + \left(\frac{2}{3}\frac{B_\rho}{A_{Se}} - \frac{2}{3}\frac{A_\rho B_{Se}}{A_{Se}^2}\right)\left[(A_{Se}t + B_{Se})^{3/2}\right]_{t_{i-1}}^{t_i} \tag{3.56}$$

Here the variable Se is given a collected physical quantity given by equation (3.57).

$$Se = \begin{cases} \rho_g^{-1}T^{1/2} & \text{for } St \leq 1 \\[3mm] \rho_g^{1/2}T^{3/2} & \text{for } St > 1 \end{cases} \tag{3.57}$$

This quantity was defined as handling both the interpolation of gas density and temperature becomes quite a mess, and way to complex.
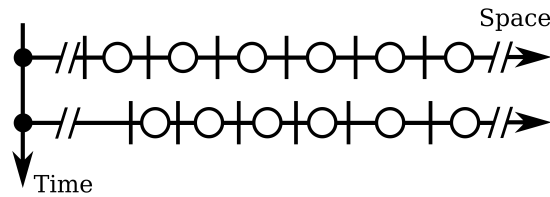
Dust dynamics in a background model

Figure 4.1: Simple illustration of a Lagrangian mesh. Here the white dots are representing the cell centers, and the vertical black bars are the interfaces/edges of the cells. Here we can see that the cells have moved as time integrates.

The effects of radiation and rotation on a prestellar core can be quite important as presented in Section 2.2. Unfortunately they are quite computationally expensive to simulate, and can also be hard to implement which would be outside the scope of this thesis. In order to have a realistic collapse of the presteallar core a background model is chosen. This background model is taken from [Vaytet and Haugbølle, 2017]. This article creates a data base for a 1D spherically symmetric, radative collapse of prestellar cores at different mass, radius and temperature for different times.

The data are allocated in 4096 cells for a varying amount of snapshots that depends on the formation of the second Larson core. Here interpolation is used to "fill" the space between sphere cells. For all variables linear interpolation is used except for the mass which is interpolated linearly in its cubic root. This is due to us knowing that the mass in the center of the sphere goes $M = \rho V^3 \propto r^3$ as the density is constant, and thus we know that it is linear in the cubic root. The benefit of the having data is that each interpolation scheme can be constructed when starting the program.

The data from [Vaytet and Haugbølle, 2017] used a Lagrangian mesh meaning that its cells location and width is not constant, but does in fact change over time. This is illustrated in figure 4.1. This choice of mesh needs a correction which is discussed in section 4.2.

The disadvantage of this approach is that it introduces truncation errors from the choice of interpolation, furthermore the data only contains discrete time stepping values form which the time stepping can be rather large.

As seen in section 3.4, the integration scheme for the particles depends on future variables. To obtain these variables for the background model one just has to estimate the placement of the particle position at $\Delta t = 1/2$, with the usage of the current velocity. In other words $r^{i+1/2} = r^i + 0.5\Delta t v_r^i$. This radius can then be used to interpolate the data from the background model.

4.1 Integrating between snapshots

As the background model comes in snapshots, an approach is needed to handle when to switch from eg. snapshot 41 to 42. The approach also needs to take into account the varying time stepping that each particle can have. So in short the approach should synchronise the particles at a given time and then switch the snapshot. Here there are 2 obvious choices, the first is to evolve the particles from snapshot time to snapshot time. The second is to synchronise that particles at the midpoint in time between two snapshots. One can argue that the latter approach is more accurate as we should be close to the next snapshot at the midpoint. This method however was not used, as it was only thought of when it was too late to change in terms of the deadline of the thesis. So for the rest of this thesis the first approach is used.

In order to synchronise the particles to a given time one can assume that each particle has a individual time step for their integration, usually calculated by a courant condition. Furthere more one can assume that the snapshots are given in a set of data $t_n = [t_0, t_1, t_2, ..., t_{N-1}]$, where N is the total amount of snapshot. Here a new time stepping criteria can be constructed such that each particle will arrive at the correct snapshot time.

$$\Delta t_p = \min(\Delta t_{courant}, t_{i+1} - t_p) \tag{4.1}$$

Here t_p is the time that the particles is located at and the time index i is the current snapshot and t_{i+1} is the time of the next snapshot. So if $\Delta t_{courant}$ is larger than the remaining time of the snapshot, then we use the remaining time. This is illustrated in figure 4.2
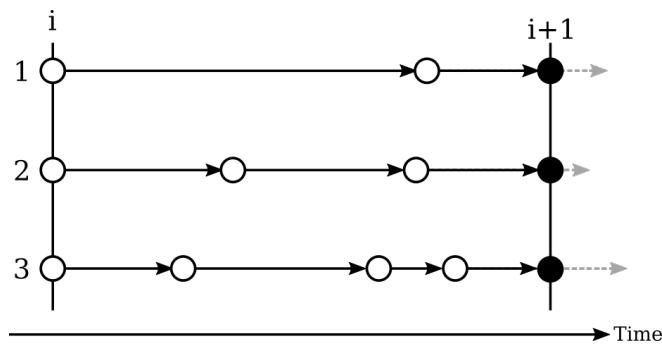

Figure 4.2: This illustration shows 3 particles starting at snapshot i, and are then integrated for snapshot $i + 1$. Here the solid black lines before the last particle white particle indicate the the courant time step, the black lines between the solid black dot, the white dot indicate $t_{i+1} - t_p$, and the grey transparent arrows indicate where the particles would have jumped if the kept using their courant condition.

4.2 Particle interpolation in a Lagrangian mesh

Because the background model uses a Lagrangian mesh, the movement of the cells needs to be accounted for when integrating between snapshots, as the cells also would have moved with their velocity. Here one could do some time interpolation of the cells, and then input the time of the particle, this however would be quite hard and time consuming to do in code as the interpolation schemes used for the physical parameters needs to be updated which can cost in terms of performance. Another approach would be a transformation from the perspective of the particle to the perspective of the cells. This approach is chosen as it one would just need to translate the particles and thus the already existing interpolation schemes can be utilized without chance.

To construct the translation scheme we consider the linear interpolation used between two
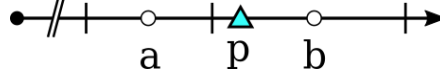
Figure 4.3: Simple illustration that shows the cells 'a' and 'b' where a macro particle is located at 'p'

cells a and b, with a particle p between their centers, as illustrated in figure 4.3. A Galerkin approximation is used, like subsection 3.5.3, for the interpolation. The interpolation part from cell *a* for particle *p* between cell *a* and *b* is given as the following.

$$f = \frac{r_{p,c} - r_a}{r_b - r_a} = \frac{r_{p,c} - r_a}{\Delta r} \tag{4.2}$$

This is the interpolation fraction for the rest frame of the cells, and the position of the particle here is given by $r_{p,c}$. The interpolation fraction for particles rest frame can be written as.

$$f = \frac{r_p - (r_a + Dt v_a)}{r_b + Dt v_b - (r_a + Dt v_a)} = \frac{r_p - r_a - Dt v_a}{\Delta r + Dt \Delta v} \tag{4.3}$$

Here the positions of the cell centers are moved forward with their current snapshot velocity at a time $Dt = t_p - t_i$, where t_p is the time of the particle and t_i is the current snapshot time, the notation Dt is to not confuse the time step used in this scheme for the integration time step of Δt. The two interpolations fractions should be the same in both rest frames, or else the it wouldn't be the same interpolation.

$$\frac{r_{p,c} - r_a}{\Delta r} = \frac{r_p - r_a - Dt v_a}{\Delta r + Dt \Delta v}$$

This can now be solved for the particles position in the rest frame of the cells.

$$r_{p,c} = r_a + \frac{\Delta r}{\Delta r + Dt \Delta v}(r_p - r_a - Dt v_a) = \beta r_p + (1 - \beta) r_a - \beta Dt v_a \tag{4.4}$$

Here β can be seen as a squish or stretch factor of the cells, and when it has the value of 1, ie the cells move at the same velocity, then the scheme collapses to a Galilean transformation.

$$r_{p,c} = r_p - \beta Dt v_a \text{ for } \beta = 1 \tag{4.5}$$

This scheme was found from the interpolation with respect to cell *a*, this could also have been with respect to the cell *b* where the fraction would be given as $1 - f$.

$$r_{p,c} = \beta r_p + (1 - \beta) r_b - \beta Dt v_b \tag{4.6}$$

There are 2 edge cases at cell 0 and cell N as they have no neighbors at respectively the left and right size. The solution for this is rather simple as one can place ghost cells as neighbors that have the same velocity as cell 0 or cell N. This means that $\beta = 1$ thus at the boundaries a Galilean transformation is used. This then gives the final correction scheme.

$$r_{p,cell} = \begin{cases} r_p - Dt v_a & \text{for cell N} \\ r_p - Dt v_b & \text{for cell 0} \\ \beta r_p + (1 - \beta) r_a - \beta Dt v_a & \text{else} \end{cases} \tag{4.7}$$

Here the choice of using equation (4.4) for all other points comes from that it was easier to implement in code with the written setup.

4.3 Depositing particles into radial cells

A useful ability to have when processing the data from the dust simulations is to map particles to the radial cells from [Vaytet and Haugbølle, 2017], as this allows us to calculate the dust to gas ratio of the system. The most naive way to do this is to just check if a particle is within a cell and then just count that as completely belonging to that cell. While this works it a bit deceiving, as the macro particles would have a volume, and thus aren't just points in space. This means that if we have macro particle located ever so closely to the interface then some of its volume would be in both cell i and cell j, and thus it would be wrong to say that the particle belongs to either i or j. Instead one could use a PIC scheme represented in [Ruyten,
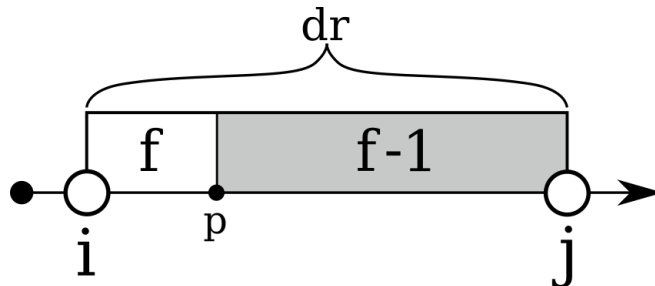

Figure 4.4: Illustration for the depositing of particle mass. Here we consider the two cell centers i and j with a particle p between them. Here we have the fraction f going to the point j and the fraction $1 - f$ going to the point i as it is the particle p is closer to the center i

1993]. Here we assume that the volume of the particles fills the space between cell i and j called $dr = r_j - r_i$. We can then here define a fraction which describe how much space goes to cell i and cell j.

$$f = \frac{r_p - r_i}{dr} \text{ where } r_j > r_p > r_i \tag{4.8}$$

Here we see that if $f = 0$ then $r_p = r_i$, this means that we need to deposit all of r_p into cell i, while if $f = 1$ then we need to deposit all into cell j. To better visualize this splitting of volume, we can look at figure 4.4. Where the particle p placed between cell i and j, here the grey shaded area shows the area covered by $1 - f$, which means this is the fraction volume belonging to cell i and the white area belongs to cell j.

With this we can now split the mass or any property of the particle between two cells, simply my multiplying the corresponding volume fraction with the property we want to split.

$$m_i = m_i + (1 - f) \, m_p \tag{4.9}$$
$$m_j = m_j + f \, m_p \tag{4.10}$$
$$\tag{4.11}$$

There is a boundary case for this we are in the first or last cell and we are on the side of the center that has no neighbor. Here we simply say that if we are placed at these boundaries then the entire particle belongs to the first or last cell.

4.4 Distribution dust in a background model

In the ISM there exist various types of dust, and they are given by a distribution of the form below

$$\frac{dn}{d \ln s} = g(s) \tag{4.12}$$

This describes the number of particles n there is at a given grain size s. The grain size is discretized into bins, such that is is easier to model on a computer. This is illustrated on figure
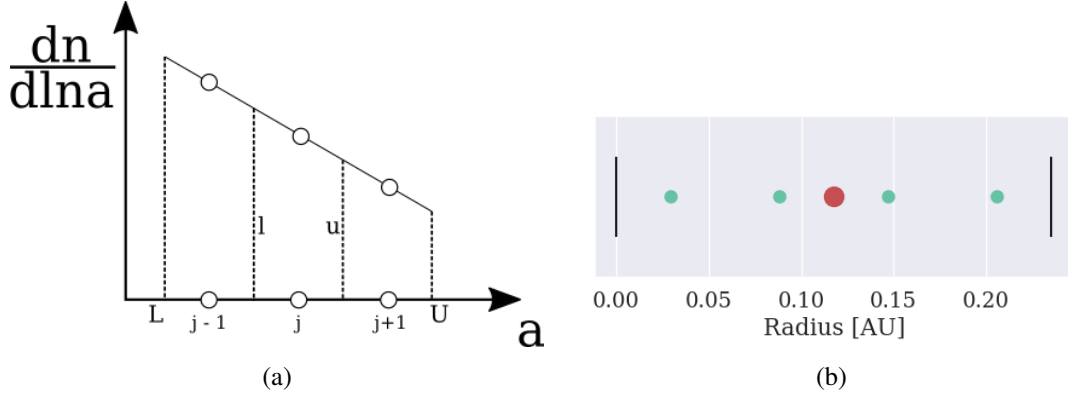
Figure 4.5: **a)** Illustration showing how one can discreize the dust distribution function into, grain size bins. Here a focus on a center cell j, with is t wo neighbors $j-1$ and $j+1$. The edges between j and its neighbors are called l and u, while the lowest bin edge and highest bin edge of the first and last bins are called U and L **b)** Here is shown the dusts spacial distribution given by equation (4.20) for a single cell. Here the black vertical lines are the cells interfaces, the green dots are the particles and the red dot is the center of the cell.

4.5a. The number density can be obtained for a chosen range going from L to U of dust by integrating equation (4.12)

$$n = \int_L^U \frac{dn}{d\ln s}\ d\ln s \tag{4.13}$$

As the grains are distributed into bins one can obtain the number density in each bin by integrating over the bins width.

$$n_i = \int_l^u \frac{dn}{d\ln s}\ d\ln s \tag{4.14}$$

Here l and u is the lower and upper limit of the cell, so $u-l$ is the cell width. The number density can be linked to the dust mass density by integrating over the grain sizes. Here we take that the mass is given by $m_d = 4\pi/3\ s^3\rho_s$, where ρ_s is again the material dust density take to be $1.6 g cm^{-3}$. With this the dust mass density for a single grain bin is.

$$\rho_{d,j} = \int_l^u m_d \frac{dn}{d\ln s}\ d\ln s = \frac{4}{3}\pi\rho_s \int_l^u s^3 \frac{dn}{d\ln s}\ d\ln s \tag{4.15}$$

$$= \frac{4\pi}{3}\rho_s \int_l^u \frac{dn}{d\ln s} s^2\ da = \frac{4\pi}{3}\rho_s \int_l^u g(s)\ s^2\ da \tag{4.16}$$

This can also be done for a total dust mass density by going over the limits of L and U. From the total and the bin wise density a fraction of how much density or mass each bin has can be constructed.

$$f_j = \frac{\rho_{d,j}}{\rho_{d,total}} = \frac{\int_l^u g(a)\ a^2\ da}{\int_L^U g(a)\ a^2\ da} \tag{4.17}$$

Here all the constant are the same, and thus only the integrals are left. The amount of mass the macro particles needs to be allocated a given dust to gas ratio, can found by multiplying the fraction from equation (4.17) with the total dust mass in each of the presteallar cores cells. This is given by the mass of the gas in each cell, and a chosen inital dust to gas ratio.

$$\Delta m_{d,i} = \mathscr{D}\Delta m_{g,i} \tag{4.18}$$

$$\Delta m_{i,j} = \Delta m_{d,i} f_j = \mathscr{D}\Delta m_{g,i}\ f_j \tag{4.19}$$

Here the index i refer to the radial cells of the presteallar core while the j index refer to which grain bin we need the mass for.

The flaw with this scheme is that $\Delta m_{g,i}$ is located at the center of the radial cell, so the particles need to start in the center. This is not that practical as distributing dust throughout a radial cell, which can help smooth the simulation output. To overcome this we are gonna subdivide the cell into smaller volumes that each particles initially governs. Here the particles are placed eqidistantly in a cell.

$$r_m = r_e + \left(k - \frac{1}{2} \right) \frac{dr}{N} \tag{4.20}$$

Here r_e is the lowest interface of a radial cell. N is the total number of particles in each cell meaning that the total amount of particles is $N \cdot \#cells$. k is the particle index going in the given cell from $[1, N]$ and dr is the width of the radial cell. This radial distribution is shown in figure 4.5b. If there is only 1 particle pr cell, $N = 1$, then it will be place in the center of the cells given by $r_e + dr/2$. These new sub cells all have a volume given by

$$V_m = \frac{4}{3} \pi \left[\left(r_m + \frac{dr}{2N} \right)^3 - \left(r_m - \frac{dr}{2N} \right)^3 \right] \tag{4.21}$$

It is assumed that each sub cell is also a spherical shell. The mass in each sub cell can be found by taking the gas density in the center of the sub cell and multipying it with the volume. This then give a new mass scheme

$$p_m = \mathscr{D} f_j \rho_g(r_m) V_m \tag{4.22}$$

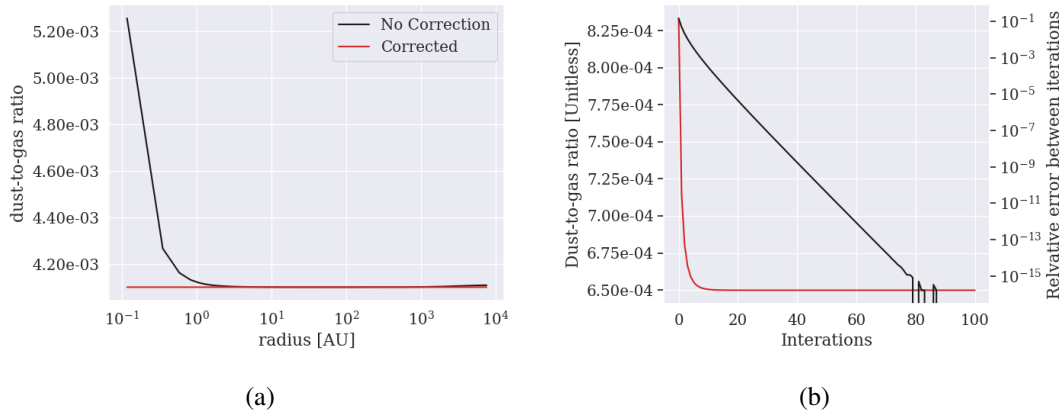(a)   (b)

Figure 4.6: **a)** shows the the dust to gas ratio before and after correction from equation (4.23), here it is obvious that the inner most cells gain more mass from the dust to the displacement of particles. After the correction the dust to gas ratio is constant through out the cells. **b)** The red line is dust-to-gas ratio for the inner most cell from **a**, while the black line is the error between each iterations, here one can see that after 80 iterations the change is less than machine precision.

The problems with the scheme is not over, for while the new mass scheme more correctly assigns mass to cell distributed particles, it does however have a problem with how particle mass is mapped to the radial cells described in section 4.3. Here there is a net gain to the left of mass to the left, as can be seen on with the black line in figure 4.6a. This can however be fixed rather easily by using a pseudo integrative method. Since we know how much dust mass there should be in every radial cell, we can modify the deposition method described in section 4.3.

$$p_m \leftarrow (1 - f) \mathscr{D} \frac{M_{req}^n}{M_{curr}^n} p_m + f \mathscr{D} \frac{M_{req}^{n+1}}{M_{curr}^{n+1}} p_m \quad \text{for } r_p > r_n \tag{4.23}$$

This here is an update scheme to a single particles mass based on what the mass should be in cell n M_{req}^n and cell $n+1$, the current mass of a cell M_{curr}^n and cell $n+1$ and the split factor into each cell with f which is assumed to be the same as discussed later in section 4.3. The correction done by this iterative method can be seen in figure 4.6a as the flat red line. A convergence figure can be seen on figure 4.6b, where it is one can see that the scheme fully converges to near machine precision at around 80 iterations.

MRN dustribution

A common choice of dust distribution is the MRN distribution ([Mathis et al., 1977]).

$$\frac{dn}{d\ln a} = Na^{-2.5} = g(x) \tag{4.24}$$

Equation (4.17) can now be calculated, so the distribution can be used in code.

$$\int_l^u a^{-2.5}\, a^2\ da = \int_l^u a^{-0.5}\ da = 2\sqrt{u} - 2\sqrt{l} \tag{4.25}$$

The dust size fraction can now be constructed by inserting equation (4.25) into equation (4.17) with the correct boundaries.

$$f_j = \frac{\sqrt{u} - \sqrt{l}}{\sqrt{U} - \sqrt{L}} \tag{4.26}$$

For the rest of the report it is assumed that the MRN distribution is used, unless stated otherwise.

4.5 Courant condition for the particles based on the background model

The particles inside of a presteallar core or any environment can experience different accelerations, move through cells of varying size etc. It is therefore important to take these parameters into account when doing a numerical integration as there is a risk of eg. moving over important cells. This can be done by calculating multiple courant conditions based on the characteristic parameters of the system. For background model 4 courant conditions where found to govern most situations. The first is based on the width of the cells the particle is currently located at, and the acceleration that it fells.

$$\Delta t_{dr} = C_{dr}\sqrt{\frac{2\,dr}{a_p}} \quad \text{where} \quad C_{dr} \in \ ]0,1] \tag{4.27}$$

Here the value of $C_{dr} \in [0,1]$ is used to parameters this courant condition, such that the importance of the criteria can be adjusted. Each criteria have their own parameter. This criteria ensures that a particle cant jump or skip an entire cell.

The second criteria is based on the backgrounds models snapshot times, in otherwords the spheres own time stepping.

$$\Delta t_{snap} = C_{snap}\,(t_{i+1} - t_i) \quad \text{where} \quad C_{snap} \in \ ]0,1] \tag{4.28}$$

This one here ensures that the particle can't move further than a single snapshot and thus skipping and important part of its interactions.

The third conditons is basde on the keplarian velocity of the particle and the is radial position.

$$\Delta t_{kep} = C_{kep}\frac{r_p}{v_{kep}(r_p)} = C_{kep}\sqrt{\frac{r_p^3}{G\,M_{sphere}(r_p)}} \quad \text{where} \quad C_{kep} \in \ ]0,1] \tag{4.29}$$

This criteria ensures that the particle can't take a time step such that i has moved around a orbital. There is missing a factor of 2π, but these are somewhat rolled into the courant constant.

The last criteria is based on gravity through the free-fall time.

$$\Delta t_{ff} = C_{ff}\, t_{ff}(r_p) = C_{ff}\sqrt{\frac{3\pi}{32G\rho_{sphere}(r_p)}} \quad \text{where} \quad C_{ff} \in \,]0,1] \tag{4.30}$$

This criteria stops the particle from taking a step larger than the free-fall time, which is the dynamcial timescale of the system. The time step for the particle then becomes the minimal courant time step.

$$\Delta t_{courant} = \min(\Delta t_{dr}, \Delta t_{snap}, \Delta t_{kep}, \Delta t_{ff}) \tag{4.31}$$

This can then be inserted into equation (4.1), to get the final time step that the particle can take for the integration.

$$\Delta t_p = \min(\Delta t_{dr}, \Delta t_{snap}, \Delta t_{kep}, \Delta t_{ff}, t_{i+1} - t_p) \tag{4.32}$$

4.6 Velocity distribution as a function of grain size

When a filament collapses into a presteallar core, there will be movement of gas and dust. However not every dust grain is handled equally due to drag forces, so it is expected that smaller grains that are more coupled will move at the same velocities as the gas. To create a model for the initial conditions for dust particle velocity one consider the Zoom-in simulation from [Kuffmeier et al., 2017]. In this article the author looks at the formation of a protoplanetary disk from giant molecular clouds (GMC). In here there are 2 figures of interest, that of figure 4 and 8. These figure show respectively the density profile of their cores and their specific angular momentum.
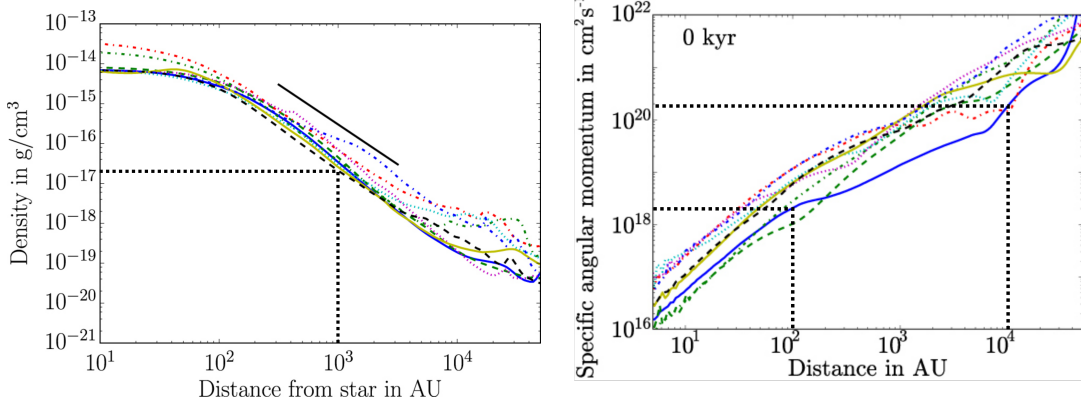
(a) Figure 4 from [Kuffmeier et al., 2017] (b) Figure 8 from [Kuffmeier et al., 2017]

Figure 4.7: The figures are are respectively figure 4 and figure 8 from [Kuffmeier et al., 2017]. The black dotted lines going from the x-axis to the y-axis are added in post as helping lines to read the data used in section 4.6

Firstly a power law is fitted to figure 4.7a for the outer regions where the density goes as $\rho_g \propto r^{-2}$. For the fit the following values was read off the graph $1e3\,AU$ the density is roughly $2e\text{-}17\,g cm^{-3}$.

$$\rho_g = \rho_0(r/AU)^{-2} \Rightarrow \rho_0 = 2\cdot 10^{-17}\cdot 10^6\frac{g}{cm^3} = 2*10^{-11}\frac{g}{cm^3} \tag{4.33}$$

From the fitted density a mass for can be constructed as a function of radius.

$$M(r) = 4\pi\int_0^r r^2\rho_g(r)dr = 4\pi\rho_0 AU^2 r \tag{4.34}$$

From this the keplarian velcoity for the core can be estimated.

$$v_{kep} = \sqrt{\frac{GM(r)}{r}} = \sqrt{4\pi G \rho_0 AU^2} \approx 613 m/s \qquad (4.35)$$

This will be used a bit later to parameters the azimuthal velocity from the specific angular momentum.

To estimate the azimuthal velocity from the angular momentum we assume that r and v_ϕ is orthogonal thus $j = rv_\phi$. From figure 8 in [Kuffmeier et al., 2017] one can read that

$$j(100AU) \approx 2 \cdot 10^{18} \frac{cm^2}{s^{-1}}$$

$$j(1e4AU) \approx 2 \cdot 10^{20} \frac{cm^2}{s^{-1}}$$

Which resaullts in the following azimuthal velocities.

$$j = rv_\phi \Leftrightarrow v_\phi = \frac{j}{r} \approx \begin{cases} 13.36ms^{-1} & \text{for } r = 100AU \\ 13.36ms^{-1} & \text{for } r = 1e4AU \end{cases} \qquad (4.36)$$

This means that the azimuthal velocity is constant throughout the outer parts of the sphere for coupled particles. To apply this to other spheres we parameterize the azimuthal velocity with the keplarian velocity.

$$\frac{v_\phi}{v_{kep}} = \frac{13.36ms^{-1}}{613ms^{-1}} \approx 2.2\% \Leftrightarrow v_\phi = 2.2\% v_{kep} \qquad (4.37)$$

This means that coupled particles should be initialized with 2.2% of their keplarian velocities. To expand this to potentially lesser coupled particles one can consider finding the critically coupled grain sizes for the ISM through the larson relations.

$$n = 2000 cm^{-3} \frac{1pc}{L} \Leftrightarrow nL = 2000 cm^{-3} pc \qquad (4.38)$$

Here nL is the column density. The number of gas particles, and by extention the gas mass, inside the cross section of a dust particles can then be found, in other words how many gas particles are in the way of the dust particles as it move in a straight line.

$$N_{gas} = A_s nL = 2000 cm^{-3} 1pc \, \pi s^2 \Rightarrow \qquad (4.39)$$

$$M_{gas} = N_{gas} \mu m_p = 2000 cm^{-3} 1pc \, \pi s^2 \mu m_p \qquad (4.40)$$

The mass of a dust particle is

$$M_s = \rho_s \frac{4}{3} \pi s^3$$

For a dust particle to come to a stop, it needs to hit an amount of gas equal to its own mass. So by setting the dust mass and the gas mass equal, a critically coupled particle size can be found.

$$M_s = \rho_s \frac{4}{3} \pi s^3 = 2000 cm^{-3} 1pc \, \pi s^2 \mu m_p = M_g \Leftrightarrow \qquad (4.41)$$

$$s = \frac{3}{4} \frac{2000 cm^{-3} \mu m_p}{\rho_s} 1pc \approx 117 \mu m \qquad (4.42)$$

Here $\mu = 2.42$ and $\rho_s = 1.6g/cm^3$. This means that a grain size of $117\mu m$ is on the border of coupling in the phases before the prestellar core formation. Because of this we choose that a size of $\sim 117\mu m$ gets a inital azimuthal velocity equal to its keplerian velocity. Now that an upper and lower bound on the velocity have been found, one can use linear interpolation to get a distribution of initial azimuths velocity.
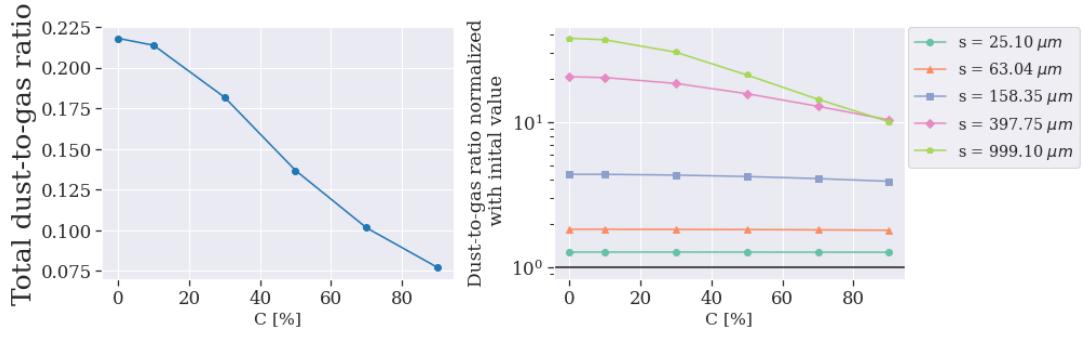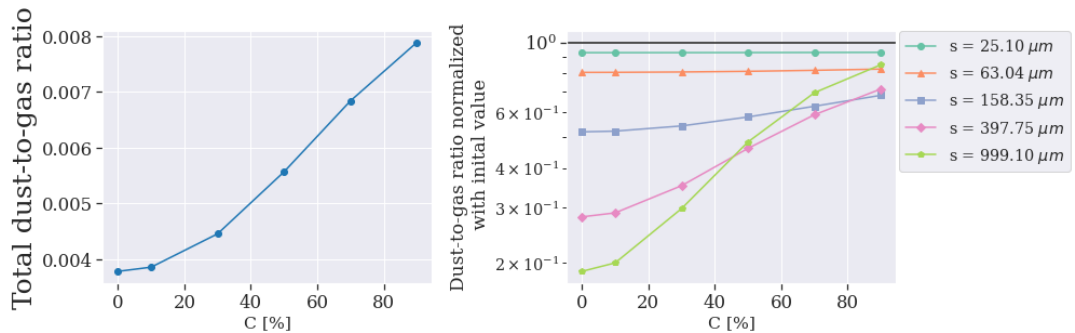
(a) The region below the evaporation line of 0.65 AU for the last snapshot
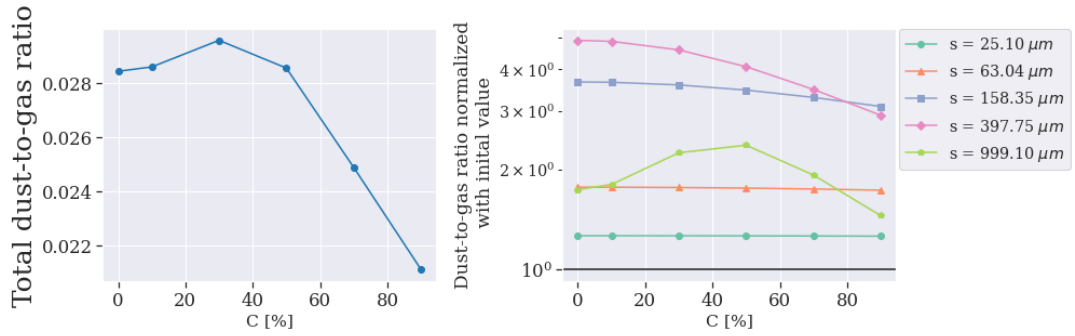
(b) The region between the evaporation line of 0.65 AU to 100*AU* for the last snapshot
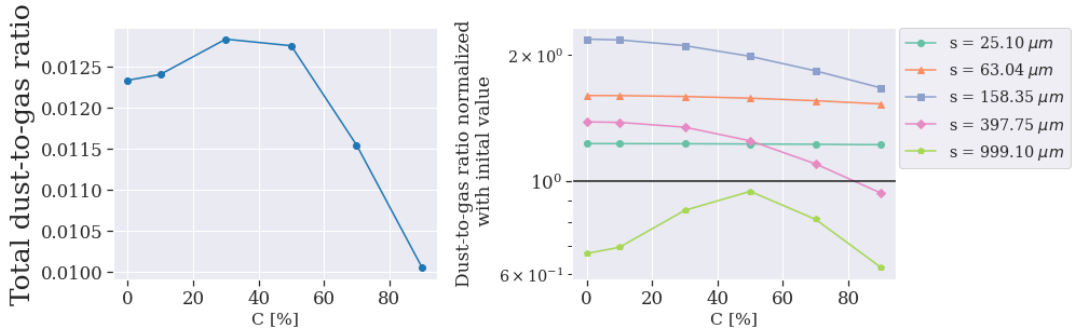
(c) The region between 100 AU and 1000 AU for the last snapshot

(d) The region over 1000 *AU* to end of sphere for the last snapshot

Figure 4.8: Panels **(a)** - **(d)** show the dust content in different regions of the protostellar core for run067 taken at the last snapshot, in which the protostar has been born. The x-axis is the initial keplarian velocity percentage. **(a)** corresponds to the reservoir of material that is used for very early star. **(b)** is the region where the protolanetary disk is formed. **(c)** is the region of corresponding to the early mass reservoir accreted during the embedded Class 0 while **(d)** corresponds the out skirts of the prestellar core, which are low in base and large in volume. Material in this region is only accreted between Class 1 and 2 after ~ 500 kyr, where the star is becoming a main sequence star

Results

As discussed in chapter 4 a background model from [Vaytet and Haugbølle, 2017] is used for the prestellar core. Here multiple initial conditions were chosen of varying size, mass and temperature. They are listed in table 5.1. The dust was initialized with a MRN distribution and a keplarian velocity, given by the equation below, in the azimuthal direction with zero radial velocity.

$$v_{initial} = C \sqrt{\frac{GM(r_p)}{r_p}} \text{ where } C \in [0,1] \tag{5.1}$$

The value of the parameter C changes depending on two configurations used in this work, which are presented in section 5.1 and 6.2. The number of dust particles in both configurations were taken to be 4 of the same size pr radial cell of the prestellar core as in section 4.4. This was done to help smooth the final simulation data. The initial dust-to-gas ratio was initialized for each radial cell to be $\mathscr{D} = 0.01$, resulting in a flat initial dust-to-gas ratio. Only the Epstein regimes was implemented as it breaks for particles over $1mm$ in size near the second Larson core, which is located behind the dust evaporation line, given by a temperature of $1550K$.

The results presented in this chapter is mostly focused on a full presentation of run067, with some cherry picked plots from the other runs which have some unique features. This is done to stop repetition of data and features, as some of the runs are quite similar in features, with the exception of maybe looking a little more super or sub linear, as an example. However all the plots for configuration 1 and configuration 2 are available in Appendix B, together with a coagulation due to Brownian motion for run067.

5.1 Configuration 1: Constant initial Kepler velocity

In this dust configuration the constant C in equation (5.1) is set to a constant for all dust sizes. This varies from 0 to 0.9, so from no azimuthal velocity to 90% of the keplarian velocity. The dust size were defined to be $25\mu m$, $63\mu m$, $158\mu m$, $398\mu m$ and $1mm$ as to have a great variety of stokes numbers and due to recent obeservations ([Pagani et al., 2010]). The various plots in figure 4.8 are segmented into 4 regions of the prestellar disk. The first region, refered to as region 0, is from the center to the evaporation line, $0.67AU$ for run067. This region is where the protostar is formed. The dust-to-gas, from now on refered to as the ratio, for this region is plotted in figure 4.8a.

Here the total ratio is is in the left plot. The lower the azimuthal velocity gives a larger ratio, peaking at 0.22 for 0% keplarian velocity, meaning there is a equivalent of 22% of the gas mass in this region as dust, and at lowest becomes 0.08 for 90%. The left figure is the ratio for the individual grain sizes. Here it is quite clear that the $1mm$ dust is the most abundant grain size within this region, with a ratio ~ 40 times larger than its initial value. As the grain size

Run	R_{BE} [AU]	M_{BE} [$M_\odot$]	T_{BE} [K]	$t_{collapse}$ [kyr]	snapshots [count]	$r_{evap}(t_{collapse})$ [AU]	$\varepsilon = M_{BE}/M_{sphere}$
006	3000	1	10	16	789	0.70	0.28
009	3000	1	25	28	745	0.89	0.71
038	5000	1	10	42	803	0.66	0.47
067	7500	1	10	113	813	0.65	0.71
068	7500	2	5	41	898	0.68	0.18
069	7500	2	10	47	803	0.70	0.35
070	7500	2	15	58	792	0.76	0.53
071	7500	2	20	79	766	0.87	0.71
072	7500	2	25	146	763	0.92	0.89
074	7500	4	10	28	791	0.80	0.18
080	7500	6	10	21	782	0.88	0.12
086	7500	8	10	18	774	0.96	0.09

Table 5.1: Table over the different spheres used from [Vaytet and Haugbølle, 2017]. Here the value of ε is the fraction between the mass of the data sphere compared to the critical BE mass, it should have for the given temperature an radius. If its smaller than 1, then there is less pressure support, and the collapse is very dominated by gravity.

go down we can also see the ratio go down, eg. for $25\mu m$ which only reaches ~ 1.3 times its initial value. Interestingly enough, the $398\mu m$ and $1mm$ dust have almost the same gain for 90%. In this region all dust particles of $158\mu m$ and under have a flat ratio trend, while the larger particles drops off at higher velocities.

The second region, refered to as region 1, is where the protoplanetary disk might be present going from the evaporation line to $100AU$, and is plotted in figure 4.8b. The left plot shows a different structure where the peak is located near 30% with a value of 0.029 and 0% is the third lowest point with a value. The minimum here is still given by 90% with a value of ~ 0.022. The right plot shows that the $1mm$ dust particles is quite low as its abundance is in the range of the $63\mu m$ dust. The abundances in this region is quite lower than the inner most one. Here the maximum abundance is around 5 times the initial values for $398\mu m$. The particles lower than or equal to $158\mu m$ have not changed much, eg. as $158\mu m$ dust have gone from around 4.3 as a maximum to a 3.66. Interestingly only the $1mm$ dust have the higher abundance of dust in the $20-60\%$ range, as the others are still decreasing with increased velocity.

The third region, refered to as region 2, is a potential envelope to the protoplanetary disk located at $100AU$ to $1000AU$ and is shown in figure 4.8c. This region very much follows the same structure as the previously presented region. Here, on the left plot, the maximum is also near the 30% however 50% is close as the ratio is around 0.0128. The minimum is still 90% which has a ratio of 0.01 which is the initial dust-to-gas ratio used for the experiment. The right hand side plot is rather interesting here as the $1mm$ dust is under its initial value with 50% being close to 1. Here the most abundant grain size is $158\mu m$ which hovers around a maximum of 2.17 for 0% and a minimum of 1.67. $398\mu m$ for all velocities dropped below $158\mu m$ and have even for 90% dropped below the initial value. The smallest grains have barely changed from the previous region.

The final region is the rest of the system, ie. everything over 1000 AU which is shown in figure 4.8d. This regions is refered to as region 3. Here the trend in the left plot is reversed as the largest ratio is located at 90% with a value of 0.008 and the smallest located at 0% with a value of 0.004. Both the maximum and minimum is under the initial ratio of 0.01. The right plot is interesting as all dust grains are under their initial value with $1mm$ dust being emptied

the most with an abundance of 0.2 for 0%. The most abundant grain is the $25\mu m$ with an abundance of 0.92 for all velocities. Interestingly dust $1mm$ with 90% is near in abundance to 25 and $63\mu m$.

5.1.1 Outer region of Run069

Figure 5.1 shows region 3 for run069.There is an interesting feature which it also shares with run006. Here the ratio on the right plot increases as the velocity increases like run067. However when the velocity reaches 90%, there is quite a a quite a drop to 0.0093 which is close between the values of 30% and 50%. This is mimicked on the right plot by all grains although at varying degrees. except $25\mu m$. Here the effect is largest for $1mm$ and becomes less and less potent as the grain size decreases.
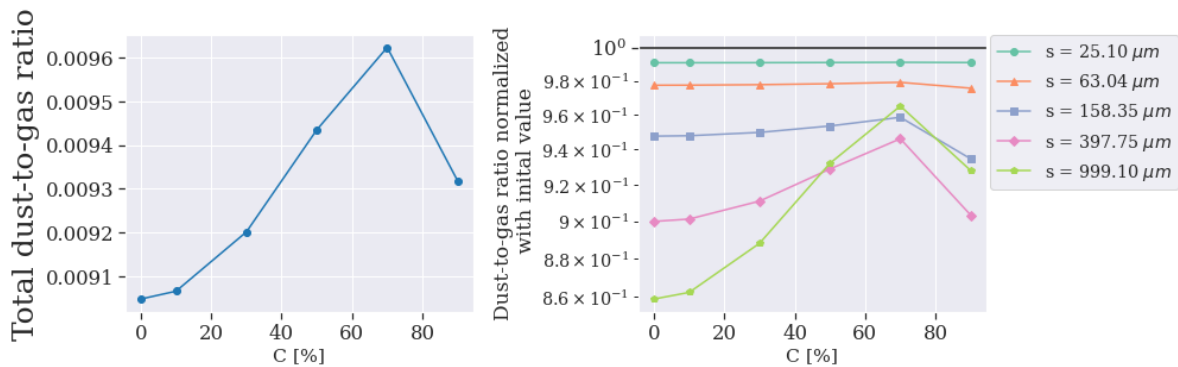
Figure 5.1: The dust-to-gas ratio as a function of the initial keplarian velocity percentage for the outskirts of run069. In this region we have a large volume and low gas mass. The left plot is the total dust-to-gas ratio, while the right plot is the grain specific dust-to-gas ratio. This region is what will eventually be accreted during the transition from Class 1 to Class 2, when the star transitions to a main sequence star.

5.2 Configuration 2: Velocity distribution given by grain size

In this configuration the value of C is determined by the scheme found in 4.6. To recap, a velocity distribution was found where the smallest particle has $C = 2.2\%$ and the largest particle has $C = 100\%$. The critically coupled grain size for a molecular cloud was found to be around $117\mu m$, and for this simulation it was chosen to be $100\mu m$. The value of C for the grains in between are calculated from linear interpolation between the two. The remaining grain sizes are $36\mu m$, $50\mu m$ and $71\mu m$. The same regions defined in section 6.2 are used here. All the regions are shown in figure 5.2a, where the size specific abundances are shown for the last snapshot.

Here one can see that for region 0, the largest particle have the most infall, despite having the larger velocity. The abundances then go down seemingly linearly with grain sizes here after. The $100\mu m$ dust have an abundance of around 2.50 times the initial value, and the smallest grain, $25\mu m$ has a abundance of a bit over 1.25. Regions 1 shows a nearly identical trends, except there is a drop off in abundance for the larger grain sizes, as $100\mu m$ is not around 2.25, while $25\mu m$ is nearly identical. In region 2, we see a different trends as $71\mu m$ and $100\mu m$ are nearly identical in abundance, hovering around 1.60. The almost linear trends continues for grain sizes under $71\mu m$ and we again see a very little difference for the $25\mu m$ dust. Region 3 is different from the others as all grain sizes have abundances lower than their
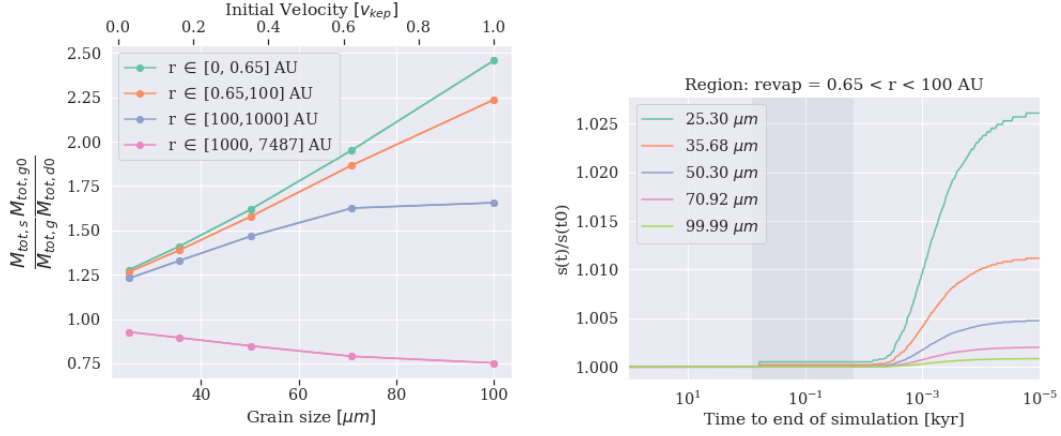
(a) Dust-to-gas ratio for a velocity distribution

(b) Example of Brownian motion

Figure 5.2: **a)** The dust-to-gas ratio for run067 with a velocity distribution based on grain size. Here the maximum size is $100\mu m$. The 4 defined regions are represented by their own lines. **b)** The coagulation due to brownian motion for configuration 2, in region 0. The growth due to Brownian motion is next to zero for the entirety of the collapse for the given grain sizes

initial values. Further more here the $100\mu m$ dust has the lowest abundance, which hovers around 0.75, with $71\mu m$ close by hovering a bit lower 0.75
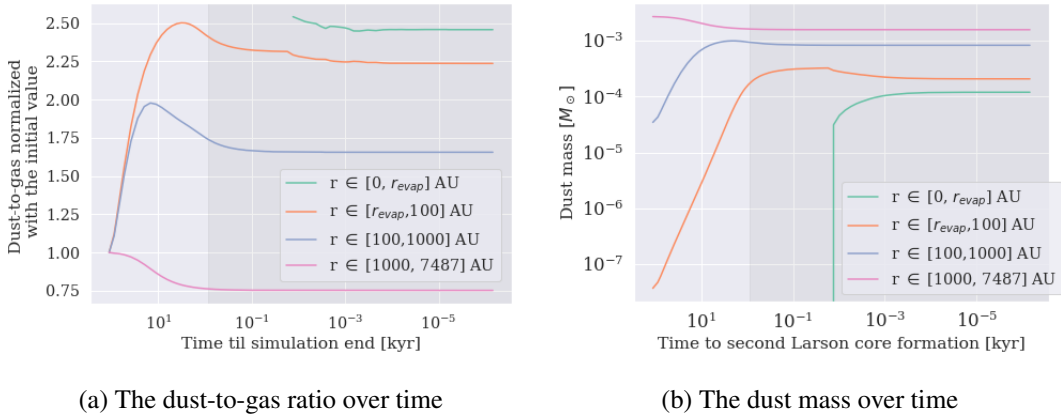
(a) The dust-to-gas ratio over time

(b) The dust mass over time

Figure 5.3: The shaped area in both plots shows the formation of the first Larson core. **(a)** The-dust-to-gas ratio various regions in the prestellar core as a function of time till the formation of the second Larson core. The first being for the region that will become the reservoir for the protostar which goes from the 0 to r_{evap}. The second region going from r_{evap} to 100 AU is the region where the protoplaneary disk is formed, and is this important for planet formation. The third region is what will accrete unto the embedded Class 0 star. This region goes from 100 AU to 1000 AU. The last region is that of the our edge of the core which will accrete unto the star doing the its transition to the main sqeuence. **(b)** shows the same as **(a)** but with the dust mass instead of the dust to gas ratio.

5.2.1 Dust-to-gas ratio as a function of time

Figure 5.3a shows the ratio for $100\mu m$ as a function of time for the various regions, while 5.3b show the same but for dust mass. However the regions defined by the evaporation line, also changes with time, starting at 0 when there is no line, to $0.65 AU$ for the last snapshot. The shaded area outlines the a rough beginning of the first adiabatic phase of the first Larson

core for run067 and starts around when there is 1kyr left. Figure 5.3a shows the ratio in the region 3 decreases over time, while the others increase. Further more it seems that the ratio for region 1 and 2 seems to drop off after or near the adiabatic phase. Further more one can see that region under the evaporation line comes into being when there is roughly 0.01kyr left. Further more the ratio seems to become constant a short time after the adiabatic process begins. These features are mimiced by the dust mass shown in figure 5.3b. Although here its a bit more apparent that when we introduce a new region. Here we there is only a drop in mass for region 2 and 3.

(a) Region 0

(b) Region 1
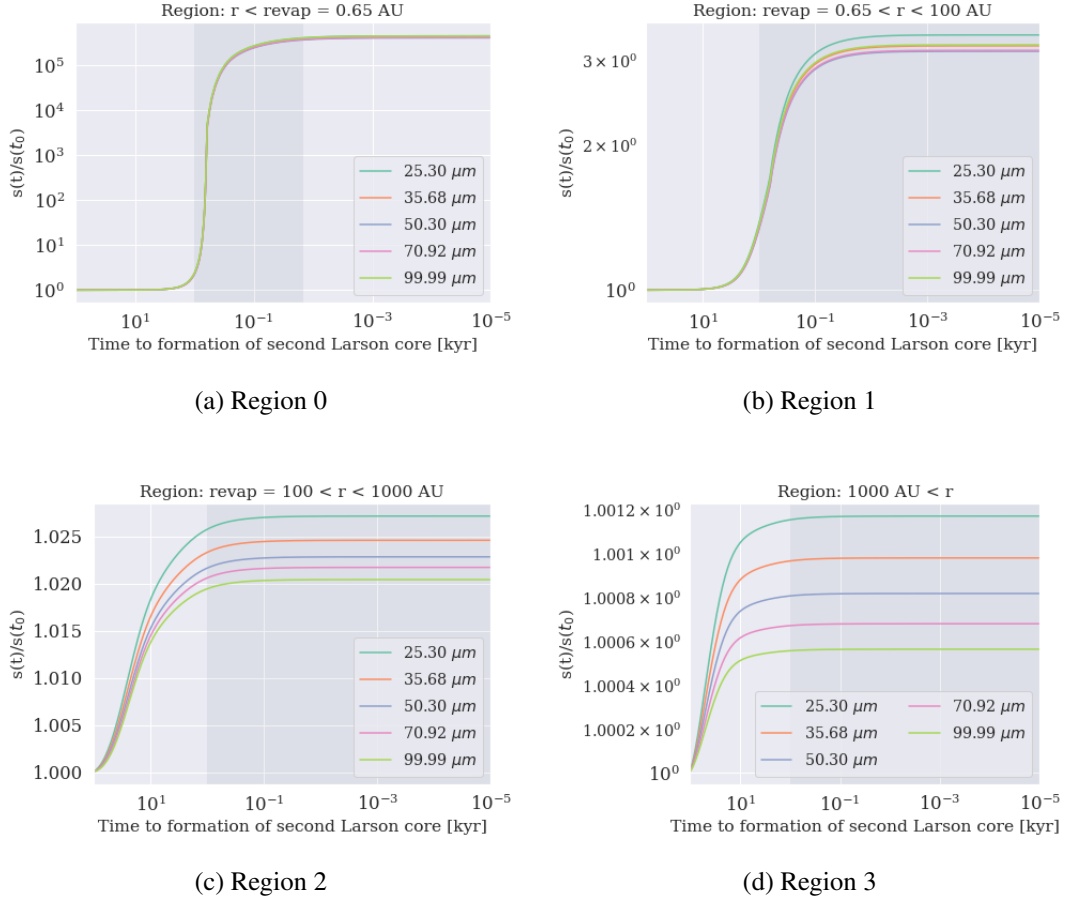
(c) Region 2

(d) Region 3

Figure 5.4: Panels (a) - (d) shows the the growth of various grain sizes due to radial coagulation for 4 different regions. The start of the shaded area indicates the formation of the first Larson core, and its end (if any) dictates when the temperature increases past the evaporation line given by a temperature of 1550 K. (a) corresponds to the reservoir that will accrete unto the very early star. (b) corresponds the to region in which the protoplanetary disk would be formed in the case of prestellar core rotation. (c) is the region that will accrete unto the embedded Class 0 star while (d) is the outskirts of the prestellar core where the mass is low, and the volume is large. These will accrete unto the star doing its transition to becoming a main sequence star

5.2.2 Coagulation estimation

Coagulation can be estimated from the schemes found in section 3.5.3 for similar sized particles. Here schemes for Brownian, radial and turbulent motions where found. However only Brownian and radial will be presented. This is because of an uncertainty that the turbulence scheme was done entirely correctly both in implementation and derivation, and due to time constrains it was opted from a proper analysis. Figure 5.4a shows the estimated growth due to

coagulation for the various dust sizes from configuration 2, in region 0. The start of the shaded area, indicates the formation of for the first Larson core, and if it ends then the temperature is over the 1550K goes over the evaporation line. In this figure its quite clear that the coagulation due to radial effects come into effect after the creation of the first Larson core. The numbers here are to a gain of 10^5 might be bloated due to the region approach described in section 3.5.3.

The growth due to coagulation is also present in the region 1 to a lesser extend as the gain is around 3 seen in figure 5.4b. For the region between region 2 and region 3, there is little to no gain as the highest is for region 2 is roughly 1.025 times the original size. Also in these regions it seems to start growing from the start of the simulation. For Brownian motion there isn't any change any where in the sphere, as we can see an example of in figure 5.2b

5.3 Dust-to-gas ratio as a function of sphere parameters

Figure 5.5 shows the dust-to-gas ratio over the prestellar cores physical properties of mass, initial temperature and initial core radius for configuration 2. Here the core only 1 property varies pr plot, so if the mass changes then the temperature and radius is the same.

Figure 5.5a shows normalized ratio for varying mass is shown for region 0. Here there is a clear trend that the lower mass cores result in the most gain, however it seemingly converge around $4M_\odot$ and flatten quite out to a ratio around 1. Figure 5.5b shows the ratio in region 3. Here a mass of around $1M_\odot$ seems to give a large drop in the ratio while the rest of the masses seemingly have a close to flat/linear trend with little to no variation. The other regions are presented here as they have little to no change in terms of form from the inner most region.

Figure 5.5c shows how the dust-to-gas ratio in region 0 changes with changes size of the prestellar core. There is a increase in the ratio as the pretellar core radius increases. Figure 5.5d shows the same but for region 3. Here its the same as for the mass, where the smaller radius has the most ratio, while the larger ones have decreased quite a bit. Again the regions between the inner and out most regions are the same structure as the inner most.

Figure 5.5e shows region 0 with varying temperature. Here we see a steady increase as temperatures increase, and then a more drastic increase going from $20K$ to $25K$. Figure 5.5f shows region 3 with varying temperatures. Here we see a trend similar to mass and radius, where the smallest value, have the largest increase. However this is not the case for $100\mu m$, which seems to is lower for $5K$ that for $10K$.

(a) Dust-to-gas over core mass

(b) Dust-to-gas over core mass

(c) Dust-to-gas over initial core radius

(d) Dust-to-gas over initial core radius

(e) Dust-to-gas over initial core temperature
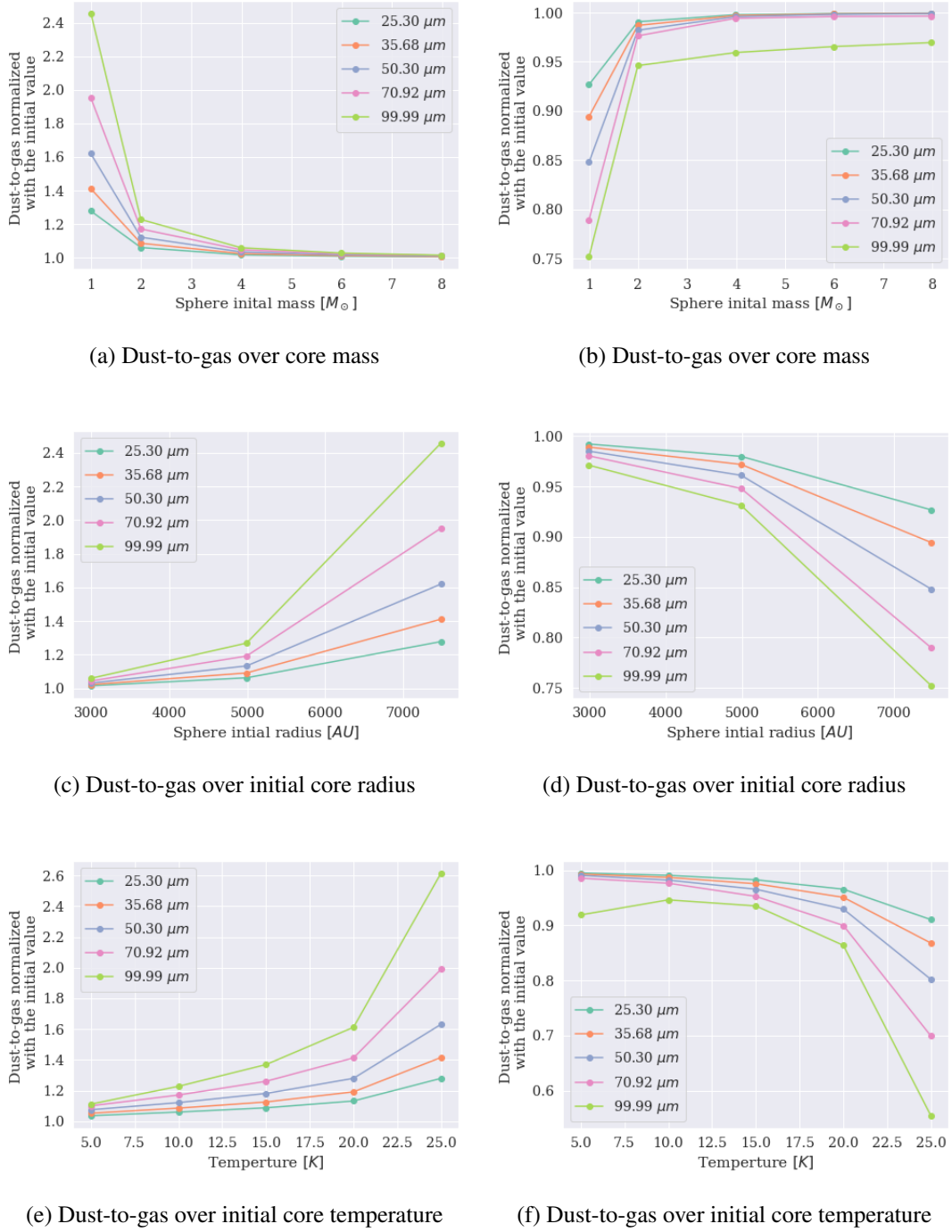
(f) Dust-to-gas over initial core temperature

Figure 5.5: Panels **(a)**, **(c)** and **(e)** shows the dust to gas ratio as a function of varying core parameters for various grain sizes. These are all in the region from the center to the evaporation line (1550 K) for their last snapshot. This region will accrete unto the star doing the embedded class 0 phase. **(b)**, **(d)** and **(f)** shows the same but for the outskirts of the prestellar core going from 1000 AU to the end of the sphere. This region is what will accrete unto the star as it begins its transition into the main sequence. **(a)** is the dust-to-gas ratio as a function of the initial core mass for the inner region while **(b)** shows the same but for the outskirts. **(c)** shows the dust-to-gas ratio for the inner region as a function of initial core radius, while **d** shows the same but for the outskirts of the sphere. **(e)** shows the ratio for the inner region for varying initial core temperatures while **(f)** shows the same but for the outskirts of the sphere.

Discussion

During the preceding chapters the theory, numerical framework, the background fluid models have been presented. Furthermore in chapter 5 the results for how dust settles in a prestellar core both with varying initial velocities, as a function of time and as a function of prestellar core properties. I will now process with discussing and interpret my results.

6.1 Configuration 1

When looking at figure 4.8 one can clearly see that the lower the azimuthal velocity the larger increase in dust-to-gas ratio is. This is expected, since the friction force first has to deplete the azimuthal velocity before the dust grains can settle into the center. Furthermore the particles need to not couple hard to the gas. This is likely the reason why the $1mm$ dust is the most effective at settling in the grain set, as its stokes numbers in the center is around 1.8 and in the the outer most radial cell is around 3. The particles smaller than this are more coupled to the dust which naturally limits their settling as they adapt faster to the gas.

If the velocity of the dust is high enough while being decoupled from the gas, we can risk the loss of mass, as the core collapses to quickly. This is what we observe in figure 5.1 with the bend around 70% to 90% where $1mm$ dust has a stokes number around 0.5. If we correct extend region 3 to be everything outside and not just yup to end of the sphere we get figure 6.1, which like 4.8d with no bend. However the stokes number is for $1mm$ dust in run069 is lower than in run run067 where we don't see the bend. The reason for this is likely the difference in pressure support, as run067 has a higher ε value.
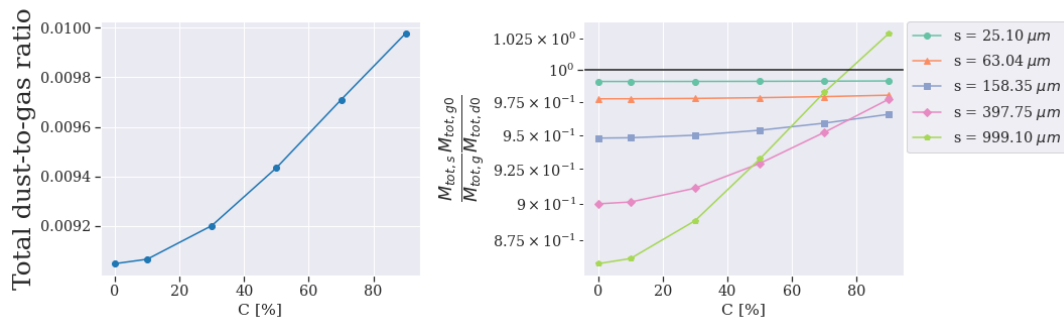
Figure 6.1: Both plots are for outskirts and outside the core of run069 going from 1000 . This region is what will eventually accrete unto the star as it enters the main sequence. The left plot is the total dust-to-gas ratio as a function of the initial keplarian velocity percentage, ie. the constant C in equation (5.1). While the right plot shows the same but for the specific grain sizes, where the dust-to-gas ratio as been normalized with its initial value. This figure is companion plot to figure 5.1, as we here have accounted for the mass lost doing the collapse.

The ratio in figure 4.8a is quite large, as 0% has a value of 0.22. This implies that the metalicity of the protostar is equally high, as an equal of 22% of the gas mass lies in "metals", eg. graphite compared to the solar metallicty of 0.0134. This high metalicity would have some heavy effects on the opacity of the star, which can have some unforeseen consequences. Naturally we have rather large particles in high bulk in this simulation, but recent observations indicate that they might not be unrealistic ([Pagani et al., 2010]). These large metalicity are also present for the other velocities as the lowest for this region is 0.08 which around 8 times larger than the solar metalicity.

Another aspect of figure 4.8 is that we can see that small dust grain do not settle efficiently to the center of the prestellar core, and their partial dust-to-gas ratio is therefore not enhanced. For $25\mu m$ have roughly the same gain of material in all regions except region 3. This implies that if have particles near the *nm* then we would likely have no gain at all in the system

The region 1 for run067 which can contain a protoplanetary disk shows an increase of gain, although not as high as the star region. However it is still a total gain of roughly 2-3 times the initial. This shows that the disk might have a dist to gas ratio that is higher than the canonical value of 0.01, given the particles are larger or near $25\mu m$. Further more if we want to maximize the dust to gas ratio for the disk, we need to have a velocity in the 50% range. This might also have some implications for a rotating core, as the dust would then be dragged along the rotational axis, which would reduce the transformation of the azimuthal velocities into radial velocities.

6.2 Configuration 2

Configuration 2 shows what one would expect from the plots in section 5.1, as eg. figure 5.4a is essentially just sampled sampled data for a grain size as a velocity in figure 4.8a. However the coagulation results are quite interesting for here one can clearly see eg. in figure 5.4a, that comes into effect after the formation. This seems to happens because as the dust density also increases, likely do to particles are more coupled in the center of the core than further out, and as such when the core is formed, movement of dust is is slowed within the core while it side the core, particles still move less coupled, and thus the dust accumulates more. Brownian motion is not shown to be of much concern for the particles used in the simulation. This however is likely a boundary from the sizes for if the particles where smaller eg. in *nm* size, then Brownian motion would likely be have a bigger effect. The plots in figure 5.3 are quite interesting,
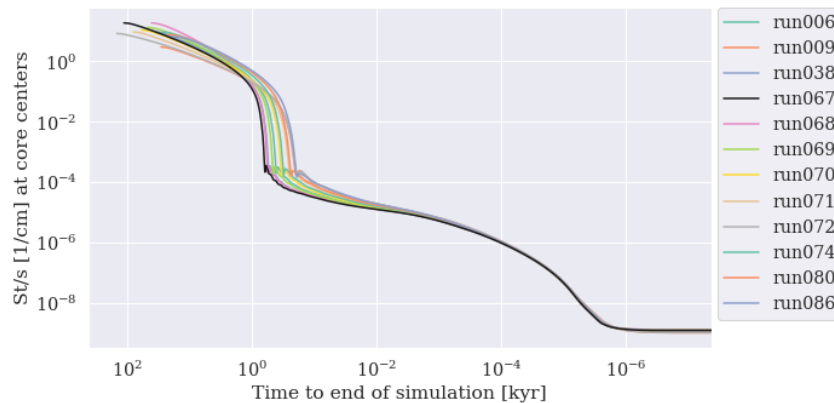

Figure 6.2: Figure here illustrates the size reduced stokes number for the center of the core as a function of time till the creation of the second Larson core. The drop around 1 kyr indicates the formation of the fist Larson core.

as it is quite clear that that when the core begins its first adiabatic phase, the particles will stop their movement as they couple strongly to the gas. This coupling seems to happen because the density and temperature in the first Larson cores increases by several magnitudes, which the Epstein regime is inversely proportional to the square root of the these parameters. This is exemplified in figure 6.2, which shows the size reduced stokes number at the center cell of all cores. Here there is the drop comes from the increase doing the adiabatic phase. What this means is that after the initial drop, we need a grain size of roughly 10^4cm for the stokes number order of unity. This means that all grain sizes, even the $1mm$ from configuration 1 couples at this point. In figure 5.3a the drop in ratio right before the adiabatic phase for the evaporation region and the up to 100 AU region. For region 2, its seems to be because of a lesser infall of material from outer regions as region 3 empties out. However the decrease in for region 1, is rather curious, for the drop here implies either that the gas mass is increasing after this point in time, or dust mass is lost. The latter doesn't seems to be the case there is no drop at this point in the mass for figure 5.3b, and when looking at the mass change over time for the dust and gas, the dust seems to gain more for a period, and then the gas takes over. The reason for this could be a numerical remedy, since the particles are not run in concurrently.

An interesting consequence of the dust coupling of the adiabatic phase, is that the coagulation of dust begins as discussed, at this time. This means that small dust particles, trades their radial dynamics for coagulation and the two doesn't exist at the same time (Although for $1mm$ dust it begins before hand as seen in appendix figure B.14. However this coagulation might not give rise to any additional radial settling as we need to create quite large particles to settle as shown in figure 6.2.

6.3 Varying core parameters

In section 6.2 we discussed that dust grain couple tightly to the gas when the core begins its first adiabatic phase which happens roughly at 1kyr before the formation of the second Larson core. As each core as a different collapse time as seen in table 5.1 there is a bias in dust settling for cores with a long collapse time. This is exemplified by figure 5.5e which shows an increase in the ratio for larger temperatures, which essentially means more settling for more coupled dust. However the largest temperature also has the longest collapse time as it has more pressure support, so this seems to indicate that the collapse time is at least more important than the coupling. However this might only be if the particles are coupled enough, for in figure 5.5f which is for the region 3, the lowest temperature of $5K$ for $100\mu m$ has the lowest ratio. This seems to indicate there might be coupling point where the collapse time becomes less important. If we look at the stokes number as a function of temperature for these regions as shown in figure 6.3b, we can see that $100\mu m$ has a stokes number of 0.7 in the out most radial cell, while other particles that are showing a more collapse orientated trend have at most a stokes number for $5K$ of 0.5. With this it seems that if the stokes number is higher than 0.7 the collapse time becomes a little less important. Sadly this indication can not be seen in with the core mass and radius in figure 6.3a and 6.3b, for here the larger mass has the smallest collapse time and the smallest stokes number and for the radius the largest core has the largest collapse time and the largest stokes number. This is shown in figure 6.3c and figure 6.3d
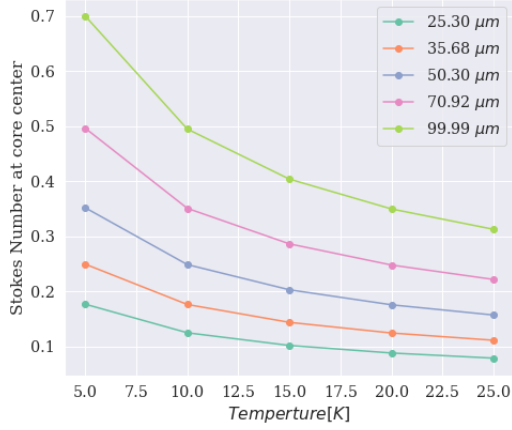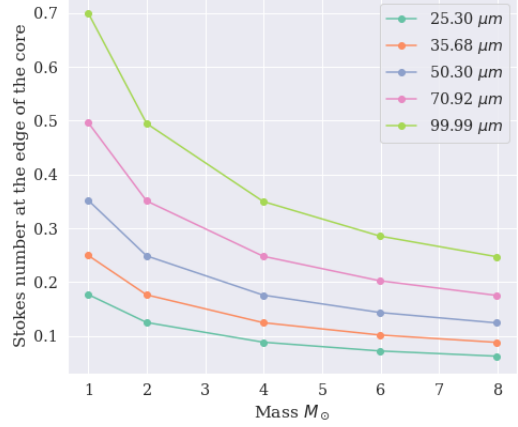
(a) For the centre of the core
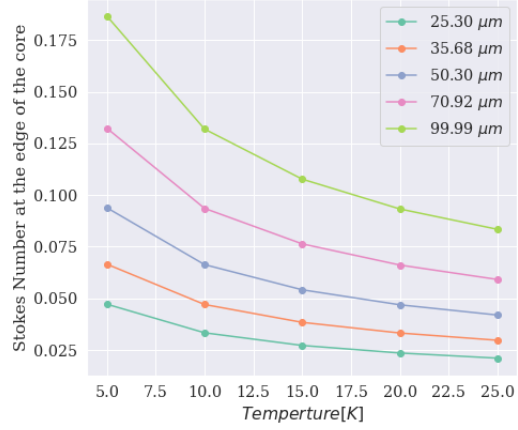
(b) For the edge of the core
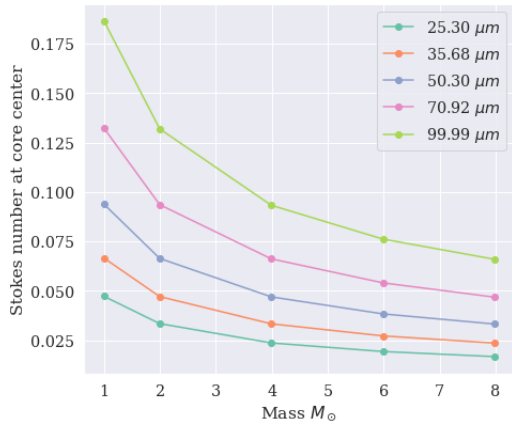
(c) For the centre of the core

(d) for the edge of the core

Figure 6.3: Panel **(a)** and **c** are for the center of the cores while panel **(b)** and **(c)** are for the edge of the cores. **(a)** shows the stokes number as a function of initial core temperatures, while **(b)** shows the same but for the edge of the core, which results in the change of stokes number. **(c)** shows the stokes number for the center as a function of initial core mass while **(b)** shows the same but for the edge of the sphere.

Conclusion and outlook

In this work we set out to understand how dust settles in a prestellar core, in order to find or test new initial conditions for the protoplanetary disk. For this we developed a postprocessing framework in python that allow macro particles to be evolved through prestellar core simulation data sets, which can help computation time as complex core simulations can take quite a long time to compute. The underlying prestellar core simulations are from [Vaytet and Haugbølle, 2017].

Here it was found that the inital azimuthal velocity of dust particles plays quite a big role, as the lower azimuthal velocity present the more effective settling, as less velocity needs to be transformed into radial velocity. However this is only if the core collapses radially. Interestingly here if the particles are decoupled enough, the higher velocities, around 50% of the initial keplarian velocity, will result in a higher dust-to-gas ratio for the region where a protoplanetray disk is formed. Here a dust-to-gas ratio for the disk would be larger than the canonical value of 0.01, for at least particles around the $25\mu m$ range. This naturally is under the assumption that the core starts with the Canonical ratio 0.01. However, the most interesting and surprising thing is that the dust-to-gas ratio for coupled particles with a stokes number around unity, is really large in the region where the protostar is formed. This means that the metalicity of the star will be quite large, to the point that it would be hard to imagine how such a star would look.

The settling of dust was found to be limited in terms of time, as all particles except for sizes larger than a few meters, couple hard to the gas when the first Larson core enters its adiabatic phases. This is naturally only a prospect for particles inside the first Larson core, however, dust further out seems to empty out rather quickly as the dust effectively settles in this region. Interestingly for particles smaller than $1mm$, there is a switch of dynamics as this point in time, since when the particles couple, coagulation seems to kick in allowing for a potentially significant growth in dust, although the estimations are rough, and were done to have an idea of where it might be effective.

The beginning of the adiabatic process of the prestellar core happens for all cores nearly at the time relative to their second core formation. Here all cores start the process roughly around $0.5kyr$ from the second core formation, meaning it is independent of collapse time. Consequently there is more settling of dust if the core as a long collapse time. However, if the particles are not heavily coupled to the data, eg. with a stokes number of 0.7, then there can be quite a lot more effective settling.

The results of this thesis shows that the that the dynamics of dust in a prestellar core are quite important for not only the protoplanetary disk but also for the star itself though high metalicities.

7.0.1 Future work

In this thesis the focus was mostly the the radial infall of dust in a 1D radiative prestellar core. However there is still plenty needed to be done to fully understand the settling of dust in a prestellar core. The first and most obvious would be to run the current setups including a framwork for dust grain size evolution, e.g. coagulation and fragmentation. For while it seems to become important for large grain in the late stages of the first Larson core, it can potentially still give a increase in certain dust sizes. Luckily fellow master student Martin Jan Sandberg, have as a part of his thesis developed such a module. Here it could also be interesting to do simulations with particles smaller than $25\mu m$ to identify when the dust-to-gas ratio stays constant over the collapse. Furthermore one can then look into when Brownian motion becomes important and if it can give a lower barrier for dust present in the disk.

Other interesting work include the study of capturing dust particles from filament flows. This could give rise to more dust in the prestellar core at various regions, and thus might help kick start coagulation, or maybe dust of the correct sizes can settle efficiently into the center of the core.

Pebble accretion could also be studied to see if it plays a role in growth doing the early stages of star formation or if it just present in the protoplanetary disk. If it is present it could lead to even more growth of dust sizes, and can thus give a better understanding of the dust sizes present in the protoplanetary disk.

Once these aspects have been understood, we can move onto larger spatial dimensions, where we can include the effect of magnetism and rotation as they can likely affects the infall of dust quite significantly. This can likely be achieved with the DISPATCH library for FORTRAN, although the process might need to be separated due to computational cost.

In this thesis we assumed a initial dust-to-gas ratio of the canonical value of 0.01. This however might not be correct as the initial dust-to-gas ratio for the prestellar core is dictated by the dust dynamics in the prestellar core. So to obtain more physically correct representation of both the core and the disk we also need to understand the dynamics in the molecular clouds.

Bibliography

J. F. Alves, C. J. Lada, and E. A. Lada. Internal structure of a cold dark molecular cloud inferred from the extinction of background starlight. *Nature*, 409(6817):159–161, Jan. 2001.

P. J. Armitage. Lecture notes on the formation and early evolution of planetary systems. *arXiv e-prints*, art. astro-ph/0701485, Jan. 2007.

D. Arzoumanian, P. André, P. Didelon, V. Könyves, N. Schneider, A. Men'shchikov, T. Sousbie, A. Zavagno, S. Bontemps, J. di Francesco, M. Griffin, M. Hennemann, T. Hill, J. Kirk, P. Martin, V. Minier, S. Molinari, F. Motte, N. Peretto, S. Pezzuto, L. Spinoglio, D. Ward-Thompson, G. White, and C. D. Wilson. Characterizing interstellar filaments with Herschel in IC 5146. *A&A*, 529:L6, May 2011. doi: 10.1051/0004-6361/201116596.

E. A. Bergin and M. Tafalla. Cold dark clouds: The initial conditions for star formation. *Annual Review of Astronomy and Astrophysics*, 45(1):339–396, Sep 2007. ISSN 1545-4282. doi: 10.1146/annurev.astro.45. 071206.100404. URL http://dx.doi.org/10.1146/annurev.astro.45.071206.100404.

T. Birnstiel, C. P. Dullemond, and F. Brauer. Gas- and dust evolution in protoplanetary disks. *A&A*, 513:A79, Apr. 2010. doi: 10.1051/0004-6361/200913731.

Birnstiel, T., Dullemond, C. P., and Brauer, F. Gas- and dust evolution in protoplanetary disks. *A&A*, 513:A79, 2010. doi: 10.1051/0004-6361/200913731. URL https://doi.org/10.1051/0004-6361/200913731.

W. B. Bonnor. Boyle's Law and gravitational instability. *MNRAS*, 116:351, Jan. 1956. doi: 10.1093/mnras/116.3. 351.

F. Brauer, C. P. Dullemond, and T. Henning. Coagulation, fragmentation and radial motion of solid particles in protoplanetary disks. *Astronomy & Astrophysics*, 480(3):859–877, Nov 2007. ISSN 1432-0746. doi: 10.1051/ 0004-6361:20077759. URL http://dx.doi.org/10.1051/0004-6361:20077759.

M. G. Brouwers, A. Vazan, and C. W. Ormel. How cores grow by pebble accretion. *Astronomy & Astrophysics*, 611:A65, Mar 2018. ISSN 1432-0746. doi: 10.1051/0004-6361/201731824. URL http://dx.doi.org/10.1051/ 0004-6361/201731824.

A. Burkert and L. Hartmann. Collapse and fragmentation in finite sheets. *The Astrophysical Journal*, 616(1): 288–300, Nov 2004. ISSN 1538-4357. doi: 10.1086/424895. URL http://dx.doi.org/10.1086/424895.

M. Elimelech, J. Gregory, X. Jia, and R. Williams. Chapter 6 - modelling of aggregation processes. In M. Elimelech, J. Gregory, X. Jia, and R. Williams, editors, *Particle Deposition & Aggregation*, pages 157–202. Butterworth-Heinemann, Woburn, 1995. ISBN 978-0-7506-7024-1. doi: https://doi.org/10.1016/B978-075067024-1/50006-6. URL https://www.sciencedirect.com/science/article/pii/ B9780750670241500066.

Geretshauser, R. J., Meru, F., Speith, R., and Kley, W. The four-population model: a new classification scheme for pre-planetesimal collisions. *A&A*, 531:A166, 2011. doi: 10.1051/0004-6361/201116901. URL https: //doi.org/10.1051/0004-6361/201116901.

L. Hartmann. *Initial conditions for protostellar collapse*, page 43–59. Cambridge Astrophysics. Cambridge University Press, 2 edition, 2008a. doi: 10.1017/CBO9780511552090.005.

L. Hartmann. *Protostellar cloud collapse*, page 60–81. Cambridge Astrophysics. Cambridge University Press, 2 edition, 2008b. doi: 10.1017/CBO9780511552090.006.

M. Heath. *Scientific Computing: An Introductory Survey*. McGraw-Hill Education, 2005. ISBN 9780071244893. URL http://books.google.de/books?id=gwBrMAEACAAJ.

H. Kirk, P. C. Myers, T. L. Bourke, R. A. Gutermuth, A. Hedden, and G. W. Wilson. Filamentary accretion flows in the embedded serpens south protocluster. *The Astrophysical Journal*, 766(2):115, Mar 2013. ISSN 1538-4357. doi: 10.1088/0004-637x/766/2/115. URL http://dx.doi.org/10.1088/0004-637X/766/2/115.

M. Kuffmeier, T. Haugbølle, and Å. Nordlund. Zoom-in Simulations of Protoplanetary Disks Starting from GMC Scales. *ApJ*, 846(1):7, Sept. 2017. doi: 10.3847/1538-4357/aa7c64.

J. S. Mathis, W. Rumpl, and K. H. Nordsieck. The size distribution of interstellar grains. *ApJ*, 217:425–433, Oct. 1977. doi: 10.1086/155591.

F. Nakamura and Z.-Y. Li. Magnetically Regulated Star Formation in Three Dimensions: The Case of the Taurus Molecular Cloud Complex. *ApJ*, 687(1):354–375, Nov. 2008. doi: 10.1086/591641.

C. W. Ormel, A. Vazan, and M. G. Brouwers. How planets grow by pebble accretion. *Astronomy & Astrophysics*, 647:A175, Mar 2021. ISSN 1432-0746. doi: 10.1051/0004-6361/202039706. URL http://dx.doi.org/10.1051/0004-6361/202039706.

P. Padoan, M. Juvela, A. A. Goodman, and Å. Nordlund. The Turbulent Shock Origin of Proto-Stellar Cores. *ApJ*, 553(1):227–234, May 2001. doi: 10.1086/320636.

L. Pagani, J. Steinacker, A. Bacmann, A. Stutz, and T. Henning. The Ubiquity of Micrometer-Sized Dust Grains in the Dense Interstellar Medium. *Science*, 329(5999):1622, Sept. 2010. doi: 10.1126/science.1193211.

P. Palmeirim, P. André, J. Kirk, D. Ward-Thompson, D. Arzoumanian, V. Könyves, P. Didelon, N. Schneider, M. Benedettini, S. Bontemps, J. Di Francesco, D. Elia, M. Griffin, M. Hennemann, T. Hill, P. G. Martin, A. Men'shchikov, S. Molinari, F. Motte, Q. Nguyen Luong, D. Nutter, N. Peretto, S. Pezzuto, A. Roy, K. L. J. Rygl, L. Spinoglio, and G. L. White. Herschel view of the Taurus B211/3 filament and striations: evidence of filamentary growth? *A&A*, 550:A38, Feb. 2013. doi: 10.1051/0004-6361/201220500.

N. Peretto, P. André, V. Könyves, N. Schneider, D. Arzoumanian, P. Palmeirim, P. Didelon, M. Attard, J. P. Bernard, J. Di Francesco, D. Elia, M. Hennemann, T. Hill, J. Kirk, A. Men'shchikov, F. Motte, Q. Nguyen Luong, H. Roussel, T. Sousbie, L. Testi, D. Ward-Thompson, G. J. White, and A. Zavagno. The Pipe Nebula as seen with Herschel: formation of filamentary structures by large-scale compression? *A&A*, 541:A63, May 2012. doi: 10.1051/0004-6361/201118663.

T. Quinn, N. Katz, J. Stadel, and G. Lake. Time stepping N-body simulations. *arXiv e-prints*, art. astro-ph/9710043, Oct. 1997.

W. M. Ruyten. Density-Conserving Shape Factors for Particle Simulations in Cylindrical and Spherical Coordinates. *Journal of Computational Physics*, 105(2):224–232, Apr. 1993. doi: 10.1006/jcph.1993.1070.

N. S. Schulz. *Historical Background*, pages 7–31. Springer Berlin Heidelberg, Berlin, Heidelberg, 2012. ISBN 978-3-642-23926-7. doi: 10.1007/978-3-642-23926-7_2. URL https://doi.org/10.1007/978-3-642-23926-7_2.

V. Springel. The cosmological simulation code GADGET-2. *MNRAS*, 364(4):1105–1134, Dec. 2005. doi: 10.1111/j.1365-2966.2005.09655.x.

S. Stahler and F. Palla. *The Collapse of Dense Cores*, chapter 10, pages 282–316. John Wiley & Sons, Ltd, 2004a. ISBN 9783527618675. doi: https://doi.org/10.1002/9783527618675.ch10. URL https://onlinelibrary.wiley.com/doi/abs/10.1002/9783527618675.ch10.

S. Stahler and F. Palla. *The Collapse of Dense Cores*, chapter 10, pages 282–316. John Wiley & Sons, Ltd, 2004b. ISBN 9783527618675. doi: https://doi.org/10.1002/9783527618675.ch10. URL https://onlinelibrary.wiley.com/doi/abs/10.1002/9783527618675.ch10.

S. Stahler and F. Palla. *Molecular Clouds*, chapter 3, pages 60–87. John Wiley & Sons, Ltd, 2004c. ISBN 9783527618675. doi: https://doi.org/10.1002/9783527618675.ch3. URL https://onlinelibrary.wiley.com/doi/abs/10.1002/9783527618675.ch3.

A. G. G. M. Tielens and W. Hagen. Model calculations of the molecular composition of interstellar grain mantles. *A&A*, 114(2):245–260, Oct. 1982.

E. F. van Dishoeck. Molecular Cloud Chemistry. In R. D. Wolstencroft and W. B. Burton, editors, *Millimetre and Submillimetre Astronomy*, volume 147, page 117, Jan. 1988. doi: 10.1007/978-94-009-3019-3_4.

N. Vaytet and T. Haugbølle. A grid of one-dimensional low-mass star formation collapse models. *A&A*, 598:A116, Feb. 2017. doi: 10.1051/0004-6361/201628194.

D. Ward-Thompson, P. F. Scott, R. E. Hills, and P. Andre. A Submillimetre Continuum Survey of Pre Protostellar Cores. *MNRAS*, 268:276, May 1994. doi: 10.1093/mnras/268.1.276.

S. J. Weidenschilling. Aerodynamics of solid bodies in the solar nebula. *MNRAS*, 180:57–70, July 1977. doi: 10.1093/mnras/180.2.57.

Windmark, F., Birnstiel, T., Güttler, C., Blum, J., Dullemond, C. P., and Henning, Th. Planetesimal formation by sweep-up: how the bouncing barrier can be beneficial to growth. *A&A*, 540:A73, 2012. doi: 10.1051/0004-6361/201118475. URL https://doi.org/10.1051/0004-6361/201118475.

Derivation of coagulation rate

Brownian Motion

The decomposition for Brownian motion is obtained from equation (3.39).

$$C = \sqrt{\frac{12k_b}{\pi^2 \rho_s}} \wedge \xi = s^{-3/2} \wedge Y = \sqrt{T} \tag{A.1}$$

When inserting this into equation (3.51), one obtains the following.

$$\int_{s_0}^{s} s^{3/2} ds = \sqrt{\frac{12k_b}{\pi^2 \rho_s^3}} \sum_{i=1}^{N} \left(A_\rho \int_{t_{i-1}}^{t_i} t \sqrt{A_T\, t + B_T}\, dt + B_\rho \int_{t_{i-1}}^{t_i} \sqrt{A_T\, t + B_T}\, dt \right) \tag{A.2}$$

The integral on the LHS is trivially easy to solve.

$$\int_{s_0}^{s} s^{3/2} ds = \frac{2}{5} \left(s^{5/2} + s_0^{5/2} \right) \tag{A.3}$$

Both integrals on the RHS can be solve by using the same substitution. For the substitution the following variables are defined:

$$u = A_T\, t + B_T \Rightarrow dt = \frac{du}{A_T} \wedge t = \frac{u - B_T}{A_T} \tag{A.4}$$

Interesting this into $\int_{t_{i-1}}^{t_i} t \sqrt{A_T\, t + B_T}\, dt$ yields the following:

$$
\begin{aligned}
\int_{t_{i-1}}^{t_i} t \sqrt{A_T\, t + B_T}\, dt &= \frac{1}{A_T^2} \int_{t_{i-1}}^{t_i} u^{3/2} du - \frac{B_T}{A_T^2} \int_{t_{i-1}}^{t_i} u^{1/2} du \\
&= \frac{2}{5A_T^2} \left[u^{5/2} \right]_{t_{i-1}}^{t_i} - \frac{2B_T}{3A_T^2} \left[u^{3/2} \right]_{t_{i-1}}^{t_i} \\
&= \frac{2}{5A_T^2} \left[(A_T\, t + B_T)^{5/2} \right]_{t_{i-1}}^{t_i} - \frac{2B_T}{3A_T^2} \left[(A_T\, t + B_T)^{3/2} \right]_{t_{i-1}}^{t_i}
\end{aligned}
\tag{A.5}$$

For $\int_{t_{i-1}}^{t_i} \sqrt{A_T\, t + B_T}\, dt$ the substitution yields:

$$\int_{t_{i-1}}^{t_i} \sqrt{A_T\, t + B_T}\, dt = \frac{1}{A_T} \int_{t_{i-1}}^{t_i} u^{1/2} du = \frac{2}{3A_T} \left[u^{3/2} \right]_{t_{i-1}}^{t_i} = \frac{2}{3A_T} \left[(A_T\, t + B_T)^{3/2} \right]_{t_{i-1}}^{t_i} \tag{A.6}$$

Then by inserting the solved integrals into equation (A.2), one obtains the final scheme.

$$s_{BM} = \left(\frac{5}{2\pi} \sqrt{\frac{12k_b}{\rho_s^3}} \sum_{i=1}^{N} Q_i + s_0^{5/2} \right)^{2/5} \tag{A.7}$$

$$Q_i = \frac{2}{5}\frac{A_\rho}{A_T^2}\left[(A_T\,t + B_T)^{5/2}\right]_{t_{i-1}}^{t_i} + \left(\frac{2}{3}\frac{B_\rho}{A_T} - \frac{2}{3}\frac{A_\rho B_T}{A_T^2}\right)\left[(A_T\,t + B_T)^{3/2}\right]_{t_{i-1}}^{t_i} \tag{A.8}$$

To test this scheme we can compare it with the appendix of [Birnstiel, T. et al., 2010], where it is assumed that ρ_d and T is constant. To test this we take the limit of equation A.7 where we let ρ_d and T converge towards a constant in time, eg. letting $T_i \to T_{i+1}$. By doing this we get that A_T and A_ρ goes towards 0 and $B_T \to T_c$ and $\rho_d \to \rho_{d,c}$. Here the c subscripts means a constant. By using this we can see that there is a problem with $A_T \to 0$ as we will get $0/0$. Here we use L'Hôpital's rule to see how the expression convergence. We start with the term of $(A_T t + B_T)^{5/2}$.

$$\lim_{A_T \to 0} \frac{(A_T t_i + T_c)^{5/2} - (A_T t_{i-1} + T_c)^{5/2}}{A_T^2} = \frac{15}{8}T_c^{1/2}(t_i^2 - t_{i-1}^2) \tag{A.9}$$

Here we see that it convergence towards a finite non-zero term. The same goes for the $3/2$ over A_T^{-2} term.

$$\lim_{A_T \to 0} \frac{(A_T t_i + T_c)^{3/2} - (A_T t_{i-1} + T_c)^{3/2}}{A_T^2} = \frac{3}{8}T_c^{1/2}(t_i^2 - t_{i-1}^2) \tag{A.10}$$

Lastly we have the $3/2$ term over A_T.

$$\lim_{A_T \to 0} \frac{(A_T t_i + T_c)^{3/2} - (A_T t_{i-1} + T_c)^{3/2}}{A_T} = \frac{3}{2}T_c^{1/2}(t_i - t_{i-1}) \tag{A.11}$$

With this we can see that all the temperature terms converges towards something finite when we converge towards a constant temperature. For the dust density we never divide with A_ρ so all terms with this becomes zero. So equation (A.7) becomes

$$s_{BM} = \left(\frac{5}{2}\frac{\rho_{d,c}}{\rho_s\,\pi}\sqrt{\frac{12k_b T_c}{\rho_s}}\sum_{i=1}^{N}\{t_i - t_{i-1}\} + s_0^{5/2}\right)^{2/5} \tag{A.12}$$

The sum here will cancel all mid terms out, thus we gain the difference between the last point and the first point.

$$s_{BM} = \left(\frac{5}{2}\frac{\rho_{d,c}}{\rho_s\,\pi}\sqrt{\frac{12k_b T_c}{\rho_s}}\{t_N - t_0\} + s_0^{5/2}\right)^{2/5} \tag{A.13}$$

This is exactly what would have been obtained if solving equation (3.38), for a constant dust density and system temperature.

Relative Velocities in the radial and azimuthal direction

Radial and Azimuths relative velocities is given by equation (3.40). This form is not that applicable the Galerkin approximation, there it is black boxed and thus assumed that the relative velocity difference is the physical variable where nothing is known. This gives the following decomposition.

$$C = 1 \wedge \xi = 1 \wedge Y = \Delta v_j \tag{A.14}$$

For this section j refer to either the radial velocity or the azimuthal velocity. With these equation (3.51) becomes the following

$$s - s_0 = \frac{1}{\rho_s}\sum_{i=1}^{N}\left(A_\rho\int_{t_{i-1}}^{t_i} t\,(A_j\,t + B_j)\,dt + B_\rho\int_{t_{i-1}}^{t_i} A_j\,t + B_j\,dt\right) \tag{A.15}$$

The integrals on the RHS are trivial to solve as they are just various orders of polynomials. The first integral becomes.

$$\int_{t_{i-1}}^{t_i} t\,(A_j\,t + B_j)\,dt = \frac{A_j}{3}\left[t^3\right]_{t_{i-1}}^{t_i} + \frac{B_j}{2}\left[t^2\right]_{t_{i-1}}^{t_i} \tag{A.16}$$

The second integral becomes.

$$\int_{t_{i-1}}^{t_i} A_j\,t + B_j\,dt = \frac{A_j}{2}\left[t^2\right]_{t_{i-1}}^{t_i} + B_j\left[t\right]_{t_{i-1}}^{t_i} \tag{A.17}$$

Then by inserting these integrals into equation (A.15) and solving for s one obtains.

$$s_j(t) = \sum_{i=1}^{N}\left\{\frac{A_\rho A_j}{3\rho_s}\left[t^3\right]_{t_{i-1}}^{t_i} + \frac{B_j A_\rho + B_\rho A_j}{2\rho_s}\left[t^2\right]_{t_{i-1}}^{t_i} + \frac{B_j B_\rho}{\rho_s}\left[t\right]_{t_{i-1}}^{t_i}\right\} + s_0 \tag{A.18}$$

To check that the scheme is calculated correctly we once again let the physical variables go towards constant. In the case of the relative velocities, there is no diving by a A_ψ factor therefore the convergence is straight forward, as terms with the A_ψ goes towards zero.

$$\lim_{A_j,A_\rho \to 0}\left\{\frac{A_\rho A_j}{3\rho_s}\left[t^3\right]_{t_{i-1}}^{t_i} + \frac{B_j A_\rho + B_\rho A_j}{2\rho_s}\left[t^2\right]_{t_{i-1}}^{t_i} + \frac{B_j B_\rho}{\rho_s}\left[t\right]_{t_{i-1}}^{t_i}\right\} = \frac{\rho_d}{\rho_s}\Delta v_j(t_i - t_{i-1}) \tag{A.19}$$

Thus one obtain a scheme for a constant dust density and relative velocity.

$$s_j(t) = \frac{\rho_d}{\rho_s}\Delta v_j\{t - t_0\} + a_0 \tag{A.20}$$

This is exactly the what would have been obtained if solving equation (3.38), for a constant relative velocity.

Turbulent Motion

The relative velocity due to turbulent motion can described by equation (3.41). Here we take the stokes number to be of the Epstein regime, equation (3.10) only as it is what is used in the thesis and is quite easier to handle, than most of the stokes regimes. For the Epstein regime the decomposition's becomes.

$$C = \begin{cases} \sqrt{2\alpha\rho_s}\left(\dfrac{32Gk_b}{24\mu m_p}\right)^{1/4} & \text{for } St \le 1 \\[2ex] \sqrt{\dfrac{2\alpha}{\rho_s}}\left(\dfrac{24k_b^3}{32G\mu^3 m_p^3}\right)^{1/4} & \text{for } St > 1 \end{cases} \tag{A.21}$$

$$\xi = \begin{cases} s^{1/2} \text{ for } & St \le 1 \\[1ex] s^{-1/2} \text{ for } & St > 1 \end{cases} \tag{A.22}$$

$$Y = \begin{cases} \rho_g^{-1/4}T^{1/4} & \text{for } St \le 1 \\[1ex] \rho_g^{1/4}T^{3/4} & \text{for } St > 1 \end{cases} \tag{A.23}$$

These decomposition is makes the integrals from equation (3.51) incredibly hard to solve analytically. To avoid series expansion or numerical integration, we are gonna cheat a little and assume that we know that how the stokes number depends on grain size s, and then we will collect all the time-dependent parameters into a single new parameter that is linearly interpolated. This will naturally be more inaccurate, but as the purpose of this estimation is to

see if coagulation is efficient, and give an idea of the grain growth, such an approximation is acceptable. With this new perspective your time dependent parts become.

$$Y = \sqrt{Se} = \begin{cases} \sqrt{\rho_g^{-1/2} T^{1/2}} & \text{for } St \leq 1 \\[2mm] \sqrt{\rho_g^{1/2} T^{3/2}} & \text{for } St > 1 \end{cases} \tag{A.24}$$

Here Se is the new parameter that will be linearly interpolated, and thus the scheme for $St \leq 1$ and $St > 1$ will have the same integral form from the interpolation in equation (3.51). This will give the same integrals as for Brownian motion seen in equation (A.6) and equation (A.5). Therefore the scheme for turbulence can be constructed for both ranges, as their LHS integral is trivial.

$$s_{turb} = \begin{cases} \left[\sqrt{\dfrac{\alpha}{2\rho_s}} \left(\dfrac{32 G k_b}{24 \mu m_p} \right)^{1/4} \sum\limits_{i=1}^{N} Q_i + s_0^{1/2} \right]^2 & \text{for } St \leq 1 \\[6mm] \left[\dfrac{3}{2} \sqrt{\dfrac{2\alpha}{\rho_s^3}} \left(\dfrac{24 k_b^3}{32 G \mu^3 m_p^3} \right)^{1/4} \sum\limits_{i=1}^{N} Q_i + s_0^{3/2} \right]^{2/3} & \text{for } St > 1 \end{cases} \tag{A.25}$$

$$Q_i = \frac{2}{5} \frac{A_\rho}{A_{Se}^2} \left[(A_{Se} t + B_{Se})^{5/2} \right]_{t_{i-1}}^{t_i} + \left(\frac{2}{3} \frac{B_\rho}{A_{Se}} - \frac{2}{3} \frac{A_\rho B_{Se}}{A_{Se}^2} \right) \left[(A_{Se} t + B_{Se})^{3/2} \right]_{t_{i-1}}^{t_i} \tag{A.26}$$

As this scheme is the same in form as the Brownian motion when looking at the interpolation constants, then it will converge in the same manor. Thus the scheme for a constant ρ_g, T and ρ_d becomes.

$$s_{turb} = \begin{cases} \left[\sqrt{\dfrac{\alpha}{2\rho_s}} \left(\dfrac{32 G k_b}{24 \mu m_p} \right)^{1/4} \rho_d Se^{1/2} \{ t_N - t_0 \} + s_0^{1/2} \right]^2 & \text{for } St \leq 1 \\[6mm] \left[\dfrac{3}{2} \sqrt{\dfrac{2\alpha}{\rho_s^3}} \left(\dfrac{24 k_b^3}{32 G \mu^3 m_p^3} \right)^{1/4} \rho_d Se^{1/2} \{ t_N - t_0 \} + s_0^{3/2} \right]^{2/3} & \text{for } St > 1 \end{cases} \tag{A.27}$$

Here we get a linear function inside the outer parenthesis which corresponds to constant physical parameters. The results are in accordance with [Birnstiel, T. et al., 2010], but can be applied to radially dependent data.

Evolution and state for other initial conditions

Some runs are not available at certain configuration as time didn't permit their execution, so if they are missing its likely due to this.

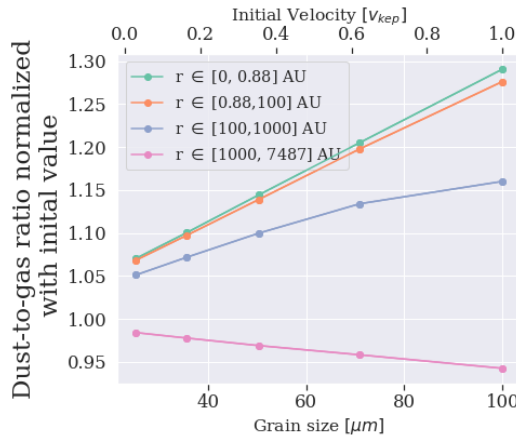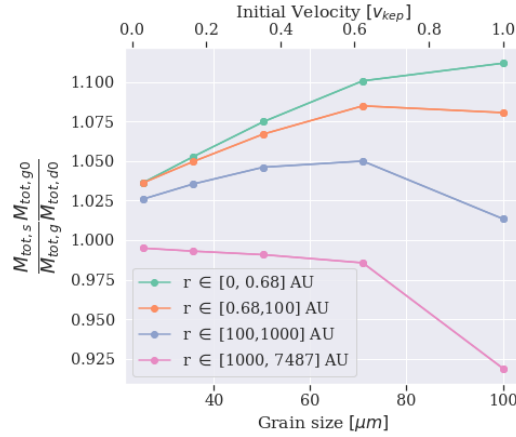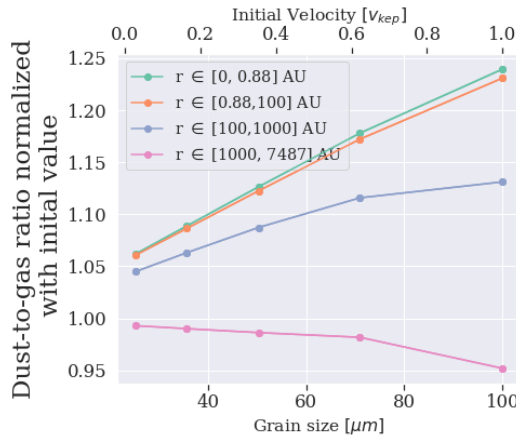## Run006 with a velocity distribution
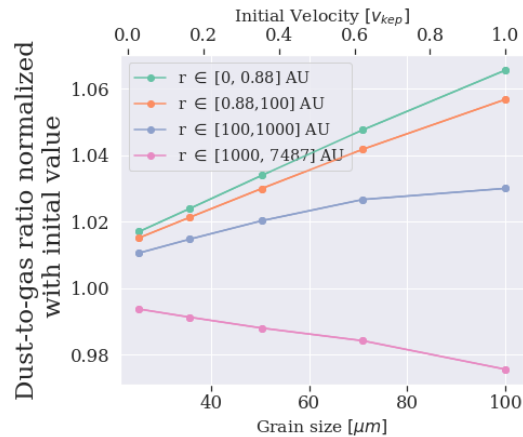
Figure B.1: The-dust-to-gas ratio various regions in the prestellar core as a function of time till the formation of the second Larson core. The first being for the region that will become the reservoir for the protostar which goes from the 0 to r_{evap}. The second region going from r_{evap} to 100 AU is the region where the protoplaneary disk is formed, and is this important for planet formation. The third region is what will accrete unto the embedded Class 0 star. This region goes from 100 AU to 1000 AU. The last region is that of the our edge of the core which will accrete unto the star doing the its transition to the main sequence.

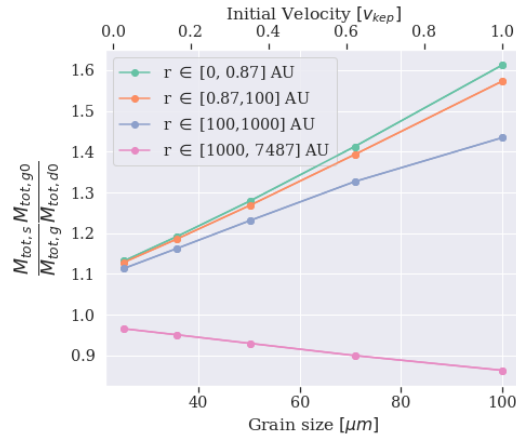## Run009 with a velocity distribution
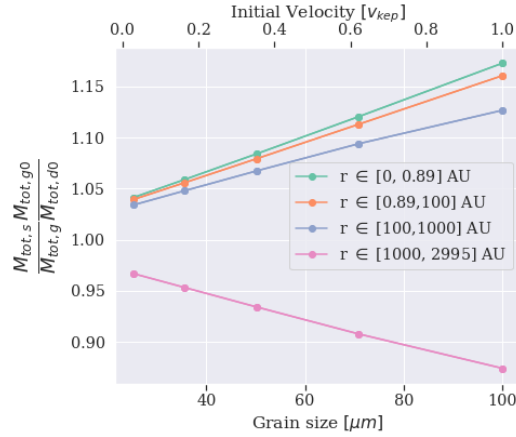
Figure B.2: The-dust-to-gas ratio various regions in the prestellar core as a function of time till the formation of the second Larson core. The first being for the region that will become the reservoir for the protostar which goes from the 0 to r_{evap}. The second region going from r_{evap} to 100 AU is the region where the protoplaneary disk is formed, and is this important for planet formation. The third region is what will accrete unto the embedded Class 0 star. This region goes from 100 AU to 1000 AU. The last region is that of the our edge of the core which will accrete unto the star doing the its transition to the main sequence.
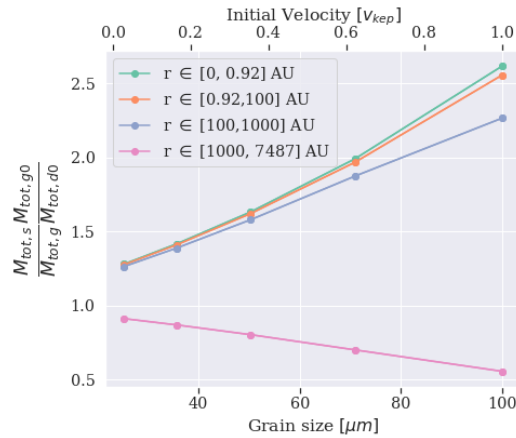
Run038 with a velocity distribution

Figure B.3: The-dust-to-gas ratio various regions in the prestellar core as a function of time till the formation of the second Larson core. The first being for the region that will become the reservoir for the protostar which goes from the 0 to r_{evap}. The second region going from r_{evap} to 100 AU is the region where the protoplaneary disk is formed, and is this important for planet formation. The third region is what will accrete unto the embedded Class 0 star. This region goes from 100 AU to 1000 AU. The last region is that of the our edge of the core which will accrete unto the star doing the its transition to the main sequence.
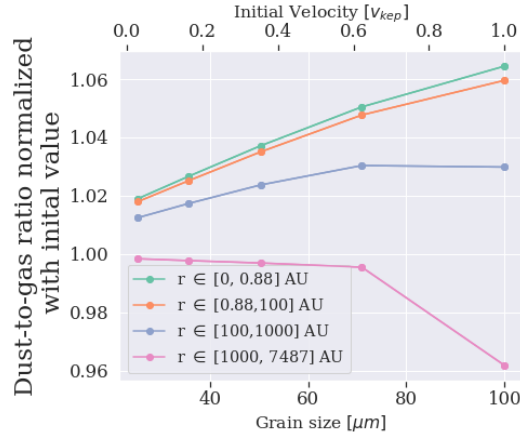
Run068 with a velocity distribution

Figure B.4: The-dust-to-gas ratio various regions in the prestellar core as a function of time till the formation of the second Larson core. The first being for the region that will become the reservoir for the protostar which goes from the 0 to r_{evap}. The second region going from r_{evap} to 100 AU is the region where the protoplaneary disk is formed, and is this important for planet formation. The third region is what will accrete unto the embedded Class 0 star. This region goes from 100 AU to 1000 AU. The last region is that of the our edge of the core which will accrete unto the star doing the its transition to the main sequence.
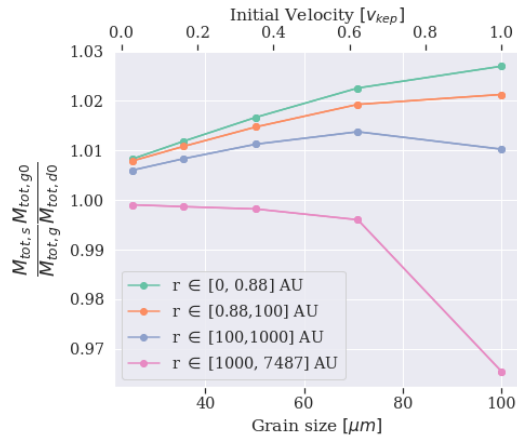
Run069 with a velocity distribution

Figure B.5: The-dust-to-gas ratio various regions in the prestellar core as a function of time till the formation of the second Larson core. The first being for the region that will become the reservoir for the protostar which goes from the 0 to r_{evap}. The second region going from r_{evap} to 100 AU is the region where the protoplaneary disk is formed, and is this important for planet formation. The third region is what will accrete unto the embedded Class 0 star. This region goes from 100 AU to 1000 AU. The last region is that of the our edge of the core which will accrete unto the star doing the its transition to the main sequence.

Run071 with a velocity distribution

Figure B.6: The-dust-to-gas ratio various regions in the prestellar core as a function of time till the formation of the second Larson core. The first being for the region that will become the reservoir for the protostar which goes from the 0 to r_{evap}. The second region going from r_{evap} to 100 AU is the region where the protoplaneary disk is formed, and is this important for planet formation. The third region is what will accrete unto the embedded Class 0 star. This region goes from 100 AU to 1000 AU. The last region is that of the our edge of the core which will accrete unto the star doing the its transition to the main sequence.

Run072 with a velocity distribution


Figure B.7: The-dust-to-gas ratio various regions in the prestellar core as a function of time till the formation of the second Larson core. The first being for the region that will become the reservoir for the protostar which goes from the 0 to r_{evap}. The second region going from r_{evap} to 100 AU is the region where the protoplaneary disk is formed, and is this important for planet formation. The third region is what will accrete unto the embedded Class 0 star. This region goes from 100 AU to 1000 AU. The last region is that of the our edge of the core which will accrete unto the star doing the its transition to the main sequence.

Run074 with a velocity distribution

Figure B.8: The-dust-to-gas ratio various regions in the prestellar core as a function of time till the formation of the second Larson core. The first being for the region that will become the reservoir for the protostar which goes from the 0 to r_{evap}. The second region going from r_{evap} to 100 AU is the region where the protoplaneary disk is formed, and is this important for planet formation. The third region is what will accrete unto the embedded Class 0 star. This region goes from 100 AU to 1000 AU. The last region is that of the our edge of the core which will accrete unto the star doing the its transition to the main sequence.

Run080 with a velocity distribution

Figure B.9: The-dust-to-gas ratio various regions in the prestellar core as a function of time till the formation of the second Larson core. The first being for the region that will become the reservoir for the protostar which goes from the 0 to r_{evap}. The second region going from r_{evap} to 100 AU is the region where the protoplaneary disk is formed, and is this important for planet formation. The third region is what will accrete unto the embedded Class 0 star. This region goes from 100 AU to 1000 AU. The last region is that of the our edge of the core which will accrete unto the star doing the its transition to the main sequence.
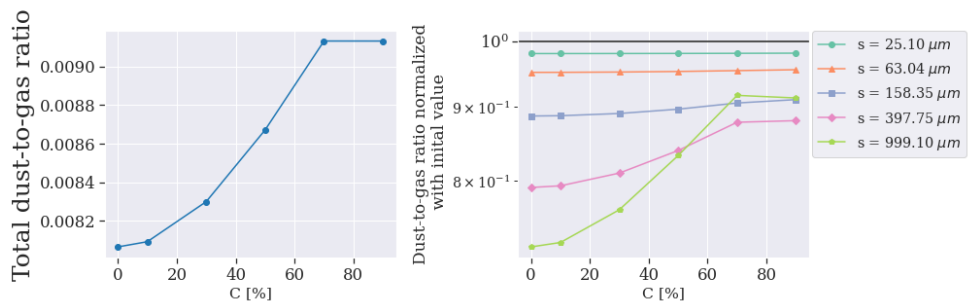
Configuration 1 run006
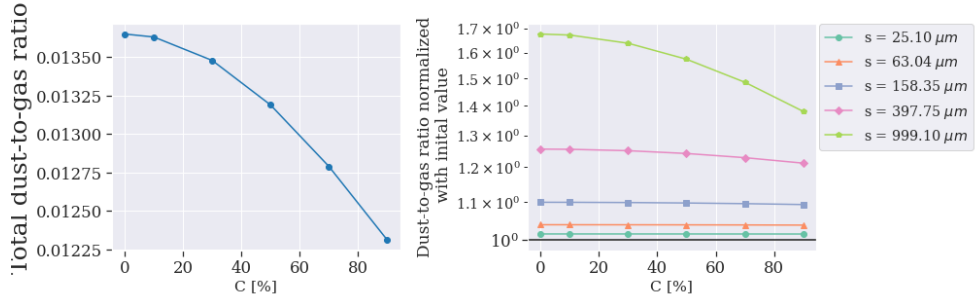
(a) The region below the evaporation line of 0.70 AU for the last snapshot
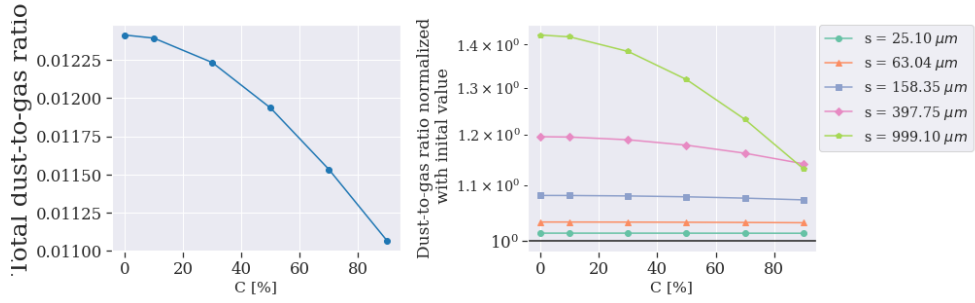
(b) The region between the evaporation line of 0.70 AU to 100*AU* for the last snapshot
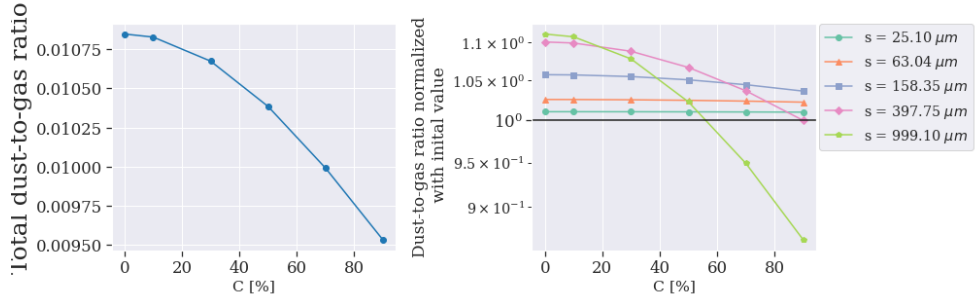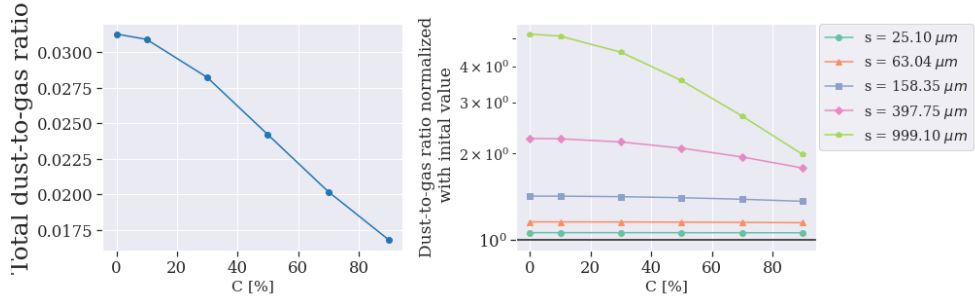

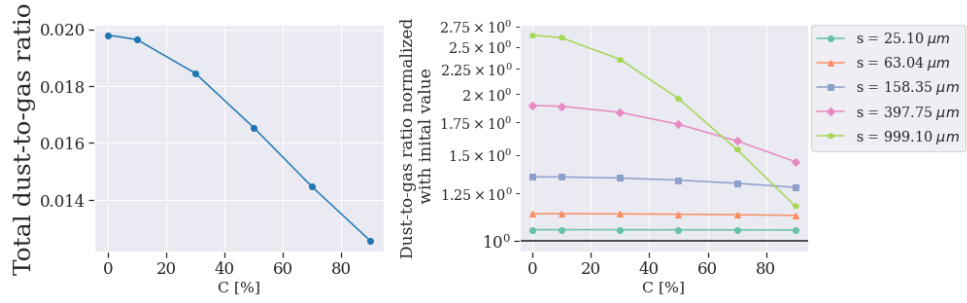(c) The region between 100 AU and 1000 AU for the last snapshot
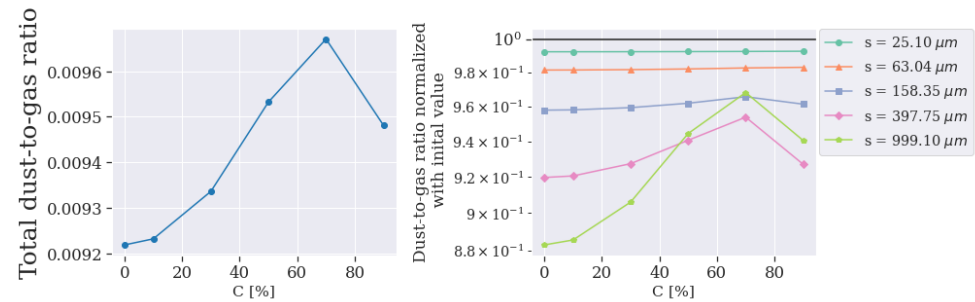
(d) The region over 1000 *AU* to end of sphere for the last snapshot

Figure B.10: The panels here are identical to figure 4.8, but here its for run006 and goes over the same regions. To summarize, the x-axis for all panels is initial keplarian velocity percentage. The y axis on the right plot is the total dust-to-gas ratio, while the right plot is the grain specific dust-to-gas ratio. Each panel is a represent a different region at the last snapshot. **(a)** is from the center and up evaporation line, **(b)** is from the evaporation line to 100 AU, **(c)** is from 100 to 1000 AU, and **(d)** goes from 1000 AU to the end of the core.
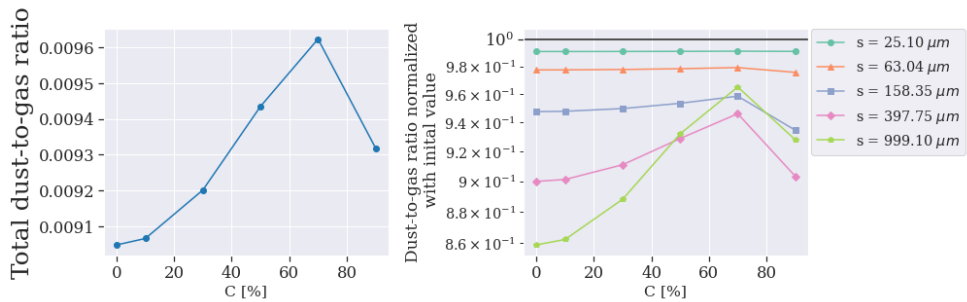
Configuration 1 run038
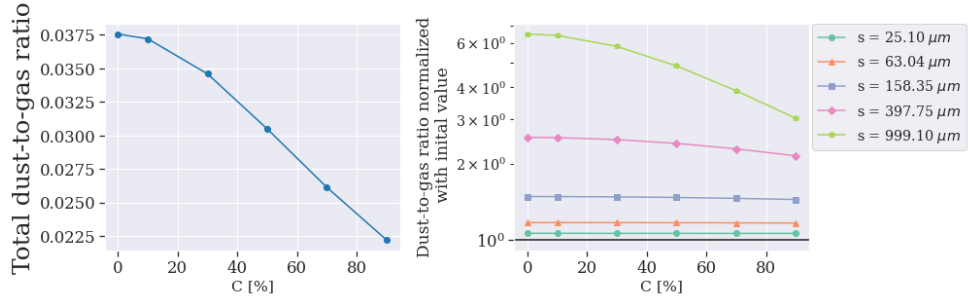
(a) The region below the evaporation line of 0.66 AU for the last snapshot
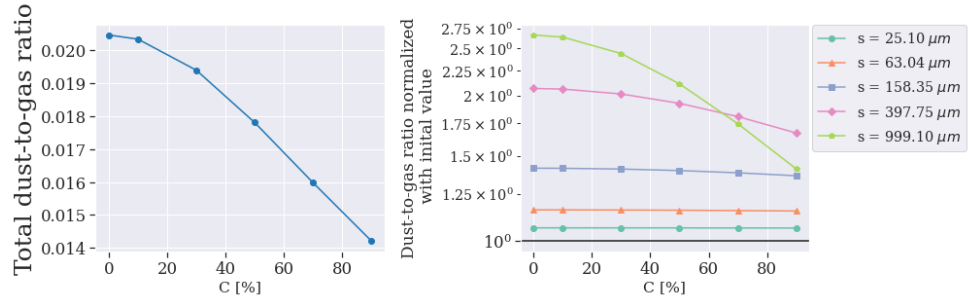
(b) The region between the evaporation line of 0.66 AU to 100*AU* for the last snapshot
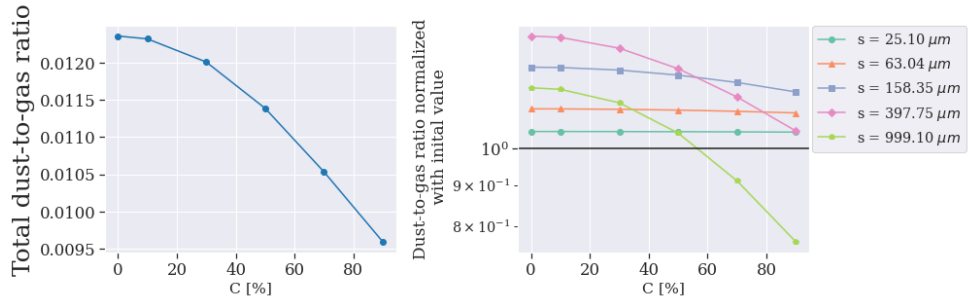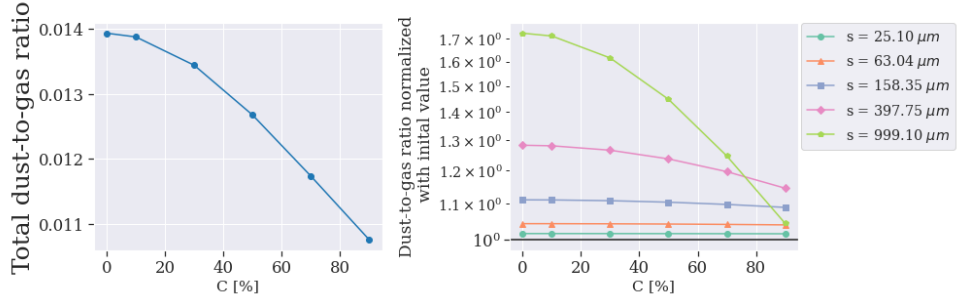

(c) The region between 100 AU and 1000 AU for the last snapshot
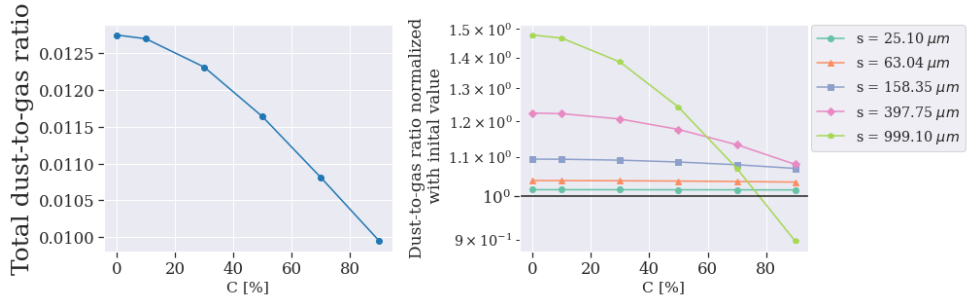

(d) The region over 1000 *AU* to end of sphere for the last snapshot

Figure B.11: The panels here are identical to figure 4.8, but here its for run038 and goes over the same regions. To summarize, the x-axis for all panels is initial keplarian velocity percentage. The y axis on the right plot is the total dust-to-gas ratio, while the right plot is the grain specific dust-to-gas ratio. Each panel is a represent a different region at the last snapshot. **(a)** is from the center and up evaporation line, **(b)** is from the evaporation line to 100 AU, **(c)** is from 100 to 1000 AU, and **(d)** goes from 1000 AU to the end of the core.

Configuration 1 run069

(a) The region below the evaporation line of 0.70 AU for the last snapshot

(b) The region between the evaporation line of 0.70 AU to 100*AU* for the last snapshot
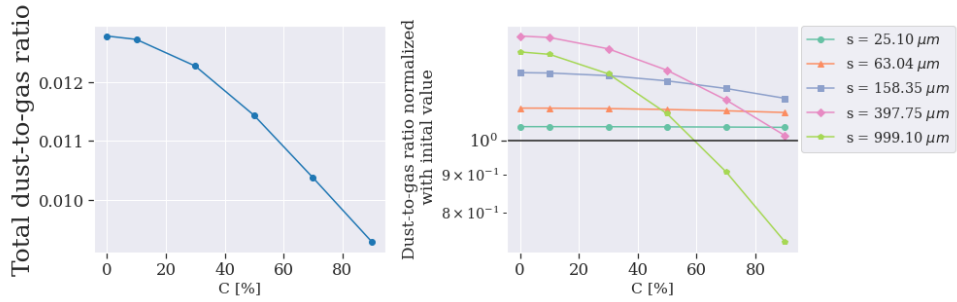
(c) The region between 100 AU and 1000 AU for the last snapshot

(d) The region over 1000 *AU* to end of sphere for the last snapshot

Figure B.12: The panels here are identical to figure 4.8, but here its for run069 and goes over the same regions. To summarize, the x-axis for all panels is initial keplarian velocity percentage. The y axis on the right plot is the total dust-to-gas ratio, while the right plot is the grain specific dust-to-gas ratio. Each panel is a represent a different region at the last snapshot. **(a)** is from the center and up evaporation line, **(b)** is from the evaporation line to 100 AU, **(c)** is from 100 to 1000 AU, and **(d)** goes from 1000 AU to the end of the core.

Configuration 1 run074

(a) The region below the evaporation line of 0.80 AU for the last snapshot

(b) The region between the evaporation line of 0.80 AU to 100*AU* for the last snapshot
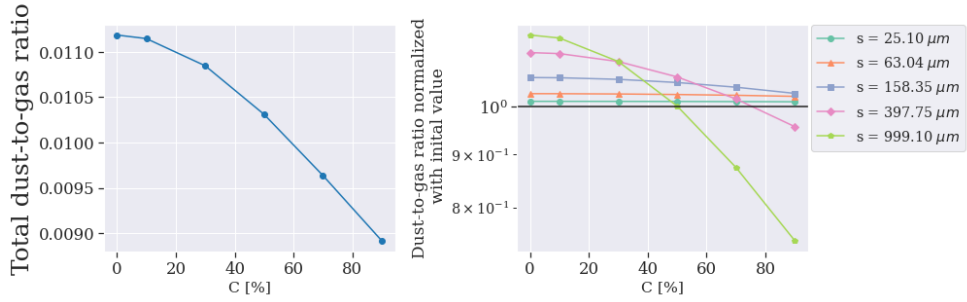
(c) The region between 100 AU and 1000 AU for the last snapshot
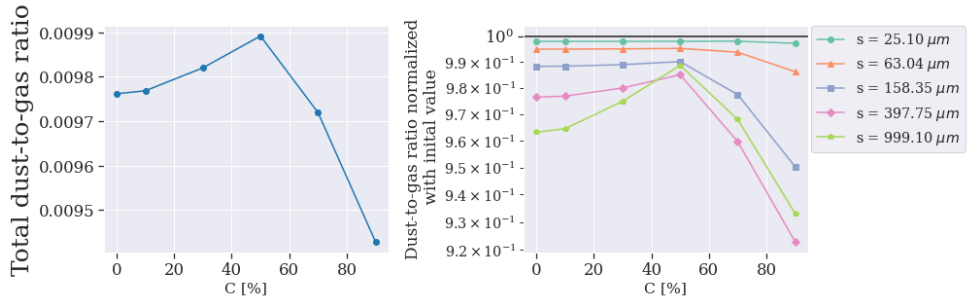
(d) The region over 1000 *AU* to end of sphere for the last snapshot

Figure B.13: The panels here are identical to figure 4.8, but here its for run074 and goes over the same regions. To summarize, the x-axis for all panels is initial keplarian velocity percentage. The y axis on the right plot is the total dust-to-gas ratio, while the right plot is the grain specific dust-to-gas ratio. Each panel is a represent a different region at the last snapshot. (a) is from the center and up evaporation line, (b) is from the evaporation line to 100 AU, (c) is from 100 to 1000 AU, and (d) goes from 1000 AU to the end of the core.

Coagulation for run067 large grains

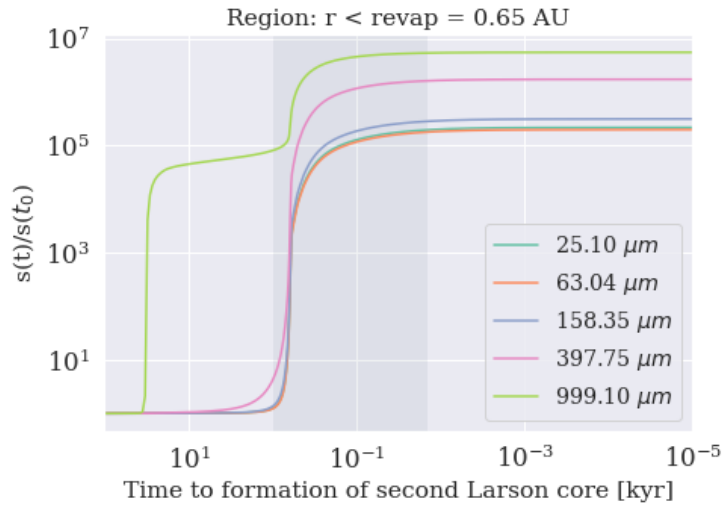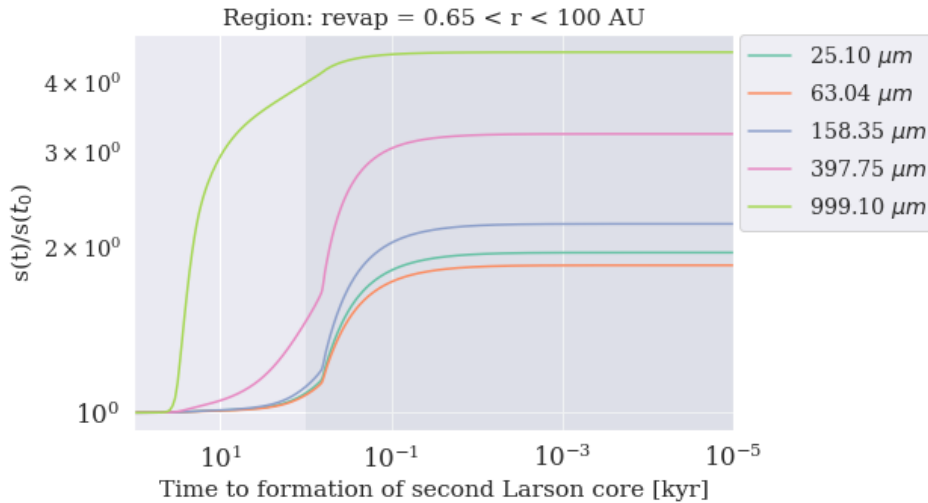### For the region under r_{evap} for the last snapshot

Figure B.14: The growth due to radial coagulation over time to second Larson core formation. The start of the shaded area shows when the first adiabatic phase of the core begins, and when the shaded area ends shows when the temperature exceeds the dust evaporation temperature of $1550K$. This is for the region under the evaporation line, which is what will accrete unto the very early star

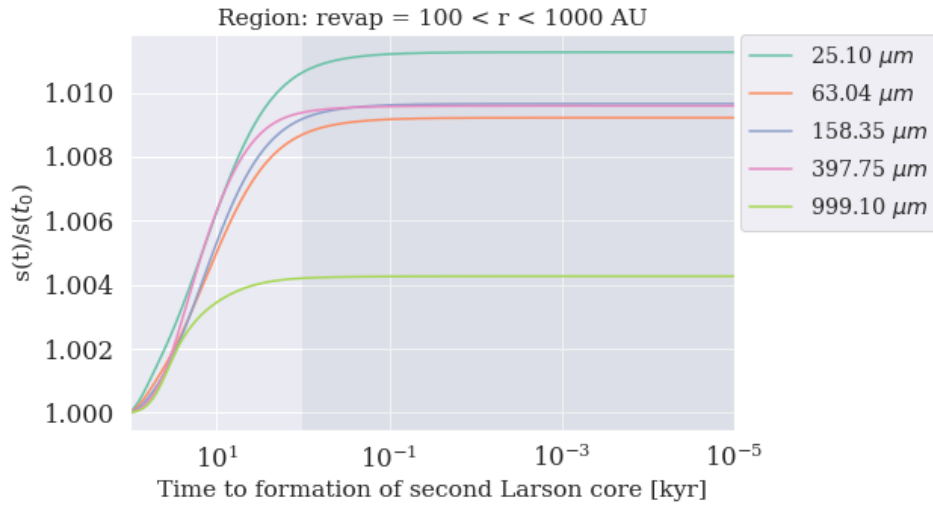### For the region between r_{evap} and 100 AU for the last snapshot

Figure B.15: The growth due to radial coagulation over time to second Larson core formation. The start of the shaded area shows when the first adiabatic phase of the core begins. This is for the region between the evaporation line and 100 AU, which is where the protoplanetary disk is formed.

For the region between 100 AU and 1000 AU for the last snapshot

Figure B.16: The growth due to radial coagulation over time to second Larson core formation. The start of the shaded area shows when the first adiabatic phase of the core begins. This is for the region between the 100 and 1000 AU, which is what will eventually accrete unto the embedded Class 0 object.

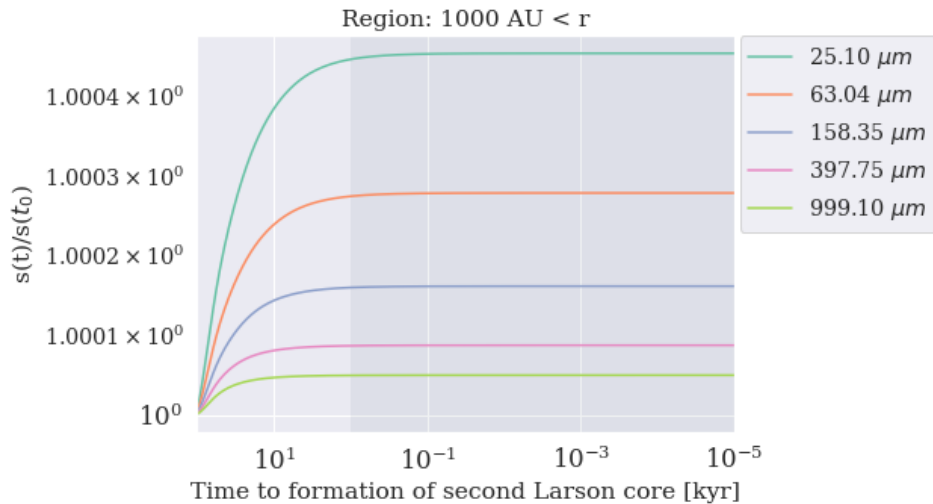**For the region between 1000 AU and the edge of the core for the last snapshot**

Figure B.17: The growth due to radial coagulation over time to second Larson core formation. The start of the shaded area shows when the first adiabatic phase of the core begins. This is for the region between 1000 AU to the end of the prestellar core. This is was will accrete unto the star when it begins to transition to the main sequence